2018

Micro-scale Fracture Toughness Testing and Finite Element Analysis of Transparent Ceramics

Fiona Yuwei Cui
Lehigh University

Micro-scale Fracture Toughness Testing and Finite Element Analysis of Transparent Ceramics

by

Fiona Yuwei Cui

Presented to the Graduate and Research Committee

of Lehigh University

in Candidacy for the Degree of

Doctor of Philosophy

in

Mechanical Engineering

Lehigh University

May 2018

Certificate of approval

Approved and recommended for acceptance as a dissertation in partial fulfillment of the requirements of the degree of Doctor of Philosophy

_____

Date

_____

Richard P. Vinci, Ph.D.
Dissertation Director

_____

Accepted Date

Committee Members:

_____

Richard P. Vinci, Ph.D.
Committee Chair

_____

Martin P. Harmer, Ph.D.
Committee Member

_____

Herman Nied, Ph.D.
Committee Member

_____

Edmund B. Webb III, Ph.D.
Committee Member

_____

D. Gary Harlow, Ph.D.
Committee Member

_____

Murat Saribay, Ph.D.
Committee Member

Acknowledgements

I would like to take this special opportunity to give thanks to everyone who has helped me and supported me in so many special ways throughout my years at Lehigh University.

First and foremost, my appreciation goes to my advisor, Dr. Richard Vinci. He is not only an excellent scientist, but also a great mentor, a real friend and a role model. Dr. Vinci has taught me how to be a scientist, who thinks innovatively and has attitude of rigorous scholarship. By his immense and extensive knowledge, insights, encouragement and support, I was led into real appreciations of science and the work I do. He has shown me what a real mentor and role model is like, who truly cares for his students and has their best interests at heart always. I'm deeply infected and inspired by his scientific attitude and his cheerful and genial personality. I would like to give thanks to my committee members, Dr. Martin Harmer, Dr. Herman Nied, Dr. Edmund Webb III, Dr. D. Gary Harlow and Dr. Murat Saribay for their academic advice, generous help, constructive discussions and tremendous support.

I would also like to give thanks to my collaborators, Dr. Animesh Kundu, Dr. Onthida Schumacher and Dr. Amanda Krause. Without the efforts and dedication of everyone, this work could not have been completed. I would like to extend my gratitude

to the National Science Foundation (CMMI-1436585) for providing the financial support for my research and study.

My gratitude also goes out to all the faculty and staff members in the Department of Materials Science and Engineering and the Department of Mechanical Engineering and Mechanics. I'm very grateful for Dr. Robert Keyse for his training and assistance on FIB and ARM and Mr. William Mushock for his kind assistance on all the SEMs. I would also like to give thanks to department coordinators and staff, Ms. Sue Stelter, Ms. JoAnn Casciano, Ms. Katrina Kraft, Ms. Lisa Arechiga, Ms. Janie Carlin and Ms. Allison Marsteller for all their support and assistance in so many ways.

Moreover, I would like to thank all my friends for sharing this life journey with me and making it memorable and pleasant. I would like to thank my officemates Mr. Jeff Smyth and Dr. Denise Yin for all the lunch dates and interesting discussions. I would like to thank my friends, Ms. Xiuyuan Li, Ms. Chenxi Liu, Ms. Patty Cone, Ms. Elizabeth Ajamu, Mr. Pat Tannous, Dr. Ese Duke, I couldn't imagine my Ph.D. life at Lehigh without the company of you guys.

Finally, I would like to thank my family, who have always been there for me. My mother, Ms. Yanxia Wang, without your support and love, I won't be able to be who I am today. My father, Mr. Fang Cui, my grandmother, Ms. Shuyun Wang and my cousin, Ms. Shasha Cui. It is your unconditional love that gives me motivation to strive for the best. And most importantly, I would like to acknowledge my Heavenly Father for granting me wisdom, strength and a life with faith, hope and love.

Table of contents

Acknowledgements.....iv

Table of contents vi

List of tables xi

List of figures.....xii

Abstract..... 1

Chapter 1. Introduction 4

1.1 Fracture toughness overview..... 4

1.1.1 Three characteristics of fracture behavior 4

1.1.2 Two methods to quantify fracture toughness..... 7

1.1.3 Intrinsic and extrinsic toughness 13

1.1.4 Fracture toughness of brittle materials..... 15

1.2 Magnesium aluminate spinel 17

1.2.1 Motivation 17

1.2.2 Problem statement 19

1.2.2.1. Arguments of surface energy. 19

1.2.2.2. Lack of systematic study of dopants effect on spinel fracture behavior 20

1.2.2.3. Discrepancy of bulk materials fracture testing results 22

Chapter 2. Fracture testing of brittle materials 26

2.1 Bulk testing methods 26

2.2 Introduction to small scale mechanical testing 32

2.3 Micro cantilever with straight notch 33

2.4 Micro cantilever with chevron notch 38

2.5 Clamped-clamped rectangular with straight notch 42

Chapter 3. Fracture toughness testing of doped spinel 45

3.1 Tri-crystal specimen fabrication 45

3.2 Improvement of micro cantilever test 47

3.1.1 Sample fabrication 49

3.1.2 In-situ fracture test 50

3.1.3 Finite Element Analysis 51

3.3 Micro cantilever testing of Eu doped spinel 55

3.3.1 Method 55

3.3.2 Fracture Test results 56

3.4 Discussion on surface energy and grain boundary energy 58

3.4.1 Single crystal 58

3.4.2 Undoped interface fracture 59

3.4.3 Eu-Doped interface 61

Chapter 4. Direct correlation of grain boundary structure and fracture behavior 62

4.1 Grain boundary segregation behavior 62

4.2 Previous work on rare earth doped spinel 63

4.3 Eu doped Tri crystal grain boundary fracture behavior 67

4.3.1 Fracture results 67

4.3.2 Fractography 68

4.4 Atomic resolution STEM characterization of grain boundaries 70

4.4.1 Atomic resolution electron microscopy 70

4.4.2 Electron Microscopy Results 70

4.4.3 In-situ foil fracture 72

4.5 Discussion and Future work 74

4.5.1 {111}{100} interface fracture 74

4.5.2 {110}{100} interface fracture 76

4.5.3. Between the two interfaces 77

4.5.4 Extending to Polycrystalline Spinel 78

4.6 Conclusion 79

Chapter 5. Design of a symmetric rectangular beam fracture test technique 82

5.1 Limitation of present test techniques 82

5.2 3pt bend rectangular beam with chevron notch test 84

5.2.1 Design criteria 84

5.2.2 Specimen fabrication 87

5.2.3 Limitation 89

5.3 Clamped-clamped rectangular chevron specimen 91

5.3.1 Specimen fabrication 91

5.3.2 Test results 92

5.3.3 3D Modeling in ANSYS and Frac3D 95

5.3.4 Crack stability analysis of fixed-fixed rectangular chevron specimen 96

5.4 Discussion and limitation 103

Chapter 6. Design of the micro bowtie chevron test technique 105

6.1 Bowtie chevron design 105

6.2 Experimental 107

6.2.1 Specimen fabrication 107

6.2.2 In-situ micro mechanical testing procedure 109

6.2.3 Contact stiffness correction to experimental data 110

6.3 Complex load cycle for minimizing large deflection effect 112

6.3.1 Introduction 112

6.3.2 Experimental procedure 113

6.4 Finite element analysis modeling 117

6.5 Geometry sensitivity evaluation 118

6.5.1 Method 118

6.5.2 Geometry sensitivity results 120

6.6 Crack stability analysis 126

6.6.1 Methodology 126

6.6.2 Crack stability results 130

6.6.3 Stability verification by TEM 131

6.7 Fracture energy calculation 133

6.8 Conclusion 138

Chapter 7. Conclusion and Future Work 139

Bibliography 145

Vita 155

List of tables

Table 2-1. Advantages and disadvantages of fracture specimens 27

Table 2-2. Advantages, disadvantages and applicability of fracture specimens for brittle materials. 31

Table 3-1. Average fracture toughness results tri-crystal spinel 58

Table 5-1 Specimen configuration and requirements for 3pt bending chevron notched beam ASTM C1421-15[39] 86

Table 5-2 Additional requirement for valid 3pt bending chevron notched beam test[39] 86

Table 5-3 Specimen dimension selected in our micro beam fabrication 87

Table 6-1. Geometry sensitivity results. Normalized impact factor of each dimension change. 124

Table 6-2. Fused quartz fracture toughness value comparison with literature 137

Table 6-3. ZerodurTM fracture toughness value comparison with literature 138

List of figures

Figure 1-1. Stress strain curve of brittle and ductile material. Fracture strength/ultimate strength of brittle material is shown in color blue. Fracture strength of ductile material is shown in color red. The area under stress strain curve estimates toughness. 5

Figure 1-2. Three major modes of loading. Mode I: opening mode. Mode II: shear mode. Mode III: Tearing mode, out of plane shear 9

Figure 1-3. Crack tip stress field 10

Figure 1-4. Classes of extrinsic crack-tip shielding mechanisms in solids. 13

Figure 1-5. (a) Damage to the glass window of space shuttle Challenger caused by a paint chip (b) No penetration through transparent $MgAl_2O_4$ Spinel after five rounds of bullets, demonstrates a higher fracture resistance over glass window 17

Figure 1-6 Dopants effect on the properties of polycrystalline spinel (a) without LiF (b) LiF doped spinel, demonstrate a higher transparency of spinel (c) without LiF (d) LiF doped spinel, evidence of a grain boundary fracture 21

Figure 1-7 Influence of rare earth dopants on fracture toughness of Silicon Nitride. (a) As the ionic radius of rare earth element increases, the toughness increases, however in (b) as the ionic radius increases, the toughness decreases. 23

Figure 2-1. Standardized fracture testing methods for metals and ceramics 26

Figure 2-2. Standardized fracture specimen for brittle materials 30

Figure 2-3 Schematic of nanoindenter loading system and a cantilever microbeam [43] 34

Figure 2-4 (a) Schematic of FIB fabricating a sharp prenotch using decreasing ion beam current. (b) leaving thin bridges on both sides of the pre-notch 35

Figure 2-5 The dimension and crack length measurement from a single crystal spinel {100},<100> sample 36

Figure 2-6. Sketch of the chevron-notched samples used to measure fracture toughness (a) Overcut notch. (b) Undercut notch. The grey area is intact and the white area is a gap between the two parts of the beam. 37

Figure 2-7. Chevron notched cantilever beam in alumina fiber. (a) overview of a fiber from which a beam was machined. (b) the same cantilever at higher magnification (c) view of the triangular ligament after testing (d) beam after testing. 38

Figure 2-8. Indentation corrected load displacement responses of (a) fused quartz and (b) alumina chevron notched cantilever beam samples. 40

Figure 2-9. (a) Triangular micro cantilever beam with chevron notch, as prepared on a flat fused quartz surface. (b) Sketch of chevron notch geometry. (c) Fracture surface of a chevron notch ligament. 41

Figure 2-10. A clamped single edge notched micro beam. (a) clamped beam for bending. (c) microbeam modelled in ABAQUS for simulation. (c) P-d curve of fracture test. (d) Fracture test in SEM in sync with (c) 42

Figure 3-1 Schematic diagram of fabrication process, annealing temperatures and characterization 47

Figure 3-2. Schematic depiction of tri-crystal sample orientation and cantilever beam specimen location. (Cantilever beams are enlarged in dimension relative to tri-crystal in the figure for clear view) 47

Figure 3-3. In-situ micro cantilever deflection fracture test before and after. Hysitron PI85 cono-spherical indenter tip was utilized as a deflection tool. Fracture propagation is aligned with the pre notched plane and after the fracture test, and the fracture surface is exposed, which allows the measurement of the pre notch ratio and characterization of the fracture surface. 48

Figure 3-4. 3D model of the cantilver deflection beam built in ANSYS Mechanical APDL, and refined meshing was applied to the notch area. Force was applied at the loading point. Extra support volume was also added due to the deformation of the bulk material support at the beam root. 52

Figure 3-5. XY plane meshing details, generated with ANSYS Mechanical APDL 14.0. Refinement is applied to highlight area near the notch. 53

Figure 3-6. Fracture toughness values with respect to different specimen condition. Standard deviation was shown in each column. Single crystal {100} and {111} has shown a higher fracture toughness. Undoped {111}/{100} interface is much weaker than a single crystal, Eu doped {111}/{100} interface is in the same range with a higher deviation due to different complexion combination contribution. Undoped {110}/{100} interface is a strong interface has fracture toughness comparable to

{100} single crystal, Eu doped {110}/{100} interface has similar fracture toughness with a higher deviation in the results. 57

Figure 4-1 Fracture toughness value of Yb doped spinel {100}/{111} bicrystal grain boundary [19] 63

Figure 4-2 Atomic resolution HAADF images (a) the intrinsic undoped bicrystal grain boundary and (b) the ytterbium doped bicrystal grain boundary demonstrate different grain boundary structures. High resolution HAADF images showing the ytterbium configuration of (c) 1400 °C (d) 1600°C and (e) 1800 °C annealed specimens in a grain boundary. [19]..... 65

Figure 4-3 Grain growth of polycrystalline spinel for undoped, Eu doped heat treatment temperature at 1400 and 1600 °C..... 66

Figure 4-4 SEM images of fracture surfaces exposed after the fracture test, viewed with a 60 degree angle from the top surface. (a) an undoped {111}/{100} grain boundary is presented here as a 'clean' fracture surface for comparison (b) Eu doped {111} /{100} interfaces, large precipitates of similar shape and size were observed at both fracture surfaces. (c),(d) Eu doped {110} /{100} interfaces, in (c) we observed a mostly 'clean' fracture surface representative of this interface and less regularly we observe voids left from smaller precipitates as shown in (d) 68

Figure 4-5 Atomic Resolution HAADF image of {111}/{100} Eu doped grain boundary and corresponding model..... 72

Figure 4-6 HAADF micrographs of the {111}/{100} grain boundary with two Eu-rich precipitates (a) before and (c) after fracture. (b) High magnification HAADF image

of the interface between the Eu-rich precipitate and the {111} plane before fracture. (d) HAADF image of the {111} spinel free surface after fracture. Figures by Dr. Amanda Krause. 73

Figure 5-1. 3pt bend test with chevron notch configuration schematic in ASTM standard test for bulk materials. Details of dimensions at the chevron notch are shown in higher magnification on the bottom. [39] 84

Figure 5-2. 3pt bend beam with chevron notch in micro scale. (a) Specimen fixed on bottom support with platinum. (b) In-situ fracture test with nano-indenter. 88

Figure 5-3 Fabrication procedure of the free end 3pt bending specimen with chevron notch 89

Figure 5-4 Fixed-fixed end 3pt bending chevron notched micro beam under loading 91

Figure 5-5 Clamped-clamped 3pt bending chevron notched beam mechanical test results. (a) Load and depth responses over time. (b) Load- Displacement during fracture test. 92

Figure 5-6 Clamped-clamped 3pt bending chevron notched beam loading and unloading P-d curve 92

Figure 5-7 SEM images of retrieving a fractured beam and chevron notch shaped fracture surface..... 94

Figure 5-8. Three type of load v. time curves observed for chevron notched specimen; Kic value is determined using peak load Pmax of curves showing smooth turnover. 94

Figure 5-9 Quarter symmetry finite element analysis model of fixed-fixed end chevron notched beam using ANSYS APDL..... 95
Figure 5-10 Specimen compliance obtained from FEA model as a function of crack propagation length 96
Figure 5-11. Generalized Notch/Crack configuration [60] 99
Figure 5-12 Schematic showing stability tendency as a function of crack length for various notch/crack configurations and load conditions[60]..... 101
Figure 5-13. Normalized beam specimen as a function of prenotch ratio..... 102
Figure 5-14 Stability factor Sp and Sd vs. α 102
Figure 6-1. (a) Schematic cross-section of the bowtie chevron-notched beam design, showing the chevron notch during crack propagation. The triangle represents the original intact region and the grey area represents the intact region after some degree of crack growth has occurred. (b) Quarter symmetry FEA model. Axial displacement constraints (z-axis) were applied at the intact area ahead of crack front, where different color highlights represent different crack lengths. 106
Figure 6-2. (a) top surface of a bowtie chevron beam. (b) 30 degree view of a bowtie specimen. (c) A in-situ mechanical test with indenter on top of specimen (d) Crack propagation observed under SEM during in-situ test. 107
Figure 6-3. Indenter tip impression on the top surface post fracture test was shown.. 110
Figure 6-4. Correction applied load displacement curve of a bowtie chevron fracture specimen tested on fused quartz. 111

Figure 6-5. In-situ fracture test of a bowtie chevron specimen. Large deflection is observed in the test with large opening distance of the notch area. 113
Figure 6-6. (a) Hysitron PI85 cyclic loading fracture test results. Compliance in each loading cycle with respect to indentation load. Maximum load corresponds to nonlinear deflection range and minimum load cycle corresponds to linear deflection range. (b) Nanomechanics dynamic stiffness measurement fracture test result showing a comparison between maximum and minimum load cycle stiffness measurement before contact stiffness correction. 115
Figure 6-7. A quarter symmetry finite element analysis model built with ANSYS Mechanical APDL and Altair Hyper mesh. A refined meshing was applied at the crack tip. 117
Figure 6-8. Compliance vs. Crack propagation length, generated through FEA, polynomial fit with MATLAB 118
Figure 6-9. Fracture surface exposed post fracture tests (a) (b) show the two opposite sides of a fracture. (c) (d) depicts the dimensions defined for a bowtie chevron specimen. 120
Figure 6-10. Finite element analysis model with change in different dimensions. (a) length (b) thickness (c) width (d) overcut/undercut (e) notch angle 123
Figure 6-11. (a) Finite element analysis result, the compliance change as crack propagation length. (b) Geometry sensitivity test. Impact ratio as a function of each geometry dimension. 124
Figure 6-12. Crack stability factor vs. normalized crack propagation length 130

Figure 6-13. TEM specimen of notch area, where a crack front could be observed clearly. 133

Figure 6-14. Finite element analysis result of compliance change with respect to crack length 135

Figure 6-15. Compliance change in each unloading segment with respect to load for fused quartz and Zerodur™..... 136

Abstract

Relative surface energies of low-index planes and the effect of Europium segregants on grain boundary structure and fracture strength of magnesium aluminate spinel ($MgAl_2O_4$) bicrystals were evaluated by micro scale fractures tests and high-resolution electron microscopy. Single crystal specimens with {111}, {110}, and {100} boundary planes were bonded together using hot pressing to make {111}/{100} and {100}/{110} interfaces. Certain of the resulting specimens were doped with Eu. Micro cantilever deflection tests were employed to measure fracture toughness within each single crystal and at both bicrystal boundaries. Correlating surface energy with fracture energy measurements, the surface energies of {111}, {110}, and {100} planes were found to have a decreasing trend. High-angle annular dark-field-scanning transmission electron microscopy (HAADF-STEM) was utilized to characterize grain boundary structure and chemistry. Differences in Eu segregation behavior on the two grain boundaries resulted in differences in grain boundary structure and differences in corresponding interfacial fracture strength. Eu segregated more uniformly to the {111}/{100} interface where it bonded strongly to the {111} plane but not to the {100} plane. The doped {100}/{110} boundary was characterized by a lack of uniform segregation. Corresponding fractography work and an in-situ foil fracture test was

carried out in addition at the interface, aiding the structure and fracture behavior analysis. Here, we demonstrate how micro-cantilever fracture toughness measurements on single crystal and individual grain boundaries can indicate surface energy trends. And by combining micro fracture tests and HAADF-STEM analysis, a method to investigate the correlation between the grain boundary structure and fracture strength was established to interpret how rare earth segregation behavior affects intrinsic toughening mechanisms of magnesium aluminate spinel.

In recognition of the shortcomings of the microcantilever bend fracture test, a new micro-scale fracture test that uses a bowtie-shaped micro-beam specimen with a chevron notch was designed and employed in transparent ceramic toughness testing. This clamped-clamped specimen can produce stable crack growth in brittle materials. Cyclic loading causes progressive crack extension, thereby producing multiple fracture toughness results in one experiment. The symmetric geometry eliminates the mixed mode fracture that exists in single-ended cantilevers. A 3D finite element analysis (FEA) model built in ANSYS Mechanical APDL and Altair Hypermesh was used to relate the crack length to the beam compliance. Full analysis of the bowtie chevron specimen geometry sensitivity has been carried out with FEA. A detailed crack stability analysis was conducted combining different nano-mechanical testing system, loading conditions, FEA analysis and TEM experimental methods. MATLAB programming was utilized to process large experimental data and to apply a polynomial fit in establishing a compliance and crack extension length relationship. The fracture energy could then be evaluated using an energy approach (‘Work of Fracture’) by combining FEA and

experimental data. The results of tests using fused quartz and a glass-ceramic material match very well with published fracture toughness values. This validates the new micro scale testing method that possesses a combination of advantages not available in any other testing methods.

Chapter 1. Introduction

1.1 Fracture toughness overview

1.1.1 Three characteristics of fracture behavior

Fracture toughness is an important property of a material, describing the resistance to fracture. There are three general characteristics to describe fracture of the sample or component tested. They are energy of fracture, fracture path, and microscopic fracture mechanisms. [1] These three characteristics are all important when describing the fracture behavior.

First, let's look at fracture energy. The fracture energy is the energy required before and during the fracture process. For a smooth tensile bar, the area under the uniaxial tensile stress-strain curve represents energy per unit volume required during crack propagation process and thus could be utilized as an estimate for fracture toughness, as shown in Figure 1-1. Therefore, a high toughness is a combination of high strength and high ductility. One usually finds that to achieve a higher toughness,

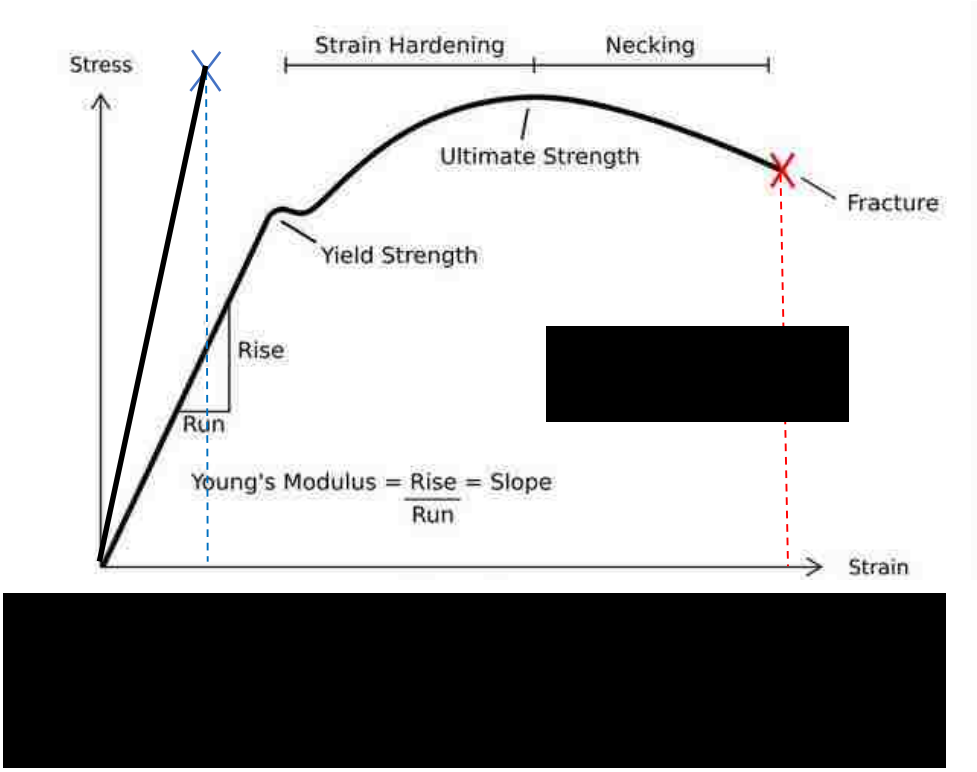

strength is often compromised to induce a higher ductility. For example, in the metallurgy tempering process, which occurs after the hardening process, the purpose is to reduce hardness (proportional to strength) and increase the degree of ductility to achieve high toughness. Ductile materials like metals often have a higher fracture toughness value compared to brittle (non-plastic) materials like ceramics where there is limited ductility. In ceramic materials or brittle metals, toughness is only determined by the strength of the material.

A material is said to be ‘tough’ when higher fracture energy is absorbed during the fracture process. And oppositely, ‘brittle’ means low energy is required during fracture process.

Ceramics are non-plastic and often absorb little energy during fracture, and thus they are brittle in either context. Since a material's fracture property is the focus of this study, when we mention brittle, we are referring to the low energy absorption in fracture energy.

Crack path is the second indicator of the toughness of the material. For example, in brittle metals that fail by cleavage the crack path follows weak planes, and in brittle metals that fail by intergranular processes the crack path follows the grain boundaries. In tough metals, the crack will often be surrounded by evidence of plasticity. In the case of ceramic, a low toughness material will often result in one single crack while a high toughness ceramic will often result in significant crack branching due to massive energy dissipated only to crack growth without plastic deformation available. Since strength correlates to toughness when ductility is absent, high strength ceramics also means higher toughness. Tempered glass will result in a special kind of fracture crack path, due to the nature of the residual stress state present in tempered glass. The tempering process for glass has two types, thermal tempering and chemical tempering. The latter involves an ion exchange process, where larger potassium ions replace the sodium ions in the manufacturing of the famous Gorilla glass. [2] In either type of tempering process, the outer surfaces of the glass are left in compression while the internal part left in tension. Therefore, the strength is much higher in tempered glass than traditional

annealing glass. Fracture will result in a network of cracks propagating and leaving the material in small fragments when the stored energy is released suddenly. Furthermore, a crack path could reveal information of loading condition and crack origin, which is a great indicator in failure analysis work in determining the cause of the failure.

Microscopic mechanisms are the third fracture characteristic, since crack propagation is related to the small process zone around the crack front. For metals, microvoid coalescence is often present due to the crack initiation at a particle between the interface of an inclusion or precipitates and the matrix material. Since ductility is involved in the forming of the microvoids, higher toughness is associated with deeper and wider microvoid coalescence. In addition, trans granular fracture and cleavage fracture are another two fast fracture mechanisms. The latter mechanisms are also present in ceramic fracture.

1.1.2 Two methods to quantify fracture toughness

There are two ways to analyze toughness quantitatively- energy balance analysis and stress field analysis.

First, let's look at the energy balance approach, which was first addressed by Griffith. [3] For brittle materials, this energy balance theory is very applicable in evaluating fracture toughness. Linear elastic fracture mechanics describes quantitatively the fracture behavior of brittle materials. The assumptions include a sharp crack embedded in a continuum elastic body and only a small-scale process zone ahead of the crack tip and thus a linear relation between the stress and strain. In an elastic material, a

balance between the decrease in stored energy and the increase in the surface energy created during the fracture process must be achieved. And therefore, we have

$$U - U_0 = -\frac{\pi \sigma^2 a^2 t}{E} + 4at\gamma_s \tag{1}$$

Where, U is the energy with the crack, U_0 is the energy before the crack and Inglis [4] has derived the decrease in the energy in an infinitely large plate with an elliptical crack as $\frac{\pi \sigma^2 a^2 t}{E}$, where t is the thickness of the plate, a is the half crack length, E is the modulus of the material. And γ_s is the surface energy per unit area. The two free surfaces created after the crack will generate a total free surface area of $4at$.

In the condition of equilibrium, the first derivative of U with respect to crack length a must equal to zero. Thus, we have

$$2\gamma_s = \frac{\pi \sigma^2 a}{E} \tag{2}$$

This equation can be rearranged to be,

$$\sigma = \sqrt{\frac{2E\gamma_s}{\pi a}} \tag{3}$$

for a plane stress condition, and

$$\sigma = \sqrt{\frac{2E\gamma_s}{\pi a(1-\nu^2)}} \tag{4}$$

for a plane strain condition, where ν is Poisson's ratio. Note that this difference is very small since Poisson's ratio is usually in the range between 0.25-0.33. And we could

further include plasticity terms by adding a plastic deformation energy term to the surface energy, so that this equation could be applied to ductile materials.

Irwin [5] then chose to denote the energy source term as elastic strain energy release rate G. Therefore, equation (5) becomes,

$$\sigma = \sqrt{\frac{EG}{\pi a}} \tag{6}$$

Now let's consider a more sophisticated method in evaluating the toughness, the stress field analysis. Westergaard [6] and Irwin [7] first published solutions for crack tip stress distributions with three major modes of loading. These are Mode I (opening or

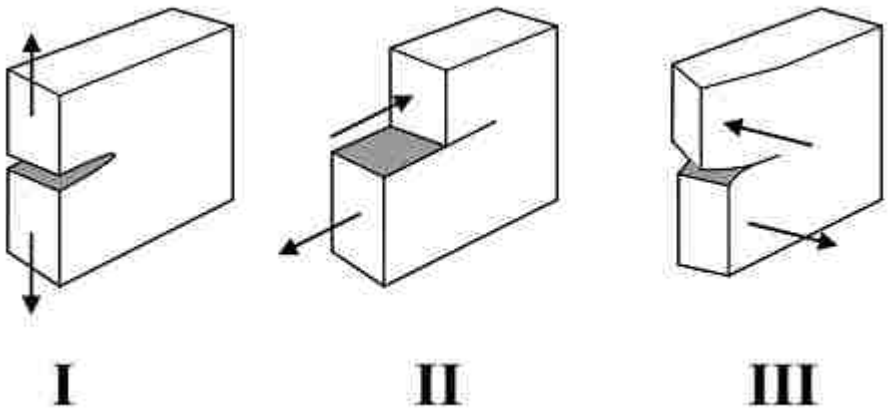

[redacted]

tensile mode), Mode II (Sliding or shear mode) and Mode III (tearing or out of plane shear mode). A schematic diagram of the three stress modes is shown in Figure 1-2.

The crack tip stresses defined as in Figure 1-3 are found to be,

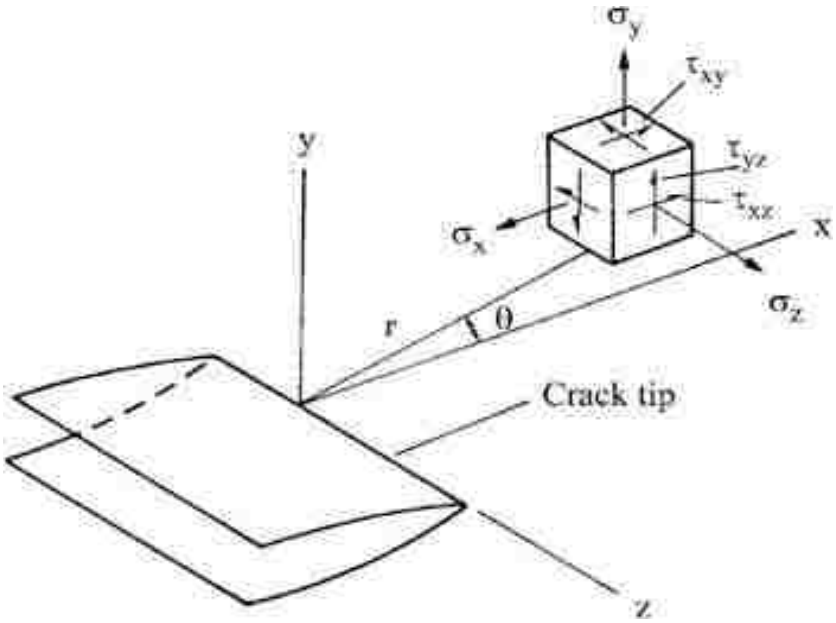

$$\sigma_y = \frac{K}{\sqrt{2\pi r}}\ cos\frac{\theta}{2}\ (1 + sin\frac{\theta}{2}\ sin\frac{3\theta}{2})$$

$$\sigma_x = \frac{K}{\sqrt{2\pi r}}\ cos\frac{\theta}{2}\ (1 - sin\frac{\theta}{2}\ sin\frac{3\theta}{2}) \quad (7)$$

$$\tau_{xy} = \frac{K}{\sqrt{2\pi r}}\ (sin\frac{\theta}{2}\ cos\frac{\theta}{2}\ cos\frac{3\theta}{2})$$

Therefore, we see that the crack tip stress distribution is determined by parameter r and θ and is represented by parameter K, serving as a scale factor of the magnitude. K is then defined as *stress intensity* in the stress field analysis to define the magnitude of the crack tip stress field. K is associated with applied stress and crack length and thus is expressed as,

$$K = Y\sigma\sqrt{\pi a} \quad (8)$$

where, Y is a geometric term. The determination of Y depends on the geometry of the specimen and the crack shape and location. A list of common Y values could be easily found in a handbook.

After these two approaches are understood, a relation between stress, crack size and material properties can be described. A relation between these two approaches can then be derived as,

$$K = \sqrt{EG} \tag{9}$$

for a plane stress condition, and

$$K = \sqrt{\frac{EG}{(1-\upsilon^2)}} \tag{10}$$

for a plane strain condition.

When measuring the fracture toughness experimentally, plane strain condition toughness is usually measured under a mode I (opening mode) loading condition. Instead of plane stress condition, plane strain condition gives the minimum toughness value measured that does not decrease with increasing test specimen thickness, and therefore could be used as the lower limit of the material toughness, denoted as Kic. So Kic is the material toughness characteristic independent of specimen geometry and represent the intrinsic fracture toughness.

In a ductile material, the thickness and crack length needs to meet a certain criterion so that the measured Ki is valid and will not become smaller as the geometry of the specimen becomes thicker and wider. Brown and Srawley [8] have found that,

(11)

$$t \; and \; a \; \geq 2.5 \left(\frac{K_{1c}}{\sigma_{ys}}\right)^2$$

and ratio $\left(\frac{K_{1c}}{\sigma_{ys}}\right)^2$ can be related to plastic zone size in plane strain condition, so we have

$$\left(\frac{K_{1c}}{\sigma_{ys}}\right)^2 = 6 \, \pi \, r_y \tag{12}$$

where r_y is the plastic zone size radius ahead of crack tip. And therefore,

$$t \; and \; a \; \geq 50 \, r_y \tag{13}$$

Kic is often used experimentally to characterize fracture behavior of the material. An ideal experiment thus should give an accurate measurement of mode I loading condition, eliminating other modes. A mixed-mode fracture may occur in certain testing specimen geometry and thus affect the accuracy of the measured toughness. A further comparison of testing specimen geometry studied in this research concerning this matter is discussed in later chapters.

1.1.3 Intrinsic and extrinsic toughness

EXTRINSIC TOUGHENING MECHANISMS

1. CRACK DEFLECTION AND MEANDERING

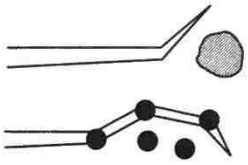

2. ZONE SHIELDING

— transformation toughening

— microcrack toughening

— crack wake plasticity

— crack field void formation

— residual stress fields

— crack tip dislocation shielding

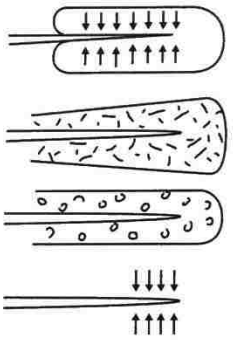

3. CONTACT SHIELDING

— wedging:

corrosion debris-induced crack closure

crack surface roughness-induced closure

— bridging:

ligament or fiber toughening

— sliding:

sliding crack surface interference

— wedging + bridging:

fluid pressure-induced crack closure

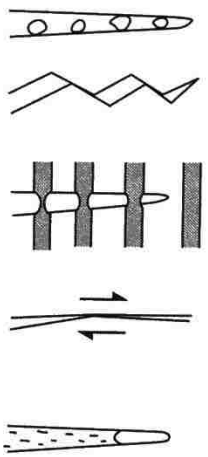

4. COMBINED ZONE AND CONTACT SHIELDING

— placticity-induced crack closure

— phase transformation-induced closure

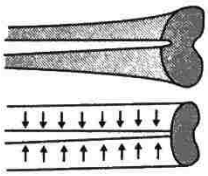

When considering fracture behavior of a material, the energy required in the system for the fracture to propagate is a combination of intrinsic and extrinsic mechanisms. These are influenced by atomic bond strength, interfacial strength, presence of porosity, second phase particles, notches from manufacturing surface processes, microscopic energy dispersive mechanisms during crack propagation including grain bridging and pull-outs that serve as friction agents to prevent crack opening. Therefore, a macroscopic fracture test may result in a measurement combining multiple factors, including the material properties, intrinsically, and other microscopic factors of the system, extrinsically.

Intrinsic toughness of a material is the resistance to damage mechanisms that are active in the region ahead of the crack tip. It will depend on the nature of electron bond, the crystal structure and the degree of order in the material. [1] Atomic bonding provides the differences in toughness in different class of materials. The more rigidly fixed the valence electrons are, the more brittle the material is. Thus, the trend of a decreasing toughness occurs, when the electron bonds varies from metallic to ionic and to covalent. The crystal structure affects toughness significantly as well. High crystal symmetry will induce slip systems to increase ductility and thus higher toughness. A decreasing trend of crystal symmetry from close-packed structure to low-symmetry structure to amorphous will result in a decrease in fracture toughness. For example, FCC structured austenitic steel has a much higher ductility and a much higher toughness compared to BCC structured ferrite. Finally, the degree of order of atomic arrangement increasing will lead to a decreasing in the ability to deform and thus yield a higher

toughness. Random distribution of solid solution (highest order of degree) will suppress the ductility least (highest toughness), then short-order and finally long-order. A reduction in precipitate volume fracture and longer particle spacing will also lead to higher ductility and higher toughness.

Extrinsic toughening mechanisms serve as ways to reduce crack driving force. The first class of extrinsic toughening mechanisms are crack deflection or meandering of the crack paths. Deflection may occur either by interaction with particles or weak planes. As long as the crack tip stress can be reduced by deflection from the perpendicular direction of the applied load, the deflection will occur. Zone shielding is another type of extrinsic mechanism. It involves a plastic deformation or dilatation in a zone surrounding the crack tip and wake. Zone shielding mechanisms include transformation toughening, microcrack toughening, crack wake plasticity, crack field void formation, residual stress fields and crack tip dislocation shielding. Another extrinsic mechanism is crack surface contact shielding. This includes wedging (crack closure), bridging (ligament or fiber toughening), sliding and a combination of wedging and bridging. In addition, a combined zone shielding and contact shielding is caused by plasticity or phase transformation induced crack closure. The schematic of these extrinsic mechanisms is shown in Figure 1-4.[9]

1.1.4 Fracture toughness of brittle materials

For ceramic materials, which are the focus of this study, the intrinsic toughness is very low due to a combination of ionic or covalent bonding, low symmetry crystal structure and long range order. And therefore, toughening processes have been

developed with a focus on extrinsic mechanisms. Rising crack growth resistance, or R-curve behavior, is thus very common in toughened ceramics, such as ceramic matrix composites. As the crack size increases, crack tip shielding mechanisms will increase the toughness of the material, but the strength of the material remains constant, until the crack extension associated with failure dominates. On the other hand, a flat R-curve material will inherit a constant toughness value and a continuously decreasing strength as the crack size increases, raising the stress intensity as it does so. Another mechanism in ceramic materials involves crack path deflection due to a weakened grain boundary or a second phase particle. Moreover, a crack zone shielding mechanism that lowers the crack tip stress intensity may greatly affect the toughness, such as grain bridging, second phase bridging, microcracks and micro voids formation.

Therefore, measurement of fracture toughness of polycrystalline ceramics experimentally is a complicated process involving intrinsic material bonding, crystal structure, grain boundary bonding and extrinsic microscopic mechanisms. In this study, we will introduce fracture toughness testing methods that specifically address this complication. Single crystal fracture testing and micro scale fracture testing methods along single grain boundaries are investigated and employed to simplify the analysis of toughness-influencing factors and establish an experimental methodology in evaluating material properties, such as surface energy, cleavage plane orientation, grain boundary structure and property relationships.

1.2 Magnesium aluminate spinel

1.2.1 Motivation

The ideal windshield material for aircraft, viewports for spacecraft, domes for cameras, and other transparent defense applications is always attracting research attention, since the traditional silicate glass and fused silica glass currently in use exhibit relatively poor mechanical properties when operating in unpredictable environments where they may potentially experience an unexpected impact. The fracture toughness value of such materials is only 0.6-0.8 MPa $m^{1/2}$, which is causing great concern for

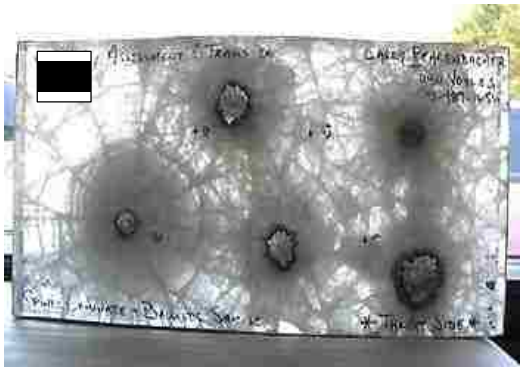

[redacted]

space vehicles, as an increasing number of space debris was reported due to an increasing number of abandoned satellites over the years. "Bullet proof glass" windows are typically made of laminated glass. A common form of laminated glass is a pair of soda lime panels bonded together by a layer of polyvinyl butyral (PVB) polymer. If a crack is initiated, it will arrest at the interface. However, this toughening mechanism will increase the overall weight of the material and reduce the transparency of the

windshield. Replacing glass with better property materials seems to be the only solution for vehicle applications in which weight is a major concern.

Transparent ceramics are known to offer a combination of superior optical and mechanical properties as compared to conventional glass systems. As shown in Figure 1-5, transparent magnesium aluminate spinel, $MgAl_2O_4$, has a much higher damage resistance compared to conventional glass material.

Spinel has raised great interest because of its superior properties, such as high melting temperature (2135 °C), high hardness (16 GPa), low density (3.58 gcm^{-3}), high strength both at room temperature (135-216 MPa) and elevated temperatures (120-205 MPa at 1300 °C), high electrical resistivity, high chemical stability and high thermal shock resistance. [10]

In addition, spinel has a cubic structure and is thus optically isotropic. And it has demonstrated better optical properties than other transparent ceramics like sapphire and ALON.[11] Its manufacturing process can, in principle, be conducted at a much lower temperature, which would reduce the cost in fabrication.

The combination of chemical inertness and thermal stability also make spinel attractive as a substrate for metal nanoparticle catalysts such as Pt. Stable nanoparticle catalysts can be used in harsh conditions to stimulate chemical reactions of industrial importance. A substrate that is highly stable and that promotes stability of the metal nanoparticles can be used in a wide variety of processing conditions. While the viewport and substrate applications are quite different, the processing conditions and resulting

properties for both are dependent on the surface energies of the internal and external interfaces of the spinel. In the case of the window applications, surface energies play a key role in determining the grain growth character and boundary fracture strength. These, in turn, strongly relate to optical quality and fracture toughness, respectively.

1.2.2 Problem statement

1.2.2.1. Arguments of surface energy.

Surface energy is an important parameter in ceramic materials and plays an important role in determining processing and properties.[12–14] Studies on surface energy of spinel have attracted research interest and led to debates about which index planes are of the highest energy. Mishra et al. have conducted theoretical surface energy calculations on spinel using Coulomb and Born-Mayer potentials estimated from its infrared and Raman spectra and concluded that {111} planes are of lowest energy for $MgAl_2O_4$ spinel.[12] However, atomistic simulations with atomic potentials have been performed by Fang et al.[13] for low-index surfaces of spinel, where surface energy of {111} as found to be highest, and {100} to be the lowest with {110} in the middle. {111}, {110} and {100} low index planes were chosen for study because $MgAl_2O_4$ has a Zener Ratio of 2.43 with the Young's elastic modulus a maximum in <111> and a minimum in <100>. [14] Stewart and Bradt have also investigated the fracture behavior of single crystals of these orientation planes experimentally and thus estimated the surface energy to have the same trend as Fang et. al.[15–18] More recent single crystal fracture measurements support these general conclusions.[19]

If fracture tests were carried out on measuring single grain boundaries, through Griffith's criterion, fracture energy could then be correlated to grain boundary energy. Therefore, one could fabricate bi-crystals of different orientations to compare the surface energies of the two orientation planes on each side, through correlation between surface energy, grain boundary energy and fracture energy.

1.2.2.2. Lack of systematic study of dopants effect on spinel fracture behavior

Due to the complications in the sintering process of spinel, high-quality, low-cost commercial bulk spinel is not yet available for manufacturing. [20] In order to produce dense transparent spinel, porosity is required to be less than about 0.1% and the pore size is required to be less than 1/10 of the important wavelength. Sintering aids such as LiF are found to be essential for fabricating dense transparent spinel if expensive methods like Hot Isostatic Pressing are to be avoided. [20] These dopant ions will segregate along the grain boundary and thus change the grain growth and coarsening process. The residual dopants will alter the grain boundary structure and affect the mechanical properties. As shown in Figure 2(a) and (b), the LiF doped polycrystalline spinel exhibits a higher transparency but lower fracture toughness, since evidence of transgranular fracture was found, as shown in Figure 2(d).

As observed in Figure 1-6 (a) and (b), with LiF as a sintering aid, the transparency has been greatly improved. [21] However, as shown in (c) and (d), intergranular fracture has been observed with LiF added in the sintering process.[22] LiF as a dopant does have

both beneficial effects and drawbacks on the overall performance of polycrystalline spinel, however there is no systematic study conducted that has shown how and why the dopants' segregation behavior would have such significant impact.

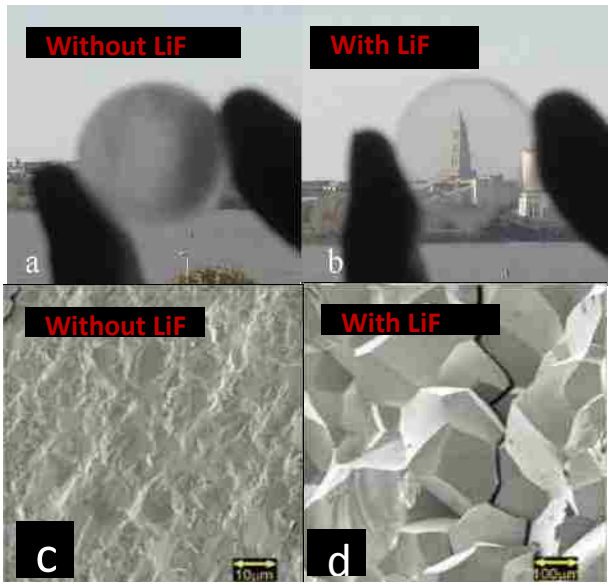

[redacted]

While studies of rare earth effects on spinel grain boundary mechanical behavior are limited, Yb has been shown to improve the strength of {111} grain boundary planes as compared to undoped boundary planes of identical orientation, presumably by lowering the boundary energy.[23] Specifically, a 30% increase in fracture toughness of individual Yb-doped {111}/{100} grain boundaries has been observed in spinel bi-crystal specimens as compared to identical undoped interfaces. Ordered Yb layer segregation was revealed in high angle annular dark field (HAADF) images, indicating a bond between Yb and Oxygen atoms on the {111} boundary plane. A similar bond was implied on the {100} boundary plane, but could not be demonstrated definitely.

However, there are no other systematic studies on how rare earth dopants will affect spinel.

1.2.2.3. Discrepancy of bulk materials fracture testing results

Previous studies on the doping segregation behavior effects on fracture properties in polycrystalline materials have been conducted on different materials, including alumina[24–27], magnesium oxide[28], silicon nitride[29–34] and silicon carbide[35].

Rare earth dopants have been observed to alter the mechanical behavior of the Silicon Nitride system, however there was a discrepancy in how these dopants could affect the fracture behavior in bulk system mechanical testing. Fracture toughness

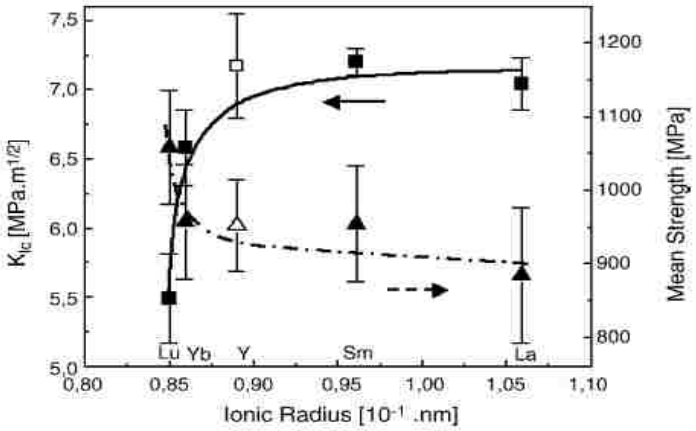

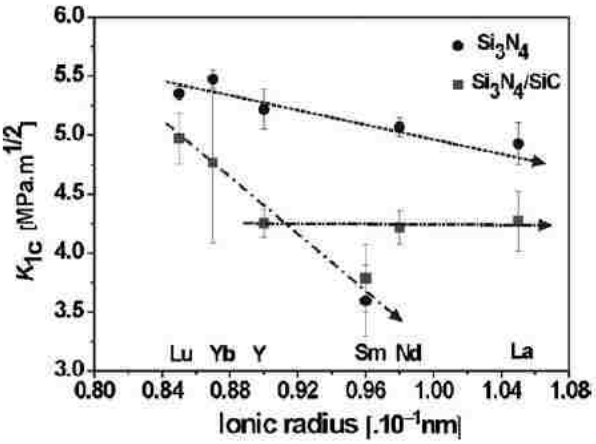

[redacted]

values have been observed to either increase or decrease with respect to size of the rare earth doping element cation ionic radius. [29,34]

In the study of Lojanova et. al.[34,36], fracture toughness of monolithic Si_3N_4 was measured to have a linear decreasing trend with increasing ionic radius of rare earth (RE) elements. The high fracture toughness with smaller RE elements (Lu, Yb, Y) was concluded to be a result of reinforcing effect of microstructure. In Lu-oxide containing sample, a higher volume fraction of a higher apparent aspect ratio of Si_3N_4 grains

measured leads to high frequency of extrinsic toughening mechanisms present like pull-outs and frictional bridges, which serve as crack energy dissipation mechanisms.

In the study of Satet et al.[29], fracture toughness was measured to have an increasing trend with increasing ionic radius of RE elements. Unlike Lojanova's study, all samples of Satet et al. were developed microstructurally comparable by altering sintering temperatures, eliminating the increasing trend of aspect ratio of Si_3N_4 grains with rare earth oxide addition. In his study, aspect ratio measured in Lu-oxide sample was higher, but showed the lowest fracture toughness, which indicates a higher effect of compositional factor than microstructure effect. In other words, in Satet et al.'s study, grain boundary composition and microstructure of the grain aspect ratio both contribute to the fracture toughness measured in the system, but composition factor plays a more important role in determining the fracture toughness. Moreover, the amount of crack deflection was higher in La-bearing ceramic than was observed in Lu-bearing ceramic in the comparison of crack opening path viewed in SEM. The debonding length is increased in the latter. Thus, it's a result of increased amount of frictional bridges and pull-out resulted from the interfacial chemistry alteration from Lu^{3+} to La^{3+} that leads to the increasing trend of fracture toughness. This fractography comparison also means that the interfacial strength was significantly weakened from Lu^{3+} to La^{3+}.

Therefore, traditional mechanical tests on bulk materials may result in conflicting conclusions when analyzing the doping segregation behavior at interfaces, because dopants at the grain boundary may simultaneously influence the grain growth, interfacial chemistry, and interfacial strength, which makes it impossible to build a

direct correlation between the grain boundary structure with the mechanical behavior. Therefore, in order to understand the rare earth dopants' segregation behavior on grain boundary mechanical properties, micro scale mechanical testing methods performed along fabricated tri-crystal grain boundaries have great value. Edge-defined bi-crystals are the ideal candidates since the loading orientation and the grain boundary orientation (potential fracture plane) are both well-defined during the in-situ fracture tests.

Chapter 2. Fracture testing of brittle materials

2.1 Bulk testing methods

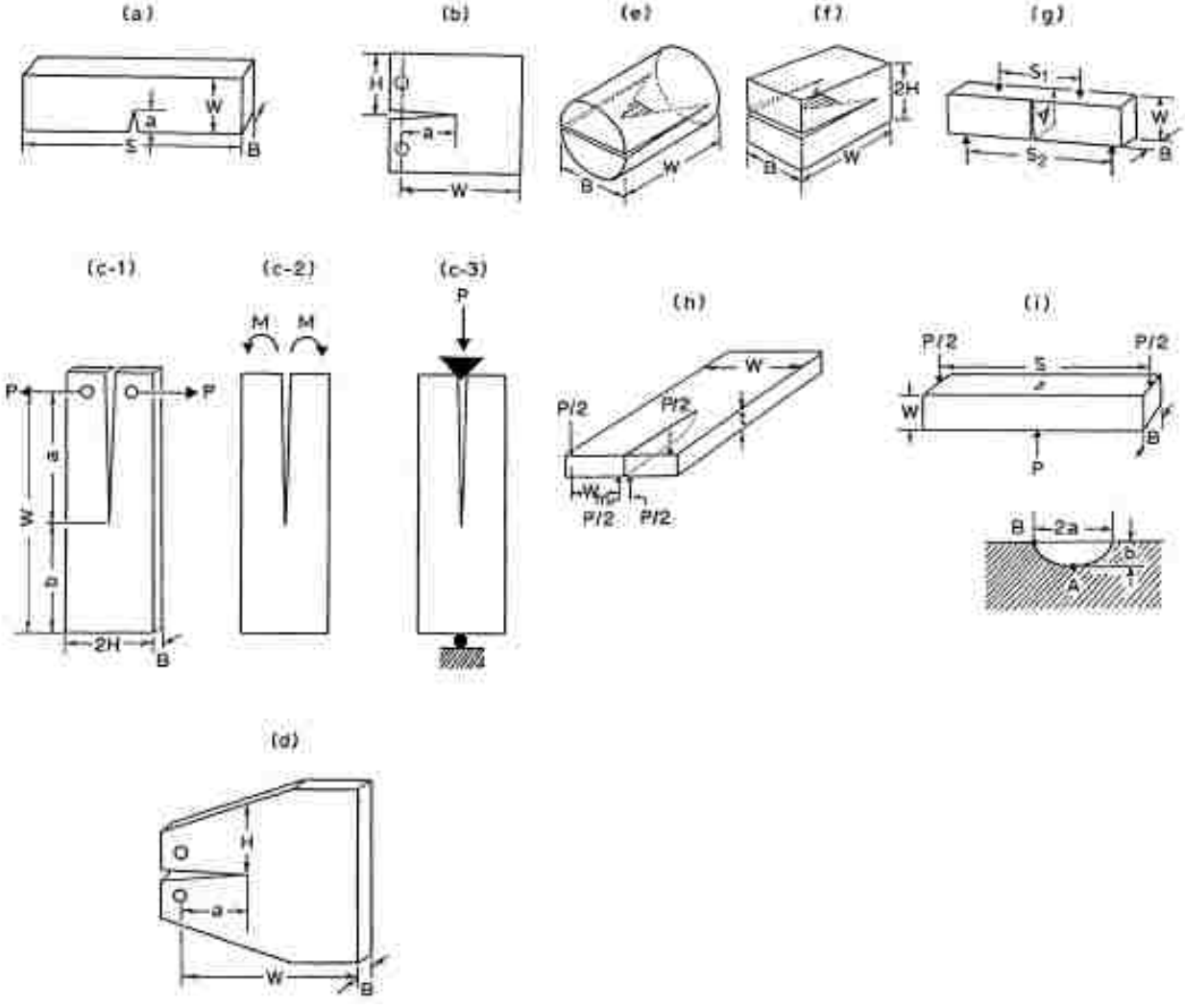

ASTM E 399 has standardized fracture toughness measurement techniques for metal systems at ambient temperature [37], including single edge notched bend (SENB) and compact tension (CT) specimens. Other methods like double torsion (DT), double cantilever beam (DCB) and chevron notch (CHV) specimen could be applied to brittle materials.

Table 2-1. Advantages and disadvantages of fracture specimens

Specimen	Advantages	Disadvantages
SENB	1. Simple specimen geometry 2. Less material required 3. Elevated temperature applicable 4. Large data of previous work	1. Difficulty in sharp precrack 2. Unstable crack growth (Difficulty in obtaining subcritical crack growth and R-curve measurements)
CT	1. Long crack length and relatively stable crack extension 2. Large data on previous work	1. Difficulty in machining 2. Difficulty in elevated temperature test 3. Delicate precracking procedure required
DCB	**Tensile loading mode:** similar to CT and more stable	1. similar to CT

	Constant bending moment mode: Constant Ki independent of crack length	1. Difficulty in attaching load arms, especially in elevated temperature
	Wedge loading mode: Elevated temperature capability	1. Difficulty of displacement measurement 2. Friction effects at the wedge loading point
	All loading modes:	Grooves to guide the crack extension. 1. Machining difficulty of the grooves 2. Crack interactions with the grooves 3. Effective thickness with grooves
CHV	1. Maximum load is the only measurement necessary	1. Delicate chevron notch machining 2. Chevron notch shape and size requirement for stable crack growth.

		3. Complication with rising R curve material.
DT	1. Ki independent of crack length	1. Constant Ki region affected by specimen dimensions. 2. Ki varies along the crack front curve. 3. Grooves required to guide crack.

As shown in Figure 2-1 [38] (a). SENB could be loaded in either three point or four point bend configuration. Geometric term Y has been given for both configurations with specific span ratio range. In (b), compact tension specimen or wedge opening loaded specimens are loaded in tension so that the crack tip stress is in opening mode. In (c), double cantilever beam specimen is demonstrated in three loading conditions: tensile, constant bending moment, and wedge loading. DCB specimens have been applied to brittle materials fracture testing. For tensile loading mode, DCB is very similar to CT specimen, just longer and thus more stable crack extension capability. In (d), a tapered DCB provides a constant K1 condition during crack extension by introducing a special taper to the specimen geometry. Chevron notched specimens are shown in (e-g): short rod, short bar, and bend bar. The maximum load recorded during test has been used to determine Ki, independent of crack length. Double torsion specimen is shown in (h). The advantages and disadvantages of each fracture specimen is listed in table 2-1.

In addition, fracture testing methods of brittle materials are listed in American Society for Testing and Materials Standard C 1421-15. [39] The geometries listed are primarily

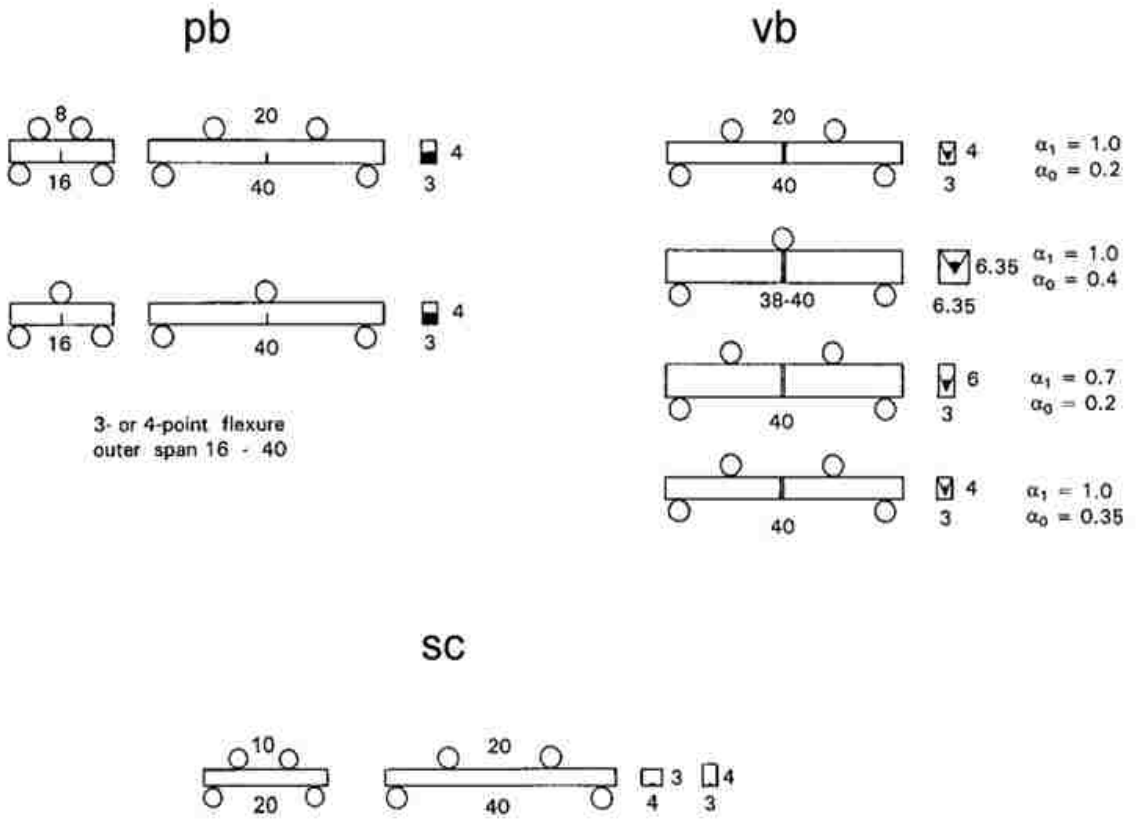

[redacted]

three or four point bend bar, the difference is in the precracks, as shown in Figure 2-2. The emphasis is in precracks because in brittle materials testing, the precrack is essentially important to introduce a valid Ki measurement. The precracks discussed here include a straight-through crack via bridge flexure (pb), a semi-elliptical surface crack via Knoop indentation (sc) or a chevron notch (vb). For pb specimen, a straight through precrack was extended by a special bridge compression fixture from median cracks associated with one or more Vickers or Knoop indentations or a shallow saw notch. For sc specimens, a surface flaw was introduced through a Knoop indenter and then

polished to remove the indents and the residual stress field. Vb specimens are valid only when crack stability is achieved, and in this conventional rectangular bar geometry, Kic measurement is independent of crack extension length; this is also described in previous ASTM E399 as CHV. Advantages, disadvantages and applicability are listed in table 2-2 as comparison. [39]

Table 2-2. Advantages, disadvantages and applicability of fracture specimens for brittle materials.

Specimen	Advantages	Disadvantages	Applicability
pb	1. Classic fracture configuration 2. Large precracks 3. Crack measurable	1. Special bridge precracking fixture 2. Large forces for precracking 3. Low force to fracture after precrack 4. Post fracture crack length measurement	Large sharp cracks
sc	Small precracks similar to natural cracks	1. Fractographic techniques for precrack measurement	Small cracks comparable to natural cracks in dense materials

		2. Skill and fractographic equipment required 3. Not appropriate for soft or porous materials 4. Not appropriate for coarse microstructure.	
vb	No need to measure crack length	1. Stable crack extension required 2. May not work for stiff materials with low fracture toughness or materials not susceptible to slow crack growth 3. Precision machining of notch 4. Requires stiff load train	Chapter 1. Large sharp cracks Chapter 2. Flat R-curve material

2.2 Introduction to small scale mechanical testing

Traditional fracture toughness testing methods developed for bulk materials are often difficult or impossible to apply directly to small-scale specimens, due to sample handling challenges and the small loads and displacements involved. Micro-scale

fracture toughness testing has particular advantages when the material or sub-region of interest has a scale below 100 μm. The micro-cantilever deflection test has recently emerged as a preferred method due to the simplicity of the cantilever beam configuration. It has been utilized to analyze a variety of materials such as thin films and individual phases within multiphase materials, and different phenomena including the influence of impurity segregation on grain boundary mechanical behavior. [40][41][23][42]

2.3 Micro cantilever with straight notch

The micro cantilever deflection test method was first introduced in 1988 [43] and has been widely used to determine mechanical properties of materials in nano/micro scales. The cantilever deflection test is widely used in micro scale mechanical tests, due to its simplicity in sample fabrication and well understood structure. It has been used in determining mechanical properties including Young's modulus, yield strength and fracture behavior of both brittle ceramics and metals.[41,42,44–46] Special techniques were utilized when milling the pre notch to ensure a sharp notch tip when fabricating micro cantilevers using Focused Ion Beam technique. And it has been shown to accurately capture the mechanical behavior of the materials with comparison to those in bulk phases. Etching and focused ion beam techniques are the most often used fabrication methods for sample preparation. Nano indentation hardware has been used to perform the deflection test. During the mechanical test, both load and displacement

data are recorded simultaneously until catastrophic fracture happens. A schematic diagram is shown in Figure 2-3.

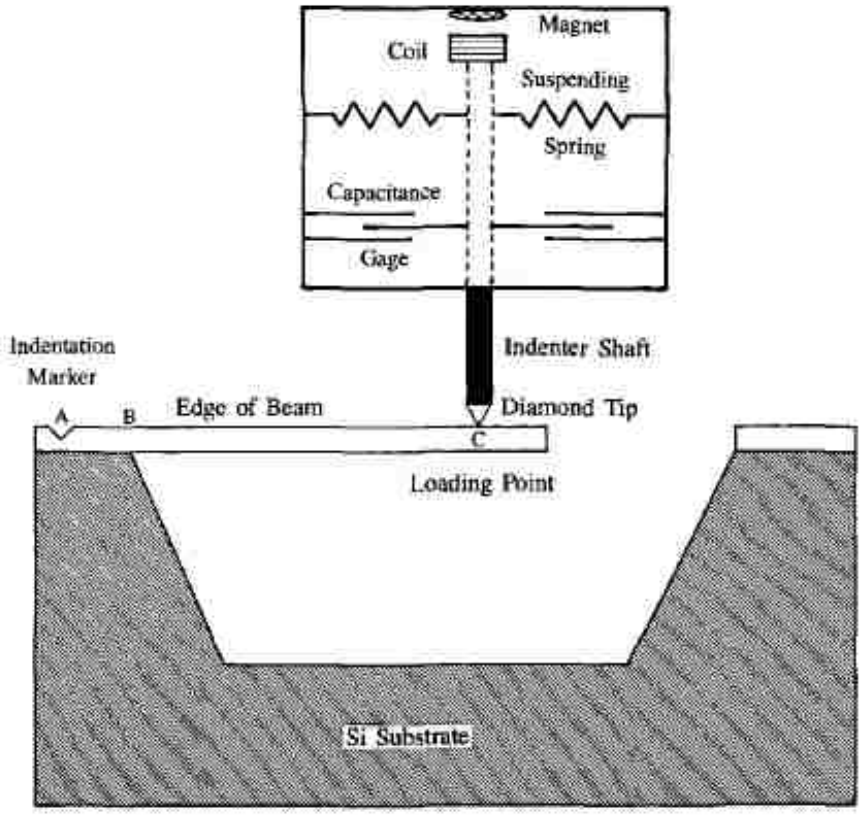

Figure 2-3 Schematic of nanoindenter loading system and a cantilever microbeam

[43]

In order to calculate the fracture toughness value of a material tested in the cantilever deflection configuration, the following equation has been used in previous studies.[40]

$$K_{IC} = \frac{6\,FL}{W^2 B}\sqrt{\pi a}\cdot f\left(\frac{a}{W}\right) \tag{14}$$

$$f\left(\frac{a}{W}\right) = 1.22 - 1.40\left(\frac{a}{W}\right) + 7.33\left(\frac{a}{W}\right)^2 - 13.08\left(\frac{a}{W}\right)^3 + 14.0\left(\frac{a}{W}\right)^4 \tag{15}$$

where F is the load when fracture happens, L is the distance between the prenotch and loading point, W and B are the thickness and width of the beam respectively, and a is the prenotch depth. Function f(a/W) is a dimensionless geometry factor used to correct for the prenotch length when the crack is not small compared to W. The parameters of this function can be determined by finite element analysis. This polynomial will vary

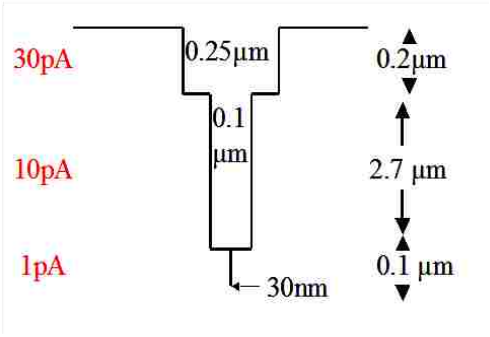

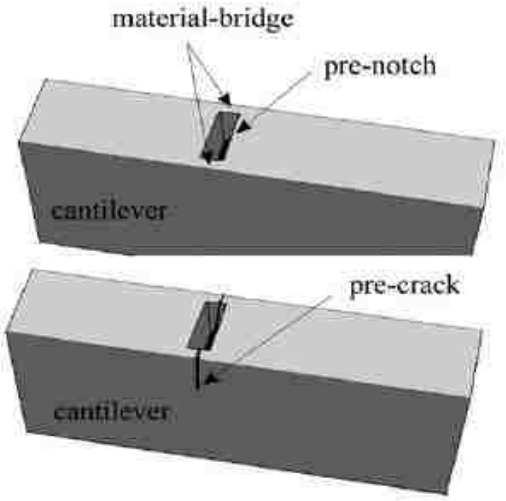

[redacted]

depending on specimen geometry. This equation is based on an assumption of a sharp prenotch with a notch root radius smaller enough to ensure the validity of the test results.

This notch in micro scale is usually fabricated with Focused Ion Beam technique in a low current setting, because precracking procedure in micro scale is not available like bridge flexure mentioned in bulk testing methods. Especially in brittle materials, once the crack initiated it will not arrest unless a crack stabilizer is employed, and such

mechanisms are not available in micro scale testing methods due to specimen handling and equipment limitations. The sharpness of the notch is essential in determining the accuracy of the fracture test. Linear elastic fracture mechanics has a preassumption that the precrack tip radius has a zero curvature. It was reported that a notch root radius of 250nm fabricated using FIB milling is not considered to be a sharp crack in micro size samples with a geometric dimensions of 10*10*50 um.[47]

In order to generate a sharp notch, a new technique has been used here involving three steps of FIB milling with decreasing ion beam current, which is shown in Figure 2-4 (a)

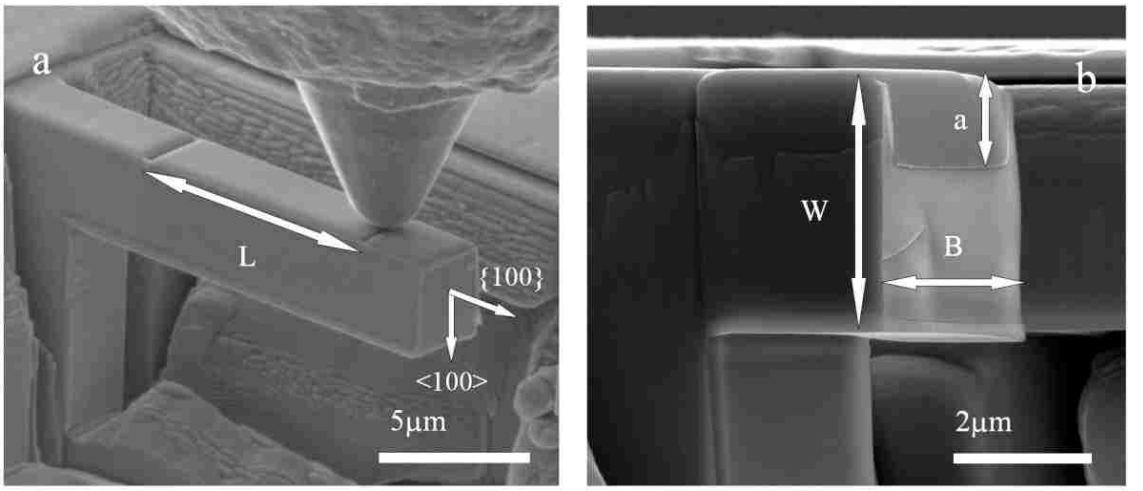

Another technique that has been used to generate a uniform crack and to induce a real sharp pre crack at the notch root is to leave thin bridges at both sides of the notch on the specimen, which are around 100-200nm in width, as shown in Figure 2-4 (b)[46]. The idea behind this is that the thin bridges will fracture at a small load, and the resulting cracks will merge and arrest when they reach the uniformly-milled area at

depth *a*. In principle, this will introduce a sharp crack that can then propagate at a higher load.

An in-situ mechanical test of a single crystal cantilever microbeam is shown in Figure 2-5[19]. The specimen was located with respect to the crystal orientation. The indenting direction is perpendicular to the top surface of the specimen, as shown in <100> direction in Figure Figure 2-5 (a) and the intended fracture plane is aligned with {100} orientation. And therefore each specimen was defined with two orientations, i.e. {100}, <100>. After the mechanical test, the fracture surface can be examined and the

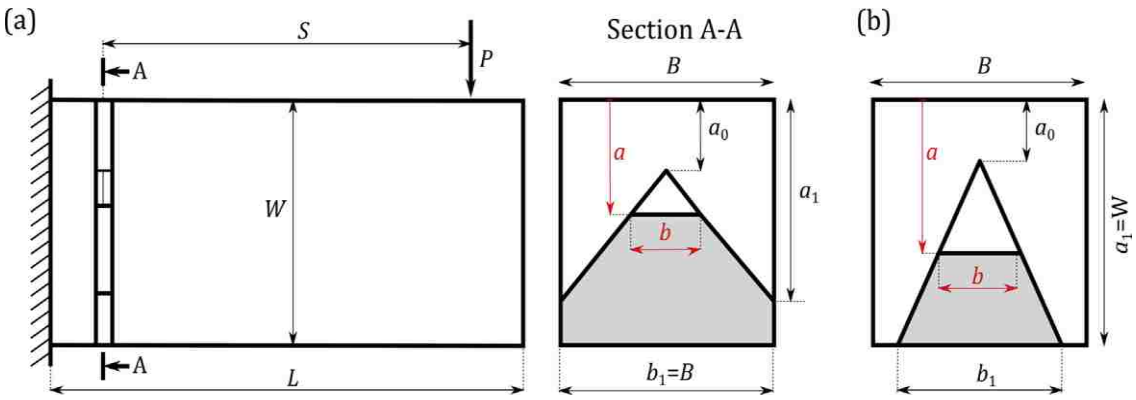

[redacted]

precrack length a, W, B can be measured respectively as shown in Figure 2-5 (b) in order to obtain the fracture toughness value using equation (16)

2.4 Micro cantilever with chevron notch

A micro cantilever deflection specimen with a chevron notch has been developed and utilized in small scale fracture toughness tests. [48] The advantage of a chevron notched specimen compared to a straight notch is that in micro scale, the straight notch machined with FIB is not as sharp as the crack introduced during fracture testing like

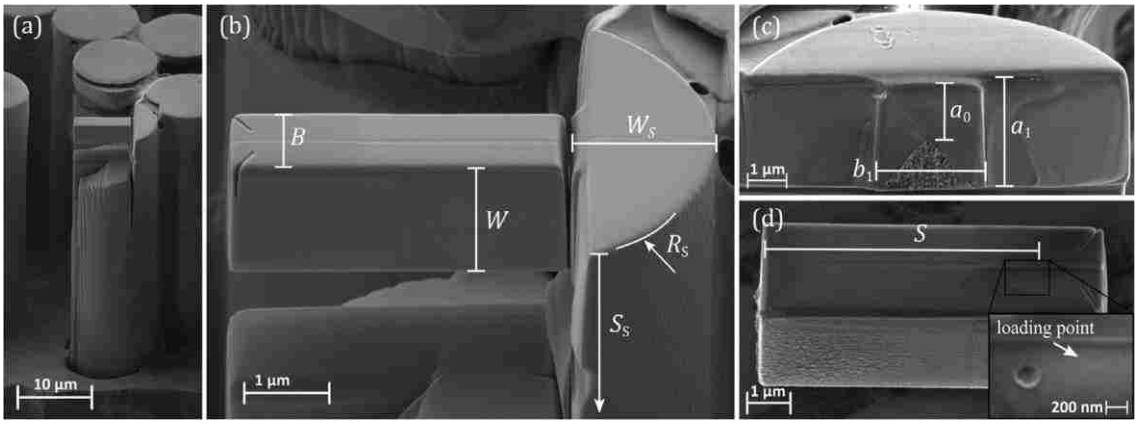

those of a chevron notch. Upon loading, the triangle shaped chevron notch tip will experience the highest stress and thus fail at first, introducing a real sharp crack. And as the load increases, the crack can extend in a stable manner with appropriate testing parameters set up. In a micro cantilever chevron notched specimen, the chevron notch is positioned with the notch tip facing upward, as shown in Figure 2-6 and 2-7. [48]

Therefore, when the beam is loaded in bending from the top, the crack tip experiences a tension mode loading. And therefore, fracture toughness could be obtained by,

$$K_I = \frac{P}{B\sqrt{W}}\, F_v(\tilde{a})$$

(17)

$$F_v(\tilde{a}) = \sqrt{\frac{1}{2\widetilde{b_1}} \frac{\widetilde{a_1} - \widetilde{a_0}}{\tilde{a} - \widetilde{a_0}} \frac{dC_V}{d\tilde{a}}}$$

Where all the dimensions are normalized as, $\tilde{a} = \frac{a}{W}$, $\widetilde{a_0} = \frac{a_0}{W}$, $\widetilde{a_1} = \frac{a_1}{W}$ and $\widetilde{b_1} = \frac{b_1}{B}$. And the compliance is dimensionless, $C_V = CEB$. This geometric term is determined with finite element analysis modeling. Maximum load could be obtained experimentally and thus is the only parameter that needs to be measured from a fracture test to determine the fracture toughness value.

We need to notice that in this testing method, a maximum load is only valid when the crack advances in a stable manner. The slope decreases to zero indicating the stability in a load displacement curve, shown in Figure 2-8. [48] The peak load reached in the test was immediately followed by unstable crack propagation. We can see that once the maximum load is reached, the indenter moves rapidly due to the programmed load function that was set to be monotonically increasing.

Fracture toughness was successfully determined with this method. The successful rate depends on machining the chevron notch to be thin enough to ensure a proper crack initiation with a lower load than the critical load associated with fracture equilibrium. Further studies in the same group involve a triangular cross section with a similar reversed chevron notch [49], the advantages of the later is that one could

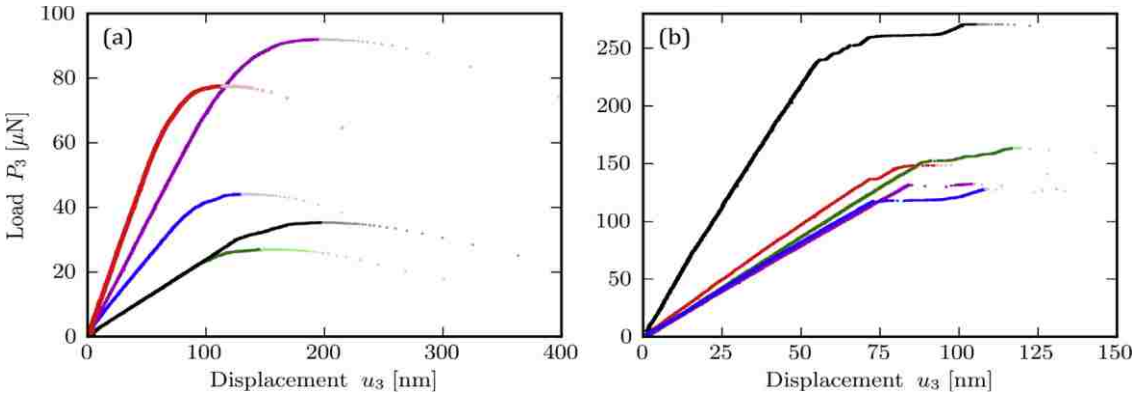

[redacted]

fabricate a fracture specimen in the center region of the sample surface, instead of a sample edge. The test configuration is shown in Figure 2-9.

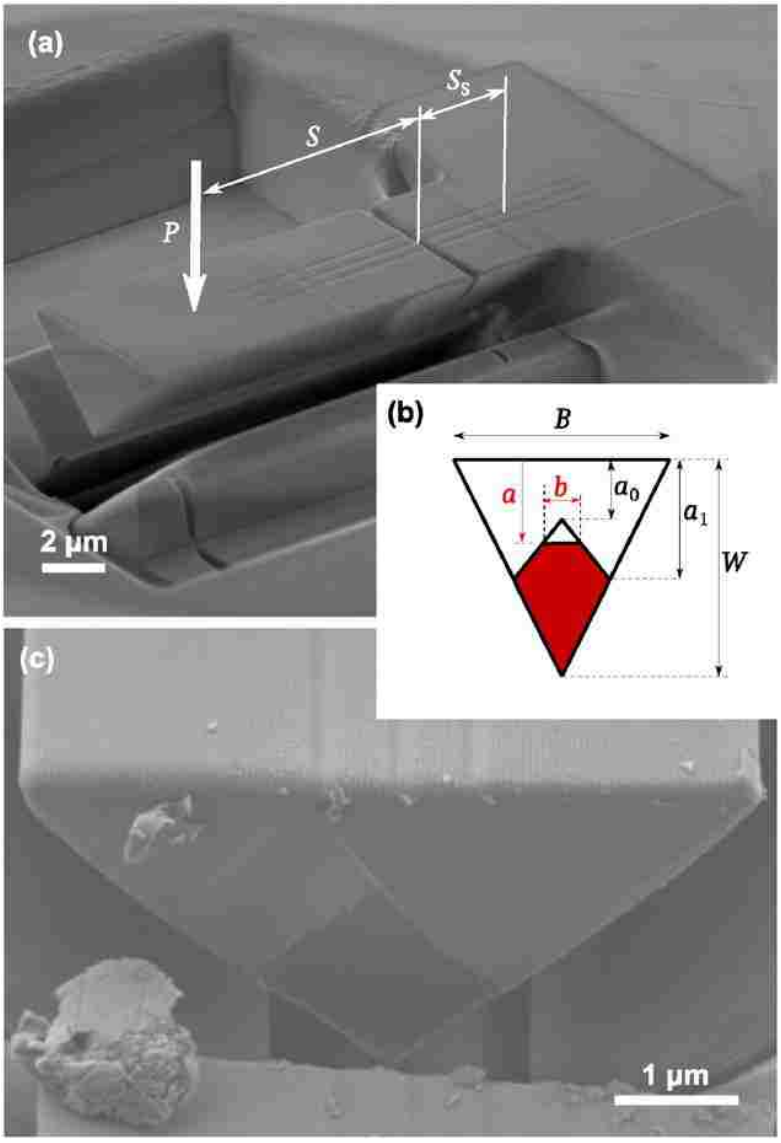

[redacted]

2.5 Clamped-clamped rectangular with straight notch

Another micro scale testing method has been developed is a clamped-clamped rectangular beam with a straight through notch, as shown in Figure 2-10. [50][51][52] The double clamped specimen is symmetric in nature and thus eliminated the mixed mode fracture in cantilever specimens. This geometry could achieve stability in certain test conditions. LEFM was utilized for evaluating fracture toughness as other testing

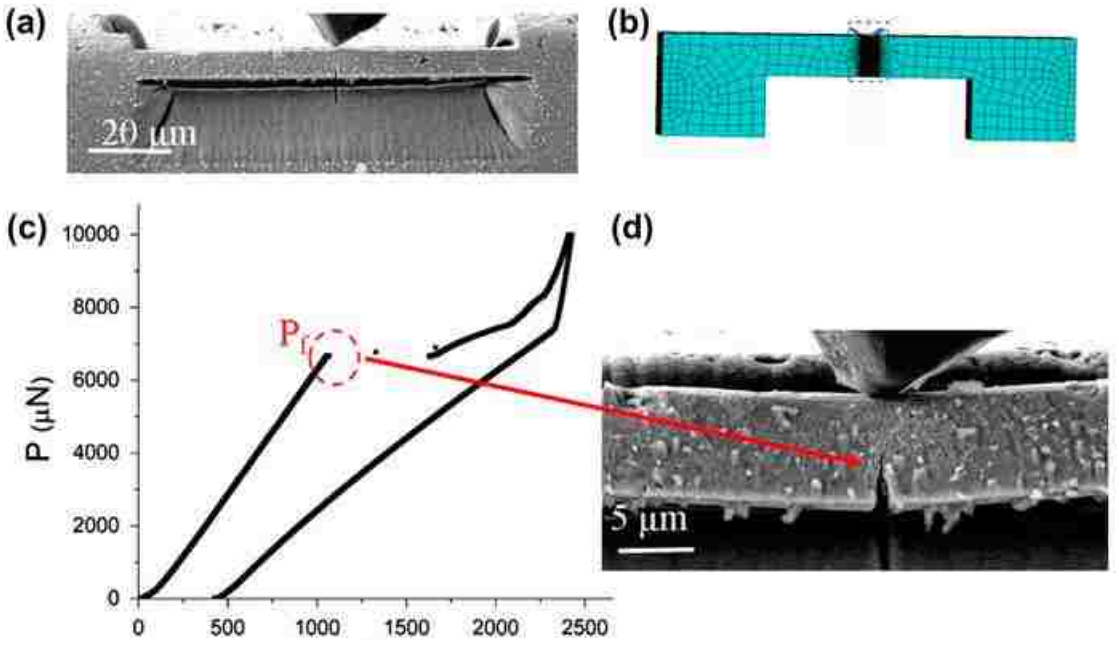

methods. Extended finite element analysis (XFEM) was carried out using ABAQUS. Kic measurements were obtained with the pop-in loads Pf shown in Figure 2-10 (c) in combination with XFEM analysis.

A disadvantage of this testing method is whether the pre machined notch radius (300nm in this study) is sufficiently sharp as that compared in a chevron notched

specimen, since the pop-in load is the only parameter used in evaluating Kic. Any bluntness of the notch will result in an overestimation of fracture toughness. In this testing configuration, not specialized preparation techniques were utilized to ensure the sharpness of the pre machined notch like those discussed in micro cantilever beams with a straight through notch, because this notch is located underneath the specimen. A correction could be applied to the results, however the accuracy of the correction is hard to evaluate. Furthermore, the evaluation of toughness results with XFEM and COD (crack opening displacement) methods have a difference with the same specimen. This error could be a combination of limitation of low signal to noise ration of DIC (digital image correlation) and the inability of the FEM to simulate the experiment condition in a non-planar crack propagation process.

Furthermore, the beam is notched on the underside in the center so it can be loaded from the top just like the microcantilever. The location of the notch requires that milling take place parallel to the notch front (i.e., from the side of the beam), thereby inevitably causing a notch that varies in shape and tip radius across the width of the specimen. This would be a significant drawback if it were not the case that properly chosen beam and notch dimensions are capable of creating conditions under which crack growth can be stable. Extended Finite Element Modeling (XFEM) showed that stability is enhanced when the beam is short and thick, and when the crack length is neither extremely short nor extremely long. The proper starting conditions result in the initiation of a sharp crack at the tip of the notch followed by crack arrest before catastrophic failure occurs. This sharp crack can then be driven forward by progressively

higher loads, much like the case of the chevron notch. The single edge notched clamped beam is therefore capable of multiple fracture events with a single specimen, and is suitable for measurement of R-curve behavior. The symmetric nature of the bridge beam design promotes pure Mode I loading at the crack tip, and should help to guide crack growth in a direction perpendicular to the beam's major axis. Like the chevron notched microcantilever test, analysis of a bridge beam test requires extensive modeling.

A secondary failure mode is also possible with the bridge beam design: fracture near the two clamped ends of the beam where the bending stresses are very large. A theoretical analysis of this failure mode shows that it is possible to reduce the likelihood of beam-end failure by careful selection of the beam and notch dimensions, and by elimination of flaws in the vicinity of the high-stress regions. Stable fracture emanating from a single underside notch has been demonstrated for specimens made of single crystal Si and (Pt, Ni)Al bond coat [53], with dimensions on the order of tens to hundreds of micrometers. In these specimens, crack growth is measured on the micrometer scale. In theory, the technique should also work for specimens at the single-micrometer scale for which crack growth must be measured on the nanometer scale, but this has not yet been demonstrated. In our laboratory we have had difficulty avoiding the secondary failure mode when working with micron-scale specimens for reasons that are unclear.

Chapter 3. Fracture toughness testing of doped spinel

3.1 Tri-crystal specimen fabrication

Two synthetic grain boundaries were investigated in this study, as shown in Figure 3-1 [54]. The boundaries were fabricated by diffusion-bonding three spinel single-crystals in a hot press (Thermal Technologies) at 1200 °C with an applied pressure of 10 MPa. The three single-crystals were edge-oriented with {111}, {100} and {110} surface planes, respectively. One of the grain boundaries thus fabricated had a {111} surface plane of one abutting crystal parallel to a {100} surface plane of the other and will be referred to as the {111}/{100} grain boundary. The other grain boundary comprised a {100} surface plane of one abutting crystal parallel to the {110} of the other and will be referred to as the {110}/{100} grain boundary. The grain boundary plane orientations are provided schematically in Figure 3-2. The diffusion-bonded sample was cut in half perpendicular to the grain boundary planes and then cleaned by ultrasonication. One half was doped with europium by soaking in europium nitrate solution and then dried, while the other half was left undoped. Both samples were annealed individually at 1600°C for 4 hours in a reducing atmosphere (forming gas). The samples were cooled

rapidly (~500°C/minute) from the annealing temperature to 1000°C. The cooling rates decreased with furnace temperature and, thus, the furnace reached 50°C in 15 minutes. Since the grain boundaries and free surfaces are identical in the two samples, the effect of europium on the grain boundary characteristics can be identified without any ambiguity. The annealed samples were polished and grain boundary orientations were confirmed with the aid of electron backscattered diffraction (EBSD; Hitachi 4300).

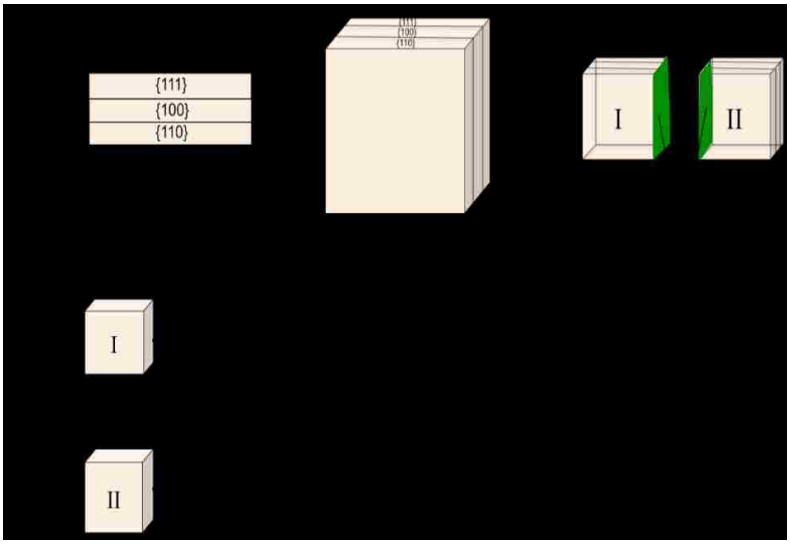

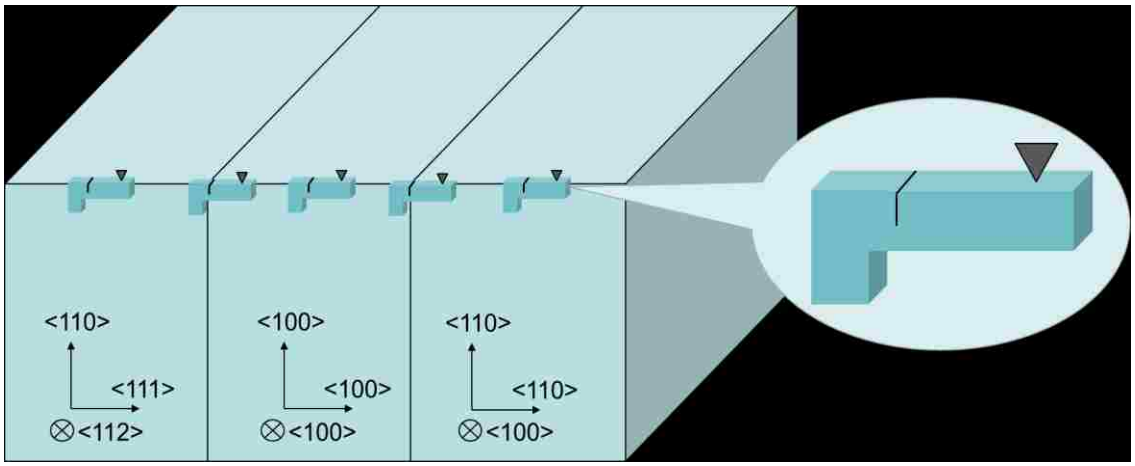

3.2 Improvement of micro cantilever test

In our study, micro cantilever deflection testing method was utilized to measure spinel grain boundary fracture toughness, due to its simplicity in sample fabrication, well understood structure and reliability, since relatively large amount of application with

micro cantilevers has been carried out in previous works. By aligning the pre notch at the location of the grain boundary, we could guide the fracture in the plane of the pre milled notch and then obtain the fracture load value from the transducer sensor during the mechanical test. Adjustments and improvements have been made in this study

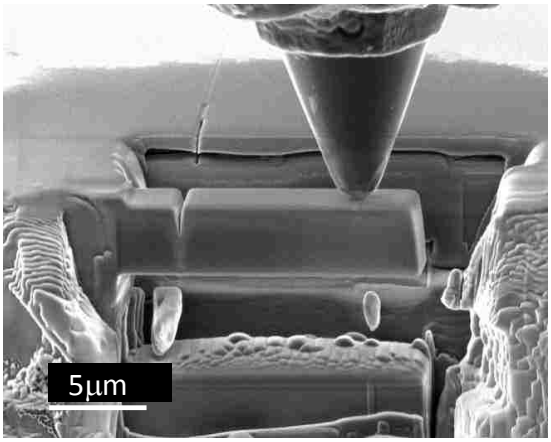

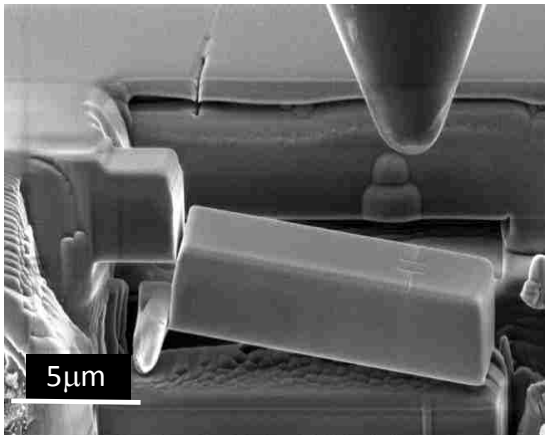

tailored to our current fabrication equipment, accurate loading point alignment, material elastic properties, milling rates and cantilever geometry. A geometric correction factor has been derived specifically in this study independently based on our finite element analysis modeling work carried out with ANSYS Mechanical APDL and FRAC 3D. This improvement is made in consideration of the material stiffness information embedded in the finite element analysis model to accurately capture the behavior of the structure during fracture testing experiment.

3.1.1 Sample fabrication

In preparation for cantilever fabrication, the top and side surfaces of the tricrystal were manually polished to create a 90 degree edge. Micro-cantilever beams were then fabricated by focused ion beam (FIB) milling using an FEI Scios Dual Beam system (Ga^+ ions, 30keV, 0.5-30nA). The microcantilevers were nominally 12 μm in length, 3 μm in width and 3 μm in height, as shown in Figure 3-3. In practice, the total length was greater than 12 μm to avoid the need to make contact with the mechanical test instrument precisely at the beam edge. For single crystal measurements, the entire cantilever beam was positioned within the respective crystal away from the grain boundaries. Three single crystal orientations of undoped spinel were tested: {100}<100>, {110}<110> and {111}<110> as defined by the ideal fracture plane and loading direction, respectively. At least three cantilever beams for each grain boundary and single-crystal arrangement were fabricated.

In all cantilevers, an ion-milled pre-notch was created to control the site of crack initiation. For the bicrystal cantilevers, EBSD was utilized before milling to correctly locate the grain boundary, the position of which was then marked using a low current ion beam. For certain orientations, the grain boundary location was confirmed using phase contrast or by second phase precipitates seen in the scanning electron microscopy (SEM) mode of the FIB instrument. The pre-notch was milled to a uniform length, with thin ligaments intentionally left on both sides of the notch.[46] To ensure a sharp crack tip, we reduced the ion milling current from 30 pA down to 1.5 pA.[44] SEM was used to confirm the notch radius as 10-20 nm, which is sufficiently sharp with

respect to beam dimensions to accurately evaluate the fracture toughness. For comparison, a previous microcantilever study on various silicon oxides, nitrides, and oxynitrides that used a similar notch radius determined that fracture toughness could be overestimated by as much as 20% if the side ligaments fail to create true crack prior to beam failure. [46]

An additional pair of shallow alignment marks were ion-milled 9 µm from the notch on the top surface of each cantilever beam to guide placement of the indenter tip during the mechanical test. These marks are visible in Figure 3-3. The distance from the marks to the base of the cantilever established the effective beam length of 12 µm, regardless of the physical beam length.

3.1.2 In-situ fracture test

A Hysitron PI85 picoindenter was utilized as the mechanical testing instrument. A cono-spherical indenter tip was used to minimize the tip impression on the top of the cantilever beam. During the mechanical test, load and displacement were both recorded. A linear load control function was employed with constant loading rate. As the load increased, the beam was deflected until fracture. The fracture load was captured in the output data which was sampled at a rate of 5 µN /s. SEM images of each post-test fracture surface were used to accurately determine the ratio of the pre-notch length (a) to the beam thickness (W). Then, the fracture toughness value (K_{IC}) was calculated using the equation (14), rewritten here for convenience.

$$K_{IC} = \frac{6\,FL}{W^2 B}\sqrt{\pi a}\cdot f(\frac{a}{W}) \tag{14}$$

in which *F* is the fracture load, *L* is the length between the notch and the loading point, *B* is the beam width, and *f(a/W)* is a dimensionless crack length correction term that is determined by finite element analysis.

3.1.3 Finite Element Analysis

A 3D finite element analysis (FEA) model was built using ANSYS Mechanical APDL, in which the beam dimensions were identical to the ideal experiment design, as shown in Figure 3-4.

Mesh refinement was applied at the notch area to ensure the convergence of the model. The model was built in the X-Y plane first, the area adjacent to the notch

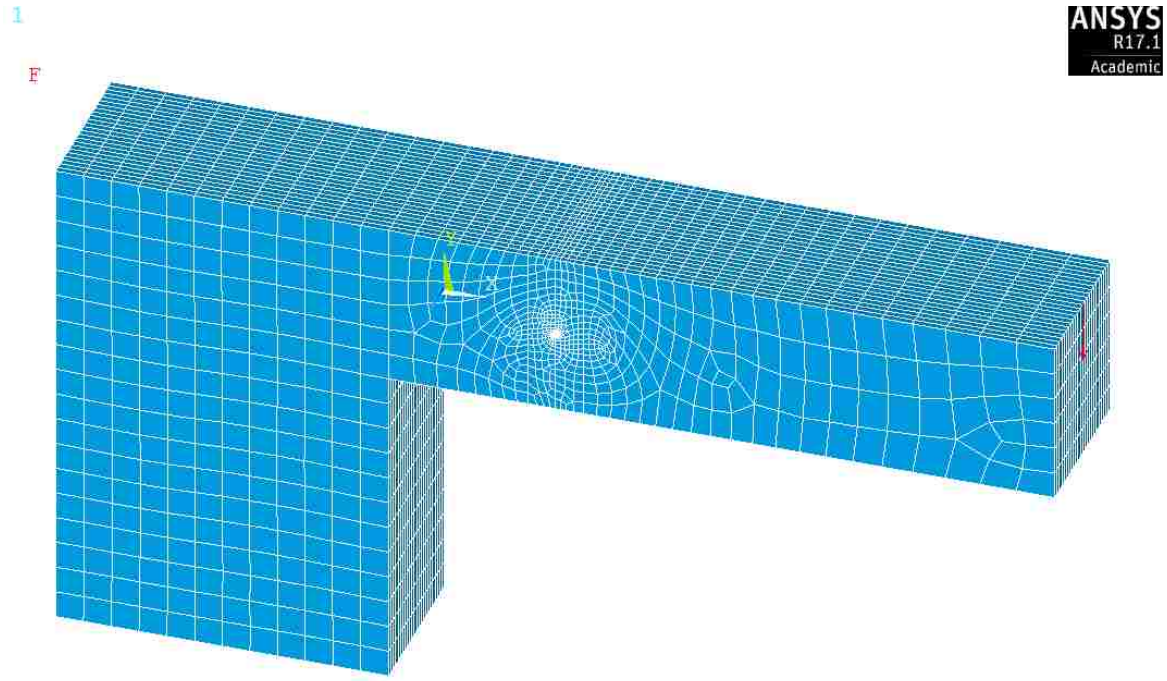

[redacted]

area was defined in order to better arrange these refinement near the notch, as shown in Figure 3-5.

A high order 3D 20-node structural solid element (SOLID 95) was selected after the extrusion of the 2D elements (PLANE 82), because of its high accuracy and tolerance of irregular shapes. A force load was applied to the top surface of the elements located at the free end of the beam 12 µm from the base, simulating the contact area of the

indenter tip. The material supporting the cantilever beam was also included in the model as the deformation of this volume affects the accuracy of the cantilever deflection. The size of the support region was increased until the solutions converged; the chosen model used a support that was half of the cantilever beam's length.

FRAC3D, a dedicated fracture toughness evaluation software package, was

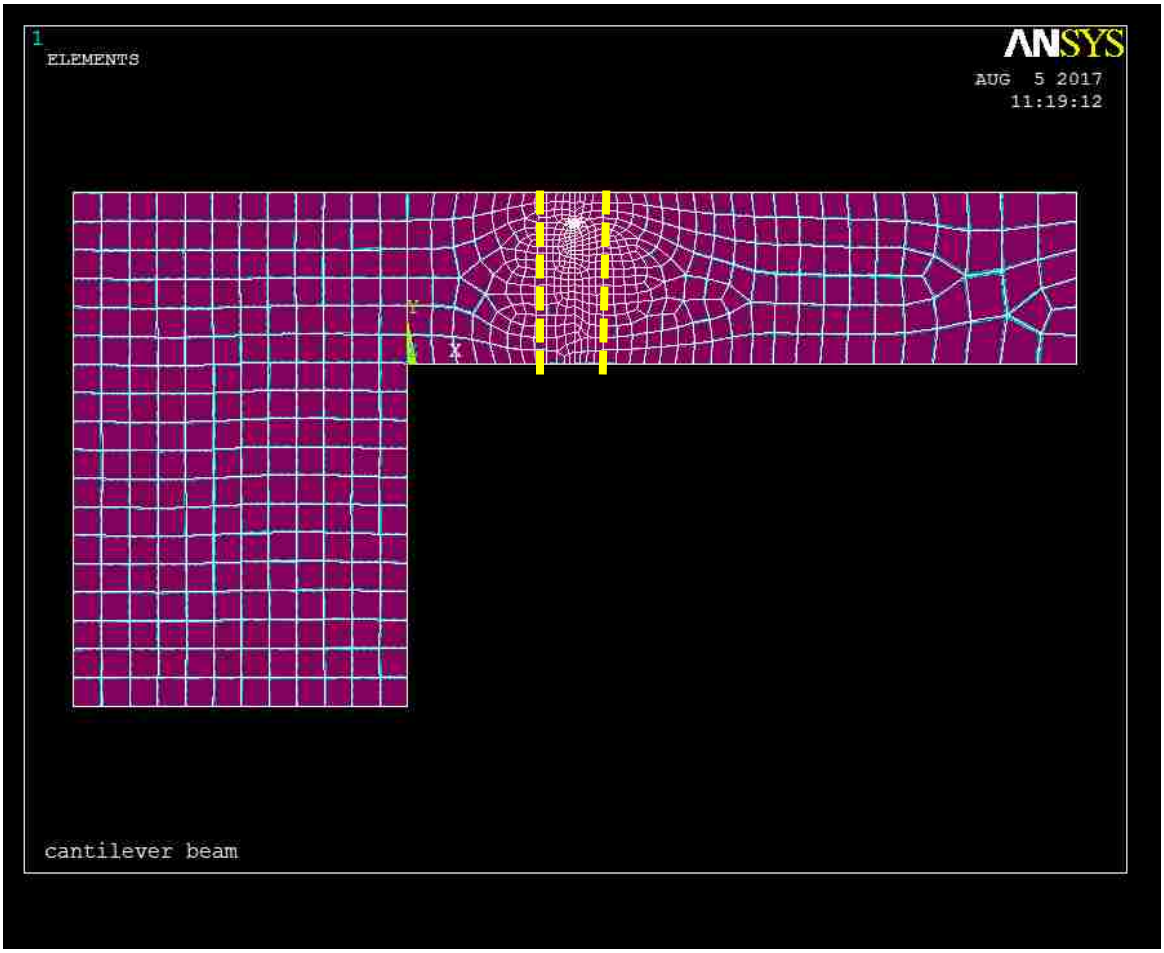

utilized to calculate the stress intensity factor value of the model.[55] In solving fracture mechanics problems, FRAC3D has certain advantages over many commercial codes by

utilizing enriched elements in evaluating the crack tip stress field, and, thus, well addresses the singularity and mesh refinement issues at the crack tip.

Multiple models with the same experimental geometry but with varying crack lengths were simulated and their stress intensity factor values were calculated with FRAC3D. In ANSYS APDL, crack length is defined as a variable, treated as a master key. Therefore, by changing this crack length variable, we could generate identically meshed models with different crack length. This makes sure that the FEA results are not affected by the difference in meshing conditions.

With the Ki measured from FRAC 3D for an increasing crack length, we could then derive the geometry factor term in Eqn. (14).

The finite crack size geometry factor (*f*) as a function of the notch length ratio (*a/W*) was then fit to these data with a polynomial (Eqn 18), this fit was generated by MATLAB.

$$f\left(\frac{a}{W}\right) = 1.55 - 6.61\left(\frac{a}{W}\right) + 38.52\left(\frac{a}{W}\right)^2 - 91.07\left(\frac{a}{W}\right)^3 + 83.04\left(\frac{a}{W}\right)^4 \quad (18)$$

Eqn. 18 applies for when *a/W* is between 0.2 and 0.5.

This polynomial was then used to calculate the fracture toughness (Eqn. 14) for the specific a/W ratio measured from each fractured beam.

3.3 Micro cantilever testing of Eu doped spinel

3.3.1 Method

In our study, micro cantilever deflection tests were employed to carry out the grain boundary fracture toughness measurement. By aligning the pre notch with the grain boundary, we could guide the fracture in the intended plane and thus evaluate the fracture behavior of the grain boundary. The {111}/{100} and {110}/{100} grain boundaries in both undoped and Eu-doped spinel were tested.

In addition, by capturing grain boundary fracture behavior of magnesium aluminate spinel and correlating the fracture energy, grain boundary energy and surface energy, we could establish an experimental method in investigating the fundamental surface energy of low index planes of spinel. Moreover, by adding different rare earth elements as dopants and evaluating the fracture behavior of grain boundaries through micro-mechanical characterization and atomic resolution scanning transmission electron microscopy, we could investigate how the choice of rare earth doping element affects the grain boundary structure, chemistry and properties systematically, which is essential in understanding grain boundary segregation behavior and beneficial in designing a material fabrication process with rare earth dopants to produce high performance materials.

3.3.2 Fracture Test results

Fracture toughness values and their standard deviations are plotted with respect to each specimen condition in Figure 3-7, and are also reported in Table 3-1. The single crystal fracture toughness values all have a standard deviation of 3% or smaller. Fracture of the {100}<100> specimens resulted in crack propagation perpendicular to the beam surface. During the {110}<110> and {111}<110> tests, the fracture plane was deflected from the pre-milled notch and, thus, a small correction was applied to these fracture toughness calculations to account for the decrease in the mode I stress intensity factor, K_I. [19].

Figure 3-6 and Table 3-1 also show the fracture toughness values for the undoped and Eu-doped spinel grain boundaries. The fracture planes were always coincident with the grain boundary planes during testing. The standard deviations for the undoped boundaries are similar to those for the single crystal specimens. The doped

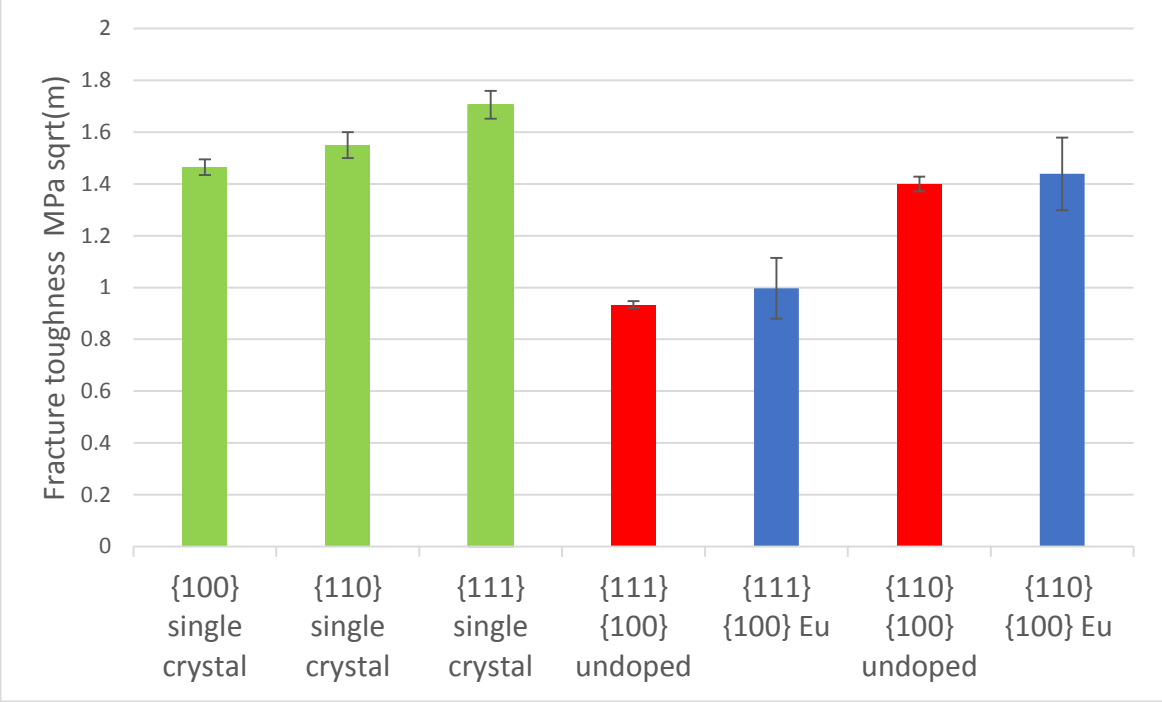

[redacted]

boundary values have standard deviations approximately four times larger. A higher fracture toughness value exists for the {110}/{100} grain boundary as compared to the {111}/{100} grain boundary for both the undoped and Eu-doped spinel. Little to no difference in fracture toughness is evident between the undoped and Eu-doped spinel grain boundaries that have the same orientation.

Table 3-1. Average fracture toughness results tri-crystal spinel

Orientation	{100}<100>	{110}<110>	{111}<110>	{111}/{100}	{110}/{100}	{111}/{100}	{110}/{100}
Condition	Single Crystal	Single Crystal	Single Crystal	Updoped	Undoped	Doped	Doped
Fracture toughness ($MPa \cdot m^{1/2}$)	1.46 ± 0.03	1.55 ± 0.05	1.71 ± 0.05	0.93 ± 0.01	1.40 ± 0.03	1.00 ± 0.12	1.43 ± 0.14

3.4 Discussion on surface energy and grain boundary energy

3.4.1 Single crystal

According to the Griffith fracture criterion for brittle materials, external energy is required when forming new surfaces and this external energy corresponds to the fracture energy measured in a fracture test. [3] A high fracture strength, or in this case fracture toughness, therefore corresponds to a high surface energy. In the single crystal tests, the beams were fabricated and tested in {100}<100>, {110}<110> and {111}<110> orientations to probe the {100}, {110}, and {111} surface energies, respectively. The average fracture toughness measurements derived from the microcantilevers match

with the most common trend reported in the literature for macroscopic single crystal spinel fracture toughness measurements made with conventional bend bars, wherein the {110} fracture plane has a slightly higher fracture toughness than the {100}, and the {111} fracture plane is significantly higher.[18] The high average fracture toughness of the {111} tensile axis specimens indicates that this plane has the highest surface energy of the three planes tested. The fractography trends for the single crystal beams are also in general agreement with published reports from conventional bend testing: the {100} cleavage plane is always smooth, the {110} plane is somewhat less so, and the {111} plane is associated with significant crack redirection during propagation. [15,16,18,56] These trends reinforce the conclusions stemming from the quantitative fracture toughness results. They also match very well with recent surface energy calculations that report a surface energy decrease from {111} to {110} and from {110} to {100} in pure single crystal spinel [13]. This is in direct contrast with older surface energy calculations that concluded that the {111} plane has the lowest energy of the three low-index planes [12]

3.4.2 Undoped interface fracture

When fracture occurs at a grain boundary, the energy required to cause crack propagation depends on the energy of the internal grain boundary as well as the energies of the exposed surfaces. Equations (19) and (20) relate the fracture energy, *G*, of both the {111}/{100} and {110}/{100} grain boundaries, respectively, as the difference between the energies of the free surfaces and that of the intact boundary.

$$G_{\{111\}/\{100\}} = \left(\gamma_{s,\{111\}} + \gamma_{s,\{100\}}\right) - \gamma_{gb,\{111\}/\{100\}} \quad (19)$$

$$G_{\{110\}/\{100\}} = \left(\gamma_{s,\{110\}} + \gamma_{s,\{100\}}\right) - \gamma_{gb,\{110\}/\{100\}} \quad (20)$$

$\gamma_{s,\{hkl\}}$ is the surface energy for the {hkl} plane and $\gamma_{gb,\{hkl\}/\{hkl\}}$ is the grain boundary energy for the {hkl}/{hkl} boundary. Fracture toughness is not an energy term per se, and is therefore not a direct measure of the surface energies, but differences in fracture toughness can indicate the underlying trends. The fracture toughness of the undoped {110}/{100} grain boundary is similar to that of the single crystal {100} and {110} measurements, for which there is no $\gamma_{gb,\{hkl\}/\{hkl\}}$ contribution. According to Eqn. 20, this would suggest that the {110}/{100} grain boundary energy is significantly lower than that of the respective free surface energies.

In contrast, the undoped {111}/{100} grain boundary's fracture toughness is significantly lower than the respective measurements of the {111} and {100} single crystals. This indicates that the {111}/{100} grain boundary has higher energy than the {110}/{100} grain boundary and, physically, there is relatively poor bonding between the {111} and {100} planes in this orientation.

The analysis above was completed for the undoped grain boundary fracture tests because the surface energies of the surface planes were elucidated from the single crystal fracture measurements. However, this method cannot be used when evaluating the Eu-doped grain boundaries as the single crystal fracture toughness measurements are now inadequate as reference values for the free surfaces.

3.4.3 Eu-Doped interface

Based on our fracture toughness results, we have not seen an increase of fracture toughness of the grain boundary with Eu doping compared to the undoped grain boundaries. And this is true for both orientation boundaries. The reason of this insensitivity of the toughness to rare earth doping at the grain boundary can only be answered combining other techniques to reveal the atomic level structure.

Further investigation of the grain boundary structure is made available through aberration corrected scanning electron microscopic analysis. The correlation of grain boundary structure and property is then established and will be discussed in great details in the following chapter.

Chapter 4. Direct correlation of grain boundary structure and fracture behavior

4.1 Grain boundary segregation behavior

The addition of dopants to spinel offers opportunities for tuning the interface energies and therefore the behavior. For example, rare earth dopants have been shown to segregate to free surfaces, stabilizing those surfaces. [57] Both the ionic size and ionic valance of the dopants were seen to determine the degree of stabilization, so proper selection of dopant type would be critical if this approach were to be put into practice. In general, among trivalent dopants larger ionic radius was associated with stronger segregation and influence on surface energy. For example, doping with La, the largest of the Lanthanide rare earths, was shown to have a very strong effect, making the {111} surfaces more favorable than they would be in undoped spinel.

In the case of internal interfaces, rare earth dopants have been observed to segregate strongly to grain boundaries and to alter the grain growth of polycrystalline spinel, promoting normal or abnormal grain growth depending on the selection of dopant and, in some cases, the heat treatment temperature.[58] Grain size and

uniformity determine optical quality, and grain boundary strength plays a role in determining fracture behavior.

4.2 Previous work on rare earth doped spinel

Previous studies on the effect of a rare earth dopant on spinel grain boundary

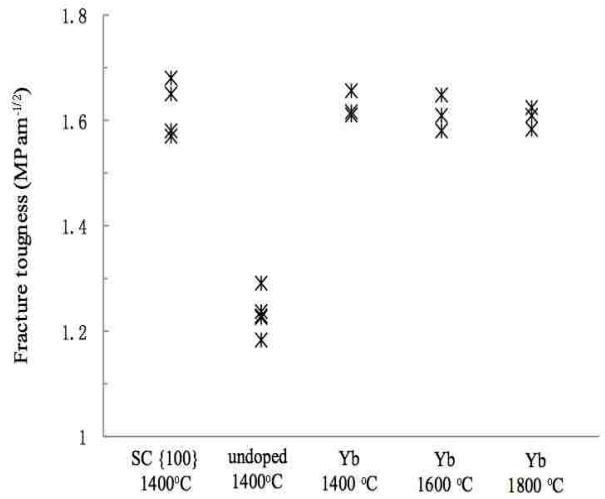

[redacted]

behavior was carried out in our research group. Ytterbium was added as a dopant in the sintering process of spinel bi crystals. [19]

The cantilever deflection test with the same nanoindentation system (Hysitron PI85) as our current study was applied to test the fracture toughness of grain boundaries on Spinel bi crystals. Only orientation {100}/{111} grain boundary was tested. In this case, Yb doping was found to affect the mechanical properties. Fracture toughness testing results with and without Yb added as a dopant was compared, the results are shown in Figure 4-1. Different annealing temperature effect was also

considered. As shown in Figure 4-1, the bi crystal grain boundary has a lower fracture toughness than a single crystal. By adding Yb as a dopant, the fracture toughness value was improved to the same level as single crystals. And the fracture toughness value of Yb-doped grain boundaries does not change with annealing temperature varying in the range of 1400 °C to 1800 °C. This result implies that an identical grain boundary structure may be achieved under this wide temperature range by adding Yb in the system.

High resolution electron microscopy characterization was carried out to analyse this grain boundary structure. As shown in Figure 4-2, HAADF micrographs of the spinel grain boundary in each doping condition were compared. Figure 4-3(a) represents an undoped spinel grain boundary, where there is no impurity segregation along the grain boundary, figure (b) shows a Yb doped grain boundary of the as-pressed doped samples. A periodic staggered monolayer segregation is observed. It must be noted that a

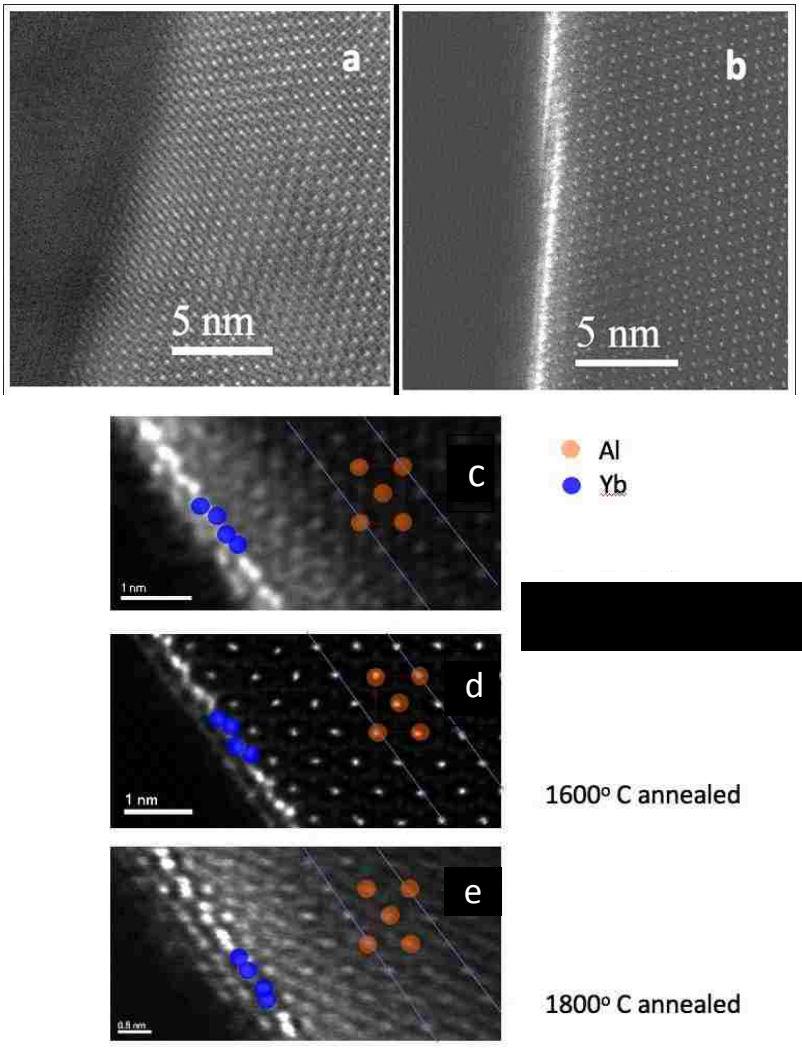

sufficient amount of ytterbium was introduced in the fabrication process, where other thermodynamically stable phases could form if they were energetically favored. Thus, it was concluded that the staggered monolayer structure is the most thermodynamically stable configuration of the ytterbium atoms in the spinel grain boundary and in fact it remains invariant over a large temperature range as shown in Figure 4-2 (c) (d) (e), which confirms the thermodynamic stability of such segregation behavior.

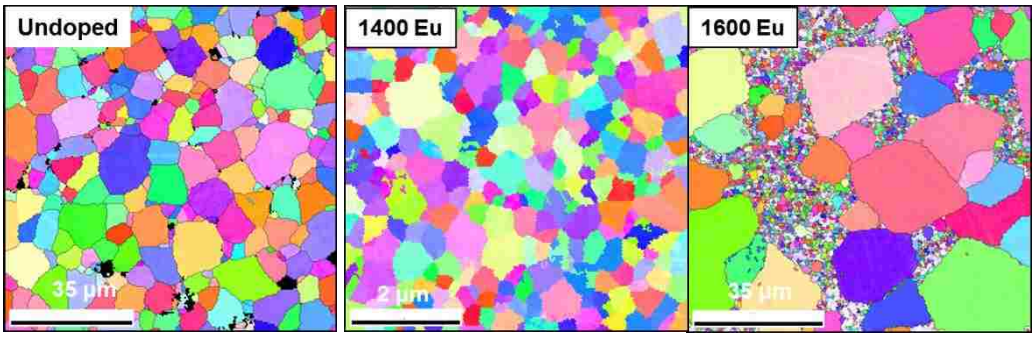

Figure 4-3 Grain growth of polycrystalline spinel for undoped, Eu doped heat treatment temperature at 1400 and 1600 °C

A prior study of grain growth in rare-earth doped polycrystalline spinel demonstrated that Yb and Eu have significantly different effects on grain growth kinetics. Yb-doped polycrystals grew in a normal fashion from 1400 to 1800 °C. In contrast, Eu-doped spinel underwent abnormal grain growth at temperatures greater than 1550 °C, as shown in Figure 4-3.[54] During abnormal growth, certain boundary planes became more prevalent than others. These results imply that Yb and Eu have different effects on boundary energy, that the Eu effect is temperature sensitive, and that segregation effects on surface energy are structure dependent. Yb is in a 3+ state and Eu in a 2+ state in spinel and the ionic radius of Eu is larger than that of Yb. Differences in both ionic size and ionic valance might be expected to result in

measureable differences with regard to effects on boundary energy. Therefore, in the present study Eu was selected as the doping element of interest, with heat treatment at 1600 °C to induce behavior unlike that of Yb. Furthermore, two different low index boundaries were created to explore the effect of structure on segregation, boundary structure, and boundary energy.

4.3 Eu doped Tri crystal grain boundary fracture behavior

4.3.1 Fracture results

Microcantilever fracture experiments were used to determine the relative fracture energies of different planes in updoped bicrystal boundaries, and doped bicrystal boundaries, as introduced in section 3.1. Scanning electron microscopy was used to analyze fracture surfaces. High resolution electron microscopy was used to elucidate the details of boundary chemistry and structure. From these results, an assessment of the relative surface energies of the low index planes with and without the presence of Eu could be made.

For the Europium doped grain boundaries, {111}{100} interface is measured to be 1.00 ±0.12 $MPam^{1/2}$ and {110}{100} interface is measure to be 1.43 ±0.14 $MPam^{1/2}$, as shown in Figure 3-6 and Table 3-1.

4.3.2 Fractography

The contact end of each cantilever beam was broken off to expose the fracture surface for observation with SEM. As mentioned above, all {100}<100> oriented single crystal micro cantilever beams had a planar fracture surface (not shown) while the fracture plane was deflected in the {110}<110> and {111}<110> oriented single crystal tests (not shown). No special features were visible on any of the single crystal fracture surfaces.

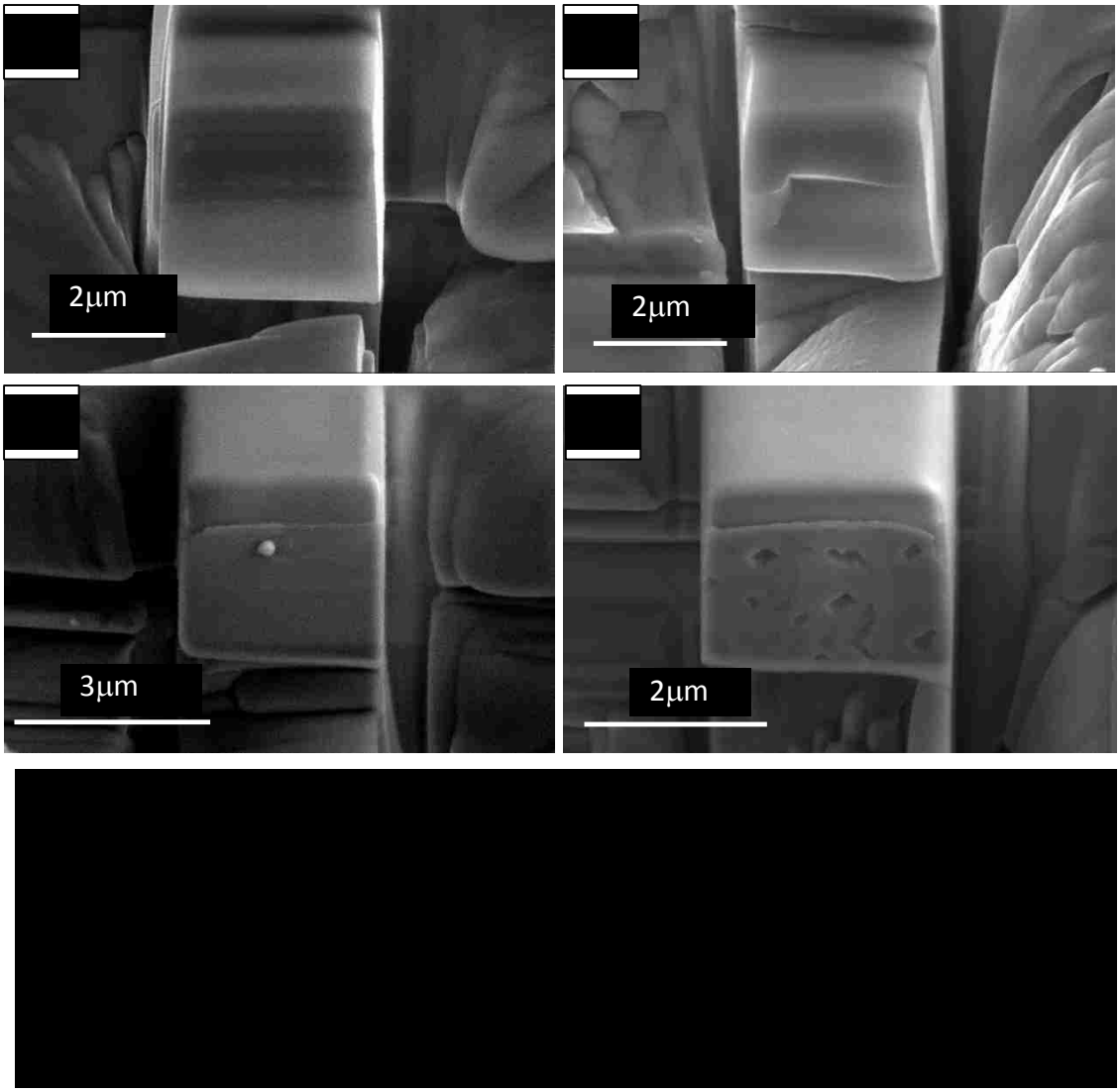

The fracture surface of an undoped {111}/{100} grain boundary shown in Figure 4-4(a) is a representative SEM micrograph showing that it also had a featureless 'clean' surface. All cantilever beams tested for the undoped-spinel grain boundaries have the same clean fracture surface, as expected. SEM observations of adjacent intact regions of the undoped tricrystal also showed no irregularities along the grain boundaries.

In contrast, precipitates were observed along the {111}/{100} interface of the doped tricrystal specimen at the surface of the sample. The precipitates covered a significant portion of the boundary and sometimes created a continuous layer. Microcantilevers were prepared only in regions without precipitates visible at the surface. A precipitate within a beam is not expected to affect the fracture measurement results unless the precipitate is located at the notch tip. Figure 4-4(b) shows an SEM micrograph of the cantilever fracture surface of a Eu-doped {111}/{100} interface, in which a precipitate-free fracture surface is visible. In contrast to the undoped {111}/{100} fracture surface, two of the doped interfaces exhibited a non-planar fracture surface like the one shown in Figure 4-4(b). In these cases, fracture initiated at the two ends of the notch tip where the ligaments existed, deviated from the ideal fracture plane in the center, and then joined to create a single fracture plane below the notch front.

In contrast to the {111}/{100} interface, the Eu-doped {110}{100} interface fracture surface was essentially clean, as shown in Figure 4-4(c). Precipitates were found along the grain boundary but with less regularity. Figure 4-4(d) is the {100} fracture surface of a {110}/{100} grain boundary cantilever beam that has voids left from

precipitates, which are much smaller than those observed in the {111}/{100} grain boundary.

4.4 Atomic resolution STEM characterization of grain boundaries

4.4.1 Atomic resolution electron microscopy

Samples for transmission electron microscopy (TEM) of the {111}/{100} and {110}/{100} grain boundaries of both undoped and Eu-doped spinel were prepared with FIB and polished with a Fischione Nanomill. At least three TEM specimens of each grain boundary type were prepared and analyzed**.** Atomic-resolution scanning-TEM (STEM) was conducted using an aberration-corrected (probe corrected) JEOL JEM-ARM200CF, operating at 200kV and equipped with energy dispersive x-ray spectroscopy (EDS; JEOL 100-mm^2 X-ray Detector). Slight crystal rotation during sample preparation required each sample to be imaged at three different tilting conditions to resolve the boundary structure: (1) grain boundary edge-on condition and (2,3) at each crystal's low-order zone axis that was closest to the edge-on condition. Qualitative EDS linescans were also completed across the grain boundary.

4.4.2 Electron Microscopy Results

All undoped-spinel TEM samples of both {111}/{100} and {110}/{100} grain boundaries exhibit planar and clean interfaces, as determined by STEM and EDS (not shown). As expected from the SEM observations of the doped tricrystal, precipitates

were found in many of the Eu-doped spinel grain boundary TEM specimens. EDS confirmed that these precipitates are a Eu-rich aluminate phase. Other than the few scattered precipitates found along the grain boundaries, the STEM images from all Eu-doped {110}/{100} TEM samples show that the boundary is clean and resembles the undoped spinel boundary of the same orientation (not shown). However, Eu was found to segregate strongly in all of the {111}/{100} boundary specimens. Figure 4-5 shows a high angle annular dark field (HAADF) image of the {111}/{100} grain boundary tilted to the edge-on condition. The high contrast at the grain boundary indicates a continuous layer of Eu-atoms, which was confirmed with EDS. When tilted to edge-on condition and to the zone axis of the {111} surface terminated crystal, as demonstrated in the

schematic in Figure 4-5. There is no evidence of Eu-preferred sites or ordering with the {100} terminated crystal at any tilting condition.

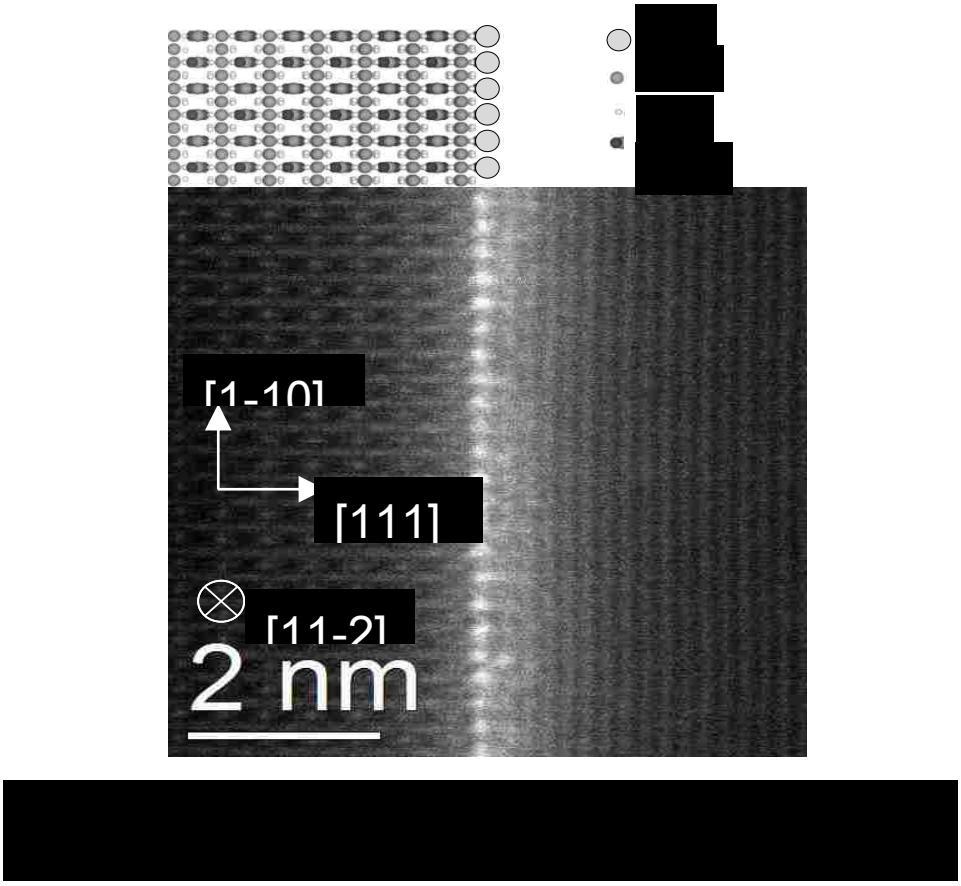

4.4.3 In-situ foil fracture

One of the Eu-doped {111}/{100} grain boundary TEM samples, prepared and imaged as described in Section 2.4, was returned to the FIB. A mechanical probe was used to bend the foil, causing it to fracture along the grain boundary *in situ*. The {100}-surface oriented crystal was completely eliminated during the failure, leaving the {111}-surface terminated crystal behind for imaging. The sample was immediately returned to the STEM for additional analysis using the methods described previously.

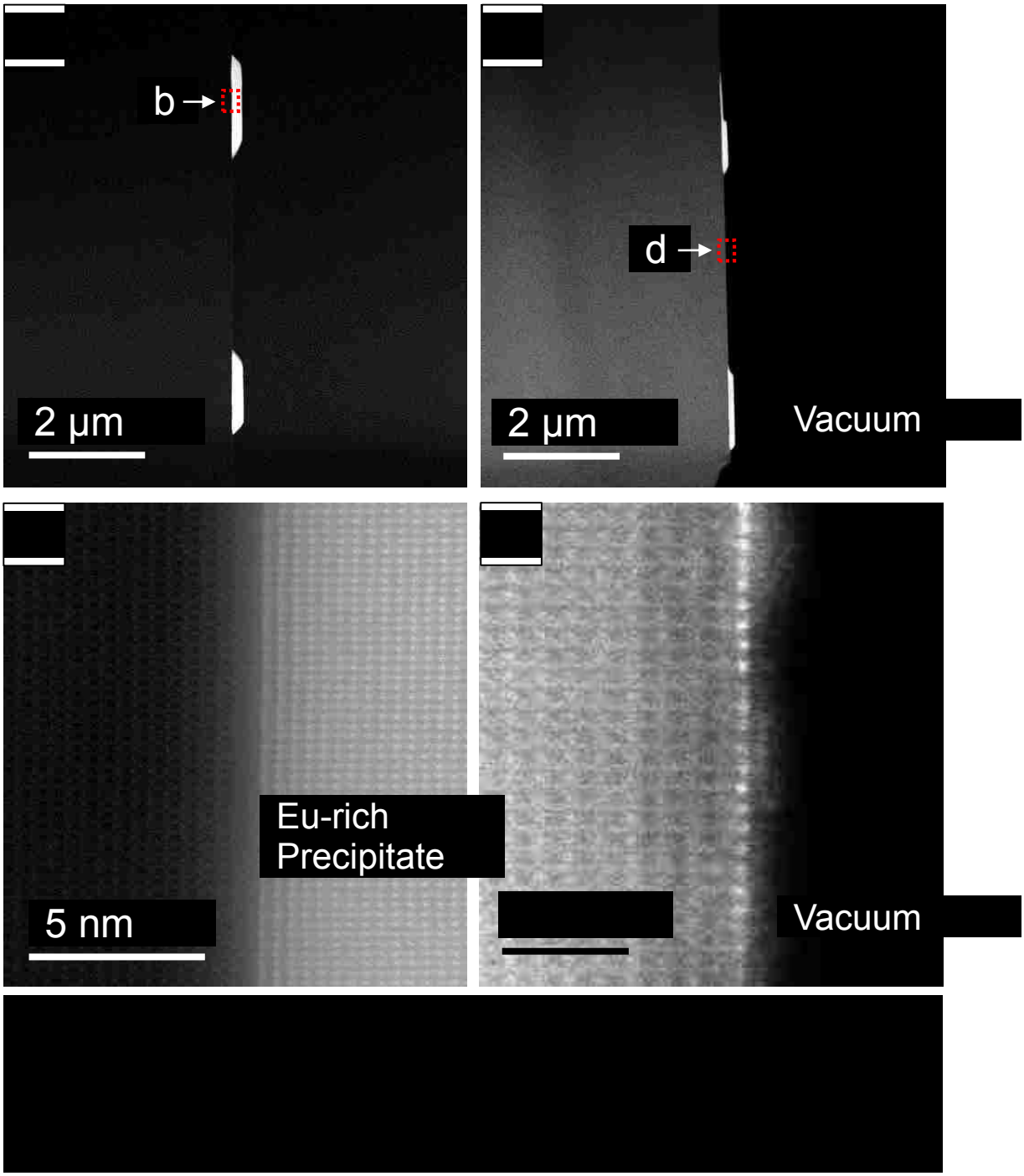

The thin foil of the Eu-segregated {111}/{100} boundary that was broken *in situ* enabled observation of an identical boundary before and after fracture. Before fracture, the grain boundary had the same structure and chemistry as seen in Figure 4-5. The

sample contained two Eu-rich aluminate precipitates on the boundary, as seen in Figure 4-6(a). The precipitates were faceted with two faces parallel to the grain boundary and showed coincident lattice matching with the {111}-plane (left crystal in Figure 4-6(a)) and showed coincident lattice matching at the interface, as seen in Figure 4-6(b). While the precipitate was also parallel with the {100} surface (right crystal in Figure 4-6(a)), no evidence of coincident lattice matching was observed between the {100} plane and the Eu-rich precipitate (not shown).

Figures 4-6(c) and (d) are HAADF images of the same sample after fracture. Figure 4-6(c) shows that the precipitates remained attached to the {111}-terminated surface. The fracture plane cut through the precipitates and then along the grain boundary interface. Figure 4-6(d) shows the exposed {111}-surface plane at Position d in Figure 4-6(c). The high contrast at the edge indicates that Eu-atoms remain bonded to the {111} plane after fracture. Failure must have occurred along the {100} plane or within a precipitate particle, leaving the bonds between Eu and the {111} plane intact.

4.5 Discussion and Future work

4.5.1 {111}{100} interface fracture

Eu segregates strongly to the {111}/{100} grain boundary (Figure 4-5), in line with the finding that this boundary has relatively high energy. However, as seen in Figure 3-6 and Table 3-1, the grain boundary's fracture toughness does not change with the addition of Eu. A layer of Eu was found to bond well to the {111}-surface, as seen in

Figure 4-5, but there is no evidence of ordered bonding with the {100}-surface at this interface. After fracture of the TEM specimen, the Eu-bonded {111} surface remains intact (Figure 4-6(d)) which suggests this particular bonding case is energetically favorable. Fracture occurred preferentially at the Eu-{100} interface, indicating that it is the weakest path. Therefore, despite the strong bonding between Eu and the {111}-spinel plane, the fracture toughness of the doped {111}/{100} interface is not improved as compared to the undoped case because the bonding is not improved across both sides of the interface.

This is unlike the Yb-doped spinel grain boundary (with same {111}/{100} grain boundary orientation) tested in [23] that exhibited a 30% increase in fracture toughness as compared to the undoped boundary. Cao et al. observed with STEM that Yb segregated strongly to the grain boundary and formed a staggered monolayer that bonded with both planes. This ordered grain boundary structure improved bonding across the interface to improve the fracture toughness. While Yb and Eu are both rare earth elements, they segregate and behave very differently in spinel grain boundaries. Both the ionic size and valence of the rare earth dopant influence segregation behavior[57], which alters the grain boundary chemistry, structure, and bonding strength.

While comparisons across material systems must be made with caution, previous mechanical studies conducted on silicon nitride samples that were doped with different rare earth cations support this general finding.[29] Satet et al. found the interfacial

fracture strength decreased with an increase in the rare earth dopant's radius. The change in interface strength was attributed to the decrease in cationic field strength associated with increasing radius. This agrees, at least qualitatively, with our results that the larger Eu dopant did not improve the fracture toughness compared to undoped interface but the smaller Yb dopant did. Valence may play an even larger role than ionic radius [57], but that influence cannot be evaluated independently by comparing only Eu^{2+} with Yb^{3+}.

The Eu-rich aluminate precipitates do not appear to significantly affect the fracture toughness measurements. As seen when comparing Figure 4-6(a) and 4-6(c), the fracture plane cuts through the precipitates. Therefore, the precipitate is weaker than the bonding between the precipitate and the {111}-plane, which is ordered (Figure 4-6(b)). While weaker, the precipitates do not cover the entire interface so we hypothesize that one must be positioned directly at the notch tip to significantly alter the fracture toughness value measured.

4.5.2 {110}{100} interface fracture

The {110}/{100} grain boundary in Eu-doped spinel shows a 'clean' grain boundary, similar to that of the undoped spinel grain boundary. The similarity between these interfaces reflects the consistency in the fracture toughness values measured. Eu shows no propensity to form stable bonds with the {100} or {110} plane under the experimental conditions. The undoped {110}/{100} grain boundary was low in energy in

comparison to the {111}/{100} grain boundary and, thus, there is no great driving force for Eu-segregation.

Small Eu-rich aluminate precipitates are found lightly distributed along the interface (Figure 4-4(d)), which caused a higher deviation in the fracture results (Figure 3-6). These precipitates are much smaller and more sparsely distributed than those found along the {111}/{100} interface (Figure 4-4(b)). The lack of Eu segregation and reduced number of Eu-rich precipitates demonstrate that Eu prefers the {111} plane, which has the highest energy of the planes tested in this system. This is reinforced by the tendency for the {110}/(100) interface to reconstruct to form {111} facets.[54]

4.5.3. Between the two interfaces

According to the atomic resolution STEM results, we found that with Eu dopants, a combination of different complexion types were observed at the {111}/{100} grain boundary, including a monolayer and Eu-rich precipitates. However for the {110}/{100} Eu doped grain boundary, we mostly observed a 'clean' grain boundary with Eu-rich precipitates sparsely distributed. This again confirms the conclusion that {111}{100} grain boundary is a higher energy grain boundary. In other words, its unstable nature causes the transition to multiple complexion types during annealing with Europium doping at 1600 °C. And our fracture results of these two doped interfaces is consistent with that of undoped interfaces, where the {111}/{100} doped grain boundary is lower than that of the {110}/{100} orientation.

According to our early study on Europium doped polycrystalline spinel, we observed a complexion transition with annealing temperature at 1600 °C[]. The cooling time is 4hrs in our experiment, thus according to TTT diagram, it is possible that during the quenching process, this high temperature complexion type has transformed into low temperature complexions, which left a trace of higher order complexion type in combination with lower temperature complexion types. Recommended further work includes study on lower annealing temperature specimens below the transition annealing temperature 1500 °C, or longer cooling time after annealing at 1600 °C.

4.5.4 Extending to Polycrystalline Spinel

The fracture measurements and TEM images presented are for select special grain boundaries. Polycrystalline samples will have many different boundary types that will have different energies. While grain boundaries are often defined by their misorientation, grain boundary planes have sometimes been found to be more descriptive of the grain boundary behavior. [59] Here, we have looked at three of the low index planes. In a previous report on polycrystalline spinel behavior, a Eu-doped specimen heat treated at 1600 ^{o}C had a grain boundary plane distribution (GBPD) that showed a high proportion of {111}-planes. In conjunction with our results that demonstrate preferential Eu-segregation to the {111}-plane, the creation of a Eu-bonded {111} grain boundary plane must lower the energy of the system. However, the relationship between Eu and the other abutting grain boundary plane will ultimately determine the total grain boundary energy and fracture toughness.

While the Eu-doped grain boundaries exhibit no superior intrinsic fracture toughness as compared to the undoped spinel boundaries, Eu-doping in spinel could still affect the fracture toughness of a polycrystalline specimen via influence on the microstructure. Schumacher et al. provided a time-temperature-transformation curve of the microstructural evolution in Eu-doped spinel, where a bimodal grain size distribution evolved with {111} planes dominating in the GBPD[58]. Here, we observed that Eu prefers the {111} plane over the others ({110} and {100}), which suggests that there will be a heterogeneous distribution of Eu in the grain boundaries. This supports the claim of Schumacher et al. that different grain boundary structures are responsible for the bimodal grain size distribution. Different dopants and the amount of doping could change the grain boundary plane distribution and, thus, change the microstructure. Individual grain boundary studies like the current work can help to separate the effects of dopant additions on intrinsic boundary toughness and extrinsic toughening mechanisms that can be influenced by microstructure control.

4.6 Conclusion

Grain boundary structure plays a significant role in determining the material fracture properties in bulk phase. Micro scale study on one single grain boundary enables us to understand the doping effect on grain boundary mechanical behavior. To relate a grain boundary property with the bulk phase material is crucial in guiding the material design and manufacturing. By statistical study of the complexion type

distribution, we could mathematically quantify and predict the macro scale properties based on the information of each complexion type studied in micro scale. Thus micro scale fracture toughness study on grain boundaries enables us to capture the grain boundary chemistry and structure, especially during sintering process with dopants and how this would affect the fracture behavior of the grain boundary complexions.

Single crystal fracture toughness measurements of magnesium aluminate spinel specimens indicate that among low index planes, the {111} single crystal plane is the highest surface energy orientation, and the {100} plane is the lowest, with the {110} orientation in the middle. These results are in agreement with most recent experimental and theoretical studies. Bi-crystal fracture test results have shown that the undoped {111}/{100} boundary orientation has a 43% lower fracture toughness than {110}/{100} boundary orientation. Eu-doped grain boundaries exhibit the same level fracture energy as their undoped counterparts, in contrast to a {111}/{100} boundary doped with Yb.

High resolution HAADF images suggest a mechanism underlying the fracture toughness results. For {111}/{100} doped grain boundaries, a combination of multiple grain boundary structures were observed including Eu-monolayer and Eu-rich precipitates. However for the {110}/{100} grain boundary, only a 'clean' interface was found between small, sparsely distributed Eu-rich precipitates. Neither case showed the staggered monolayer structure previously observed in the {111}/{100} Yb-doped spinel boundary. Although a strong bond may exist between Eu and the {111} side of a boundary, relatively poor strength of Eu-Eu bonds or bonds between Eu and the {100} boundary plane may result in the unimproved fracture toughness with Eu doping.

These results support the theoretical prediction that the surface energy of a {111} plane is more strongly affected by doping than the other low index planes. However, the larger Eu 2+ ion has a reduced tendency to segregate and alter surface energy than the smaller Yb 3+ ion. Valence may play a more significant role than size, so the present result does not necessarily contradict the general size trend observed in other material systems.

Eu doping did not have a positive effect of boundary strength in either of the two orientations examined. However, when extrinsic mechanisms are considered in fracture behavior of bulk materials, weaker grain boundaries can enhance energy dispersing mechanisms like bridging, crack deflection, and pull-out of grains. This was observed in Satet at al.'s work in the Si_3N_4 system, in which an increase in rare earth dopants size introduced weaker boundaries and thus an increasing fracture toughness.[29] It may be, therefore, that Eu is an attractive dopant to choose because Eu-doped grain boundaries may have unchanged bond strength between the grain boundaries while offering options for controlling grain growth by selection of processing temperature.

Chapter 5. Design of a symmetric rectangular beam fracture test technique

5.1 Limitation of present test techniques

We have introduced several attractive fracture test techniques in Chapter 2. All these micro scale fracture specimens were utilized to measure fracture toughness experimentally. However, they all have limitations and drawbacks in their own ways.

While micro cantilevers have a number of advantages for micro-scale fracture testing, the inherent mixed mode fracture cannot be neglected at large deflections of ductile materials and in anisotropic materials. In brittle material testing, this large fraction of shear mode in the initial load is often utilized as the fracture load measured from the experiment. Because no stable crack propagation or plasticity around the crack tip is available in brittle materials, this is when catastrophic fracture occurs. This is especially true when the FIB machined notch is not sharp enough. And the difficulty in producing a truly sharp crack by fatigue or other methods is not available in micro scale testing due to

specimen handling and equipment laminations. Another drawback of the cantilever is that the indenter inevitably slides on the top surface of the cantilever beam as the angle changes. This complicates the fracture load measurement in a ductile material fracture test as the beam plastically deforms.

Stable crack growth has been achieved in cantilevers machined with a chevron notch; in this way there is sufficient stability to reliably produce a truly sharp crack prior to the onset of failure [48][49], but the mixed mode fracture toughness effect due to the asymmetric geometry of a cantilever is still present. And the test becomes unstable immediately after the stable crack has been achieved, making this test only valid for one single fracture load output per specimen.

A symmetric clamped-clamped beam with a straight notch has been explored as a way of eliminating the mixed mode fracture, but its capability of stable crack growth is often limited because it may fail simultaneously at the beam center and beam ends, complicating analysis [51]. A way to further stabilize the fracture specimen needs to be investigated. Another drawback is the FIB machined notch tip cannot be treated as an ideal sharp crack tip in this straight notch configuration, which will again overestimate the fracture toughness results.

Moreover, regardless of the specific specimen shape, site-specific micro-scale sample fabrication typically requires techniques that are time consuming and costly. Generating sufficient fracture data to ensure statistical significance is often not practical for any configuration that results in a single data point per test specimen.

Therefore, new micro scale fracture test specimens are needed to address current

fracture specimen issues. We explored several fracture test configurations in micro scale. The design process, sample fabrication, advantages and issues are presented in the following two chapters.

5.2 3pt bend rectangular beam with chevron notch test

5.2.1 Design criteria

For traditional bulk poly-crystal ceramics, a symmetrical bending specimen configuration is always utilized. A 3pt bending chevron notched beam is described in

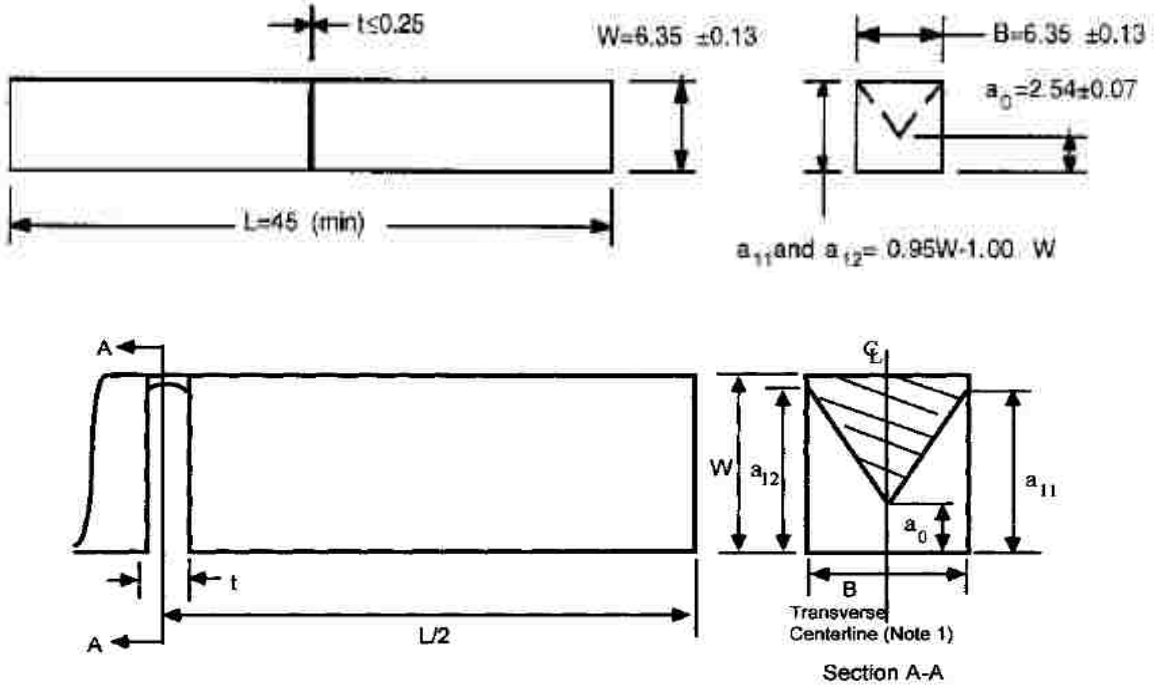

[redacted]

ASTM C1421-15 [39] for macro scale ceramic fracture toughness testing, as shown in Figure 5-1.

This symmetrical specimen configuration would eliminate the mixed-mode fracture loading in existed in cantilever specimens, and the chevron notch shape would induce a stable crack propagation that prevents the potential higher fracture toughness value that might be obtained from a simple straight pre-notch. In order to produce a test with stability, we followed strictly one of the standard test configurations reported in ASTM C1421-15, as shown in Table 5-1. The following equation is used to calculate the fracture toughness value:

$$Kic = f\left(\frac{a_0}{W}, \frac{a_1}{W}\right)\left(\frac{Pmax \cdot L\ 10^{-6}}{BW^{\frac{3}{2}}}\right) \quad (1)$$

Where, f is the minimum stress intensity factor coefficient as determined from specimen geometries, Pmax is the maximum force as determined from the load-displacement curve, L is the specimen length, B and W are the beam width and thickness, respectively. For $0.382 \leq a_0/W \leq 0.420$ and $0.950 \leq a_1/W \leq 1.00$ and a maximum error of 1%, the geometry factor f is given. Therefore, we chose parameters in our microscale specimen accordingly.

Other requirements in additional to the general geometries are listed in Table 5-2 in order to achieve a valid test.

Table 5-1 Specimen configuration and requirements for 3pt bending chevron notched beam ASTM C1421-15[39]

Test fixture	**L (mm)**	**B(mm)**	**W(mm)**	**a_0 (mm)**	**a_{11}, a_{12}**	**t (mm)**
3pt bending macro scale specimen	45 (min)	6.35±0.13	6.35±0.13	2.54±0.07	0.95W to1.00W	≤0.25

Table 5-2 Additional requirement for valid 3pt bending chevron notched beam test[39]

Chevron notch grooves on either side should meet	Tip of chevron shall be on the centerline	Difference between a_{11} and a_{12}, or the average of both	Test rate	Machine Compliance
≤ 0.3t	≤0.02B	≤ 0.02W	0.0003 to 0.005 mm/s	≤4.43×10^{-5} m/N

Using the focused ion beam technique in our experiment, we fabricated our 3pt bending microbeam with the chevron notch, where the specimen dimension is proportional to the standard test specimen dimension. The specific specimen dimensions that were chosen in our test are shown in Table 5-3.

Table 5-3 Specimen dimension selected in our micro beam fabrication

Test fixture	L (um)	B(um)	W(um)	a0 (um)	a11,a12 (um)	t (um)
3pt bending micro scale specimen	15	2	2	0.8	2	≤0.08

The Hysitron PI85 pico- indenter has been used in our test for applying the load. The test rate is we chose is 5 nm/s which meets the ASTM requirement listed in Table 5-2. The machine compliance provided by Hysitron of the indenter tip is 16.2×10^{-5} m/N, which is higher than the requirement suggested in the standard bulk system test. However, this compliance is sufficient enough for our experiment, as will be explained in details in later chapters.

5.2.2 Specimen fabrication

Focused ion beam milling is utilized to fabricate the specimen in micro scale. A complicated fabrication process involving the manipulator/needle and platinum deposition was needed to fabricate the free end specimen configuration, which is shown in Figure 5-2.

After milling the beam with the chevron notch in the middle, we mill away one end of the beam and leave a small ligament on the other side, as shown in Figure 5-3. Then the first step is to insert the needle and move it to the position right on top of the free end of the specimen, then use platinum deposition under a small current to glue

the needle on top of the specimen. The second step is to mill away the ligament on the right hand side so that the beam is lifted by the needle, as shown in Figure 5-3. Then we slowly move the needle downward, so that the beam comes into contact with the support material underneath, and we restrain the beam to the support using platinum deposition as a 'glue'. Step 4 is to mill away the part that connects the needle and the specimen. Then we extract the needle in step 5. Now the free end 3pt bending specimen is finished. The final step is to conduct the mechanical test with the nano-indentation system (Hysitron PI85) as shown in Figure 5-3.

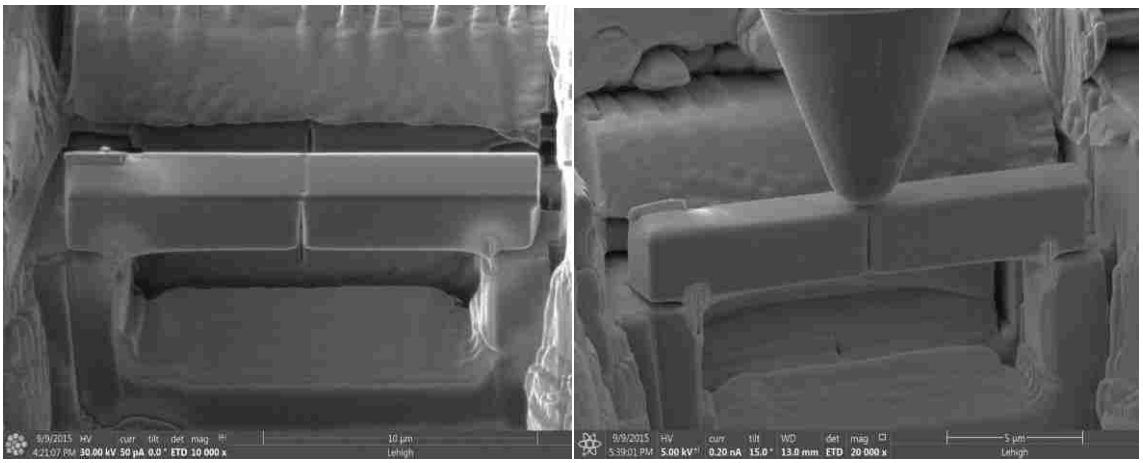

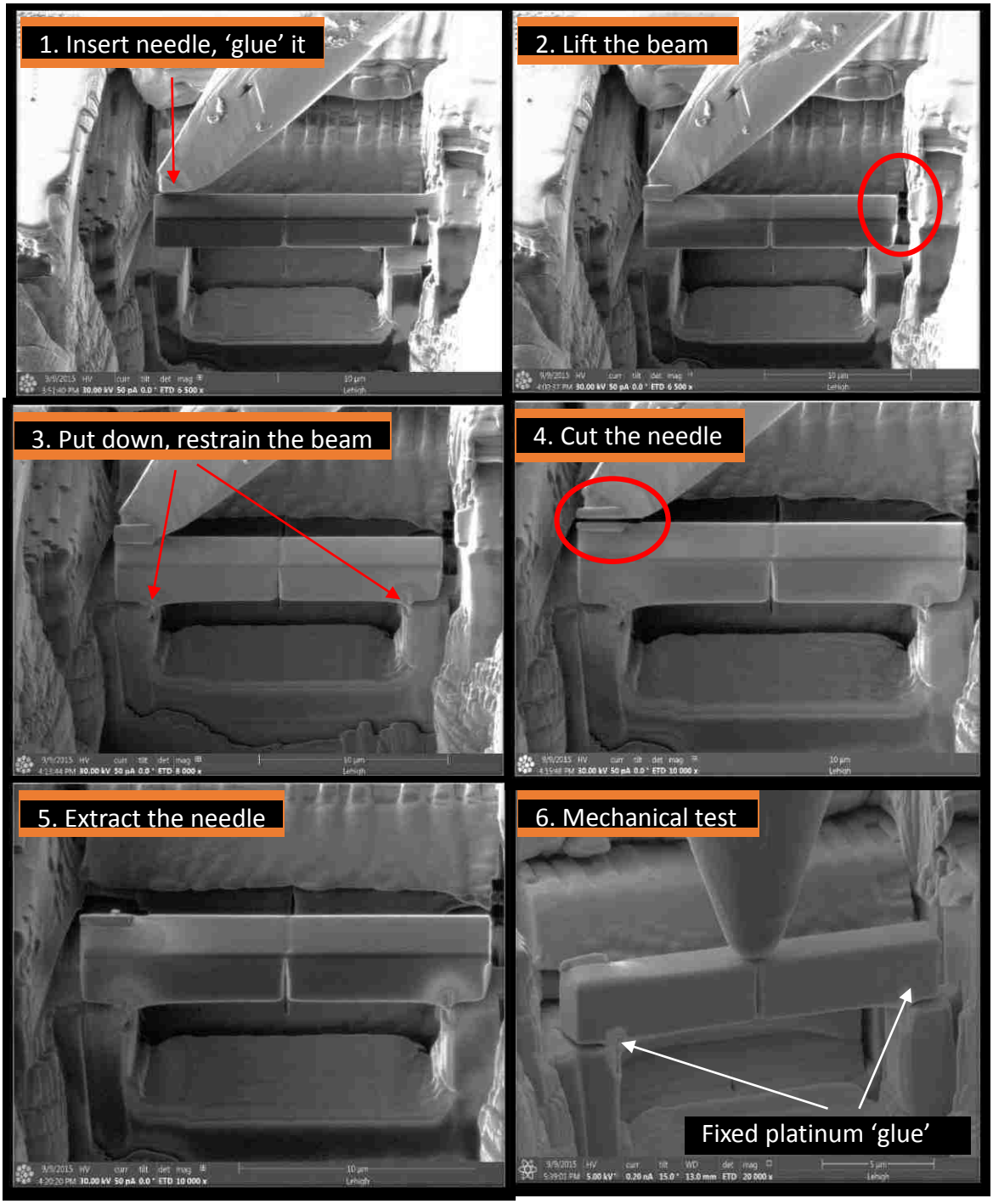

5.2.3 Limitation

As we can see, the fixed platinum glue on both sides of the specimen would break first when loading, since the platinum is much weaker compared to the testing material, but this would still affect the degree of freedom so that the boundary condition in our test is different from a true free-end 3pt bending test. And this complicated procedure takes a really long FIB milling time, and thus leads to high fabrication cost. Furthermore, the contact area between the bottom surface of the beam and the support is unknown, where the bottom of the surface might not be accurately parallel to the support, causing concern regarding the alignment of the loading direction on the specimen.

Therefore, a better approach to modify the configuration of our specimen is needed, and this is the motivation of a doubly clamped beam design in the next section.

5.3 Clamped-clamped rectangular chevron specimen

5.3.1 Specimen fabrication

As shown in Figure 5-4, instead of milling away the both ends of the beam, we keep them attached to the rest of the material, and thus achieve a clamped-clamped end 3pt

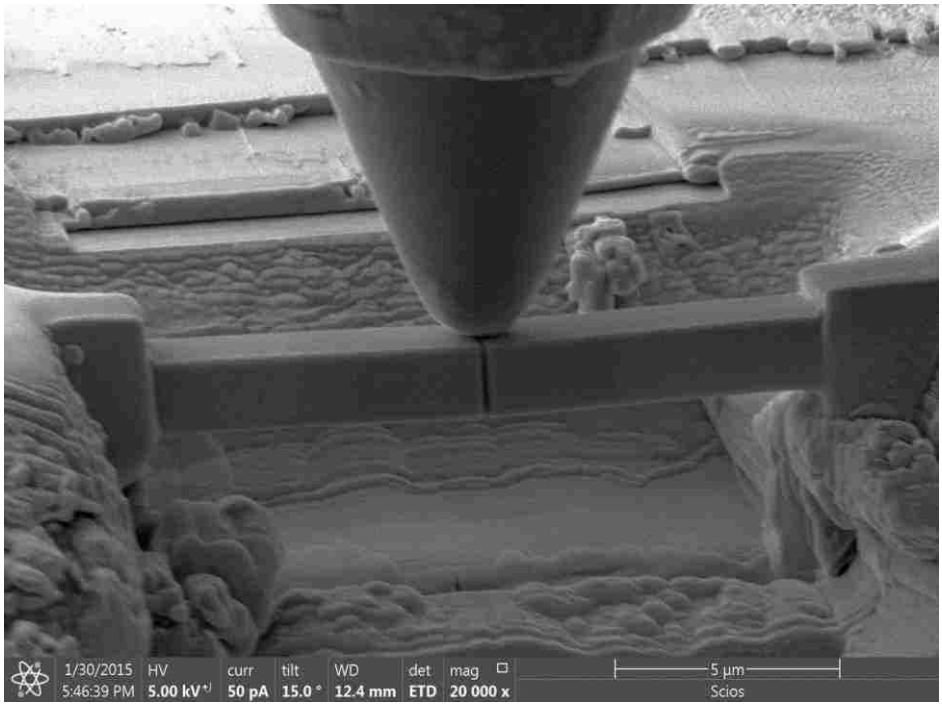

[redacted]

bending test configuration. The chevron notch was milled in the middle underneath the contact point of the indenter tip. This approach is easier to fabricate, which takes shorter FIB milling time and thus is relatively cost efficient.

5.3.2 Test results

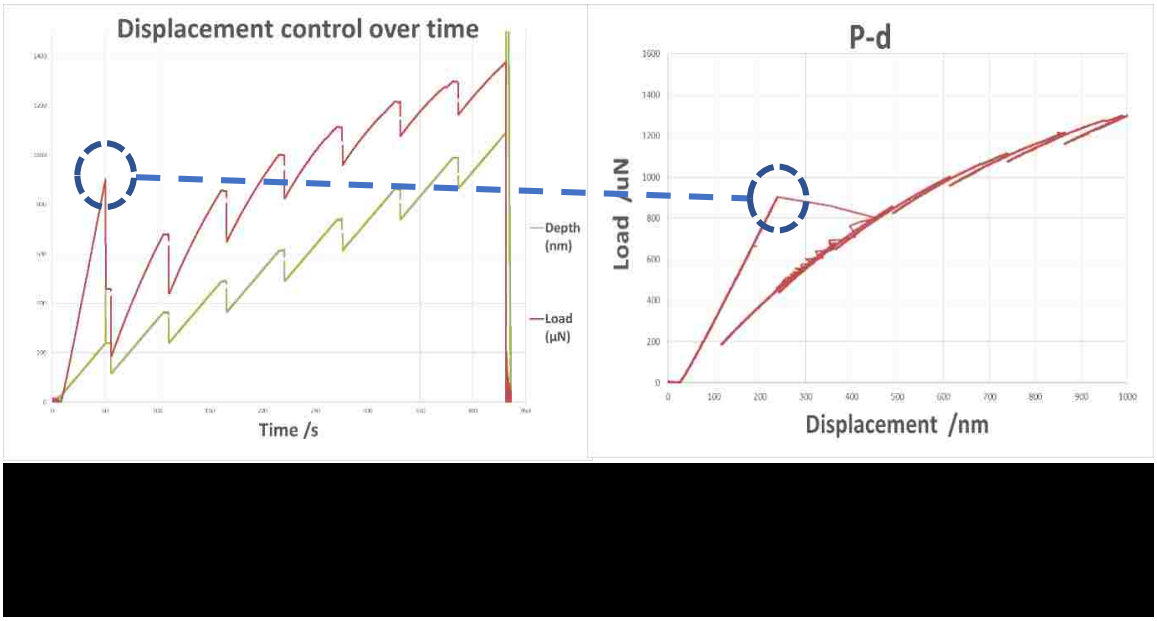

The indentation test result of a clamped-clamped end 3pt bending test is shown in Figure 5-5. The test is under displacement control, with a loading-hold-unloading complex input function, as shown in the green curve in the plot on the left hand side. The red curve is the load response over time during the deflection test. As we can see at

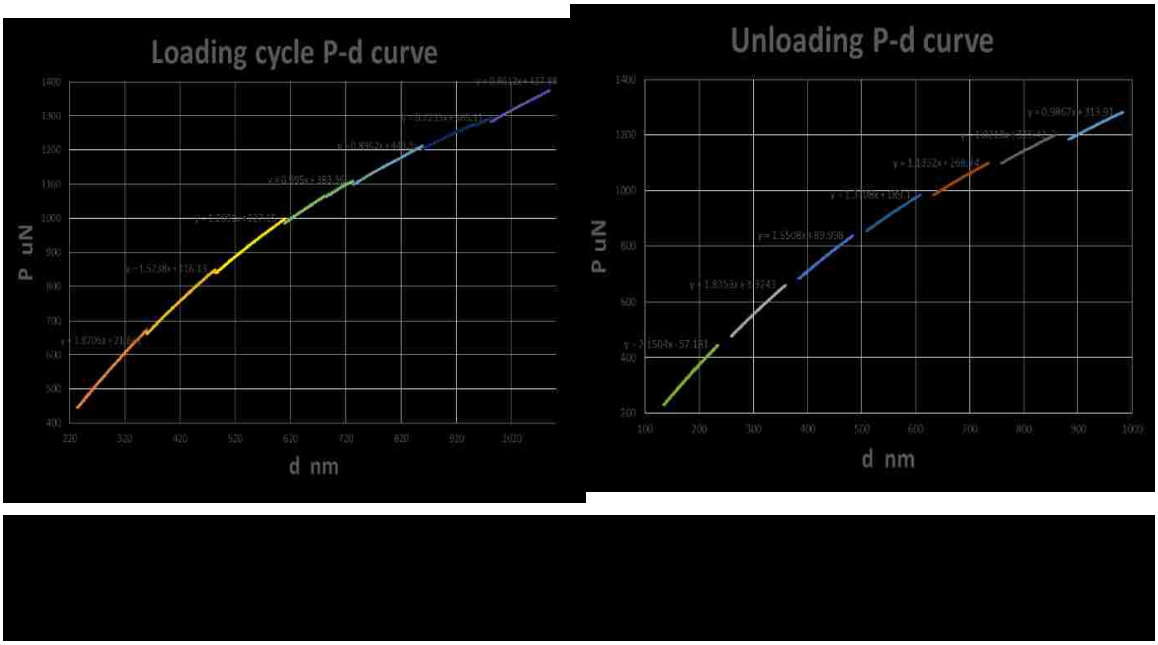

the very end of the first loading cycle, there's a pop-in event, indicating the initiation of a precrack. In each following loading and unloading cycle, the slope decreases slowly. On the load-displacement curve, we could observe the same pop-in event as the slope was linear until the sudden drop at the end of the 1st loading cycle, then the following unloading and loading cycles show a decrease in the slope of P-d, which represents the decreasing stiffness of the specimen.

If we extract the loading and unloading curves separately, as shown in Figure 5-6, we could see the nonlinearity of the stiffness happens to both curves. We obtained the same trend and consistent beam stiffness nonlinearity results in 3 to 4 mechanical tests with the same configuration. This nonlinearity indicates a stable crack propagation after the crack initiation.

We retrieved one of the fractured specimens, and managed to examine the fracture surface using the needle under SEM, as shown in Figure 5-7. The fracture surface shows that a chevron notch was successfully made.

A valid test usually observed for a 3pt free-ends bend specimen with chevron notch is shown in Figure 5-8.[38] The sudden drop in load displacement curve indicates an unstable fracture in (a). In (b) and (c), the turnover in load-displacement curve represents the stability achieved with chevron notch, the maximum load was then used in evaluating toughness.

In a doubly clamped specimen with chevron notch, even though we may achieve a stable crack propagation, the stable extension is not through the maximum load, and thus we could not obtain a Pmax value to calculate the fracture toughness value. 'Work of fracture' is an alternative method in calculating fracture energy, through establishing compliance change and crack propagation length relationship. This method will be introduced in next chapter.

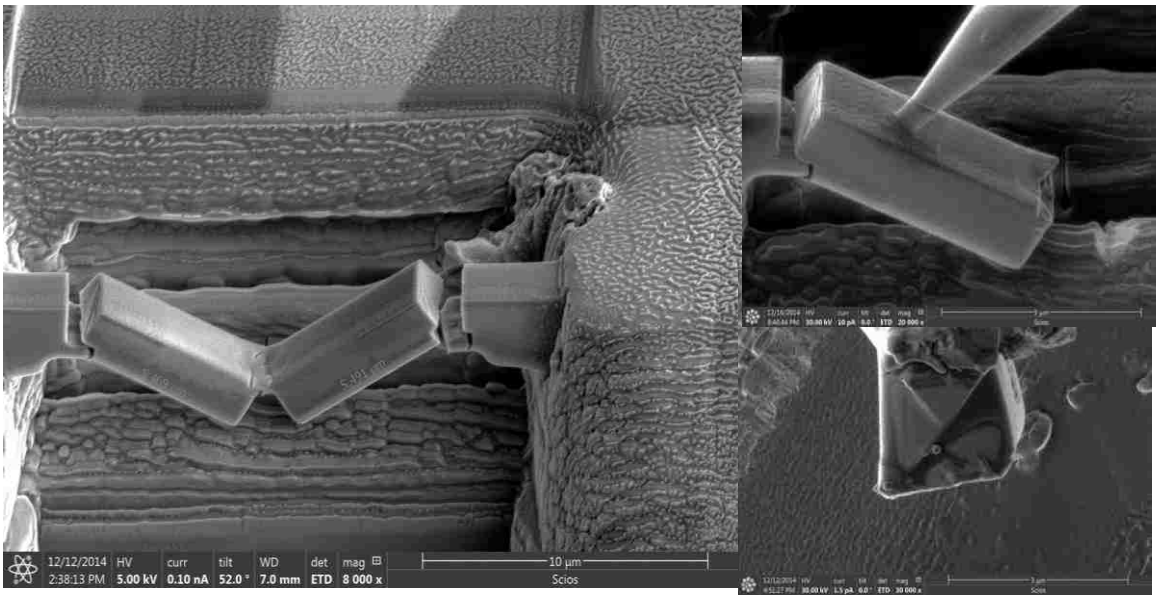

[redacted]

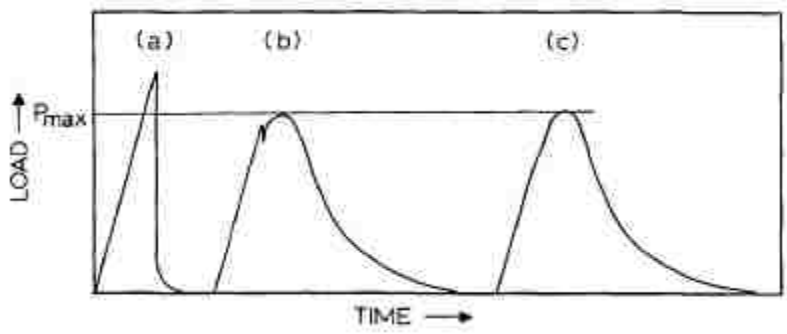

[redacted]

5.3.3 3D Modeling in ANSYS and Frac3D

As shown in Figure 5-9, we build a quarter-symmetric finite element analysis model of chevron notched beam with clamped-clamped ends fixture. The load was applied in a small area on the top surface of the elements located in the center of the beam, shown as the red arrow in the Figure. Boundary conditions are added in the triangle shaped ligament in Z direction, which is along the beam to restrain the movement and model the symmetry of the notch, the notch thickness is idealized as zero. The mesh is refined using Altair Hypermesh to generate homogenous shaped elements. Then after building a series of models with different prenotch length, we obtain the specimen compliance curve as a function of crack propagation length. The

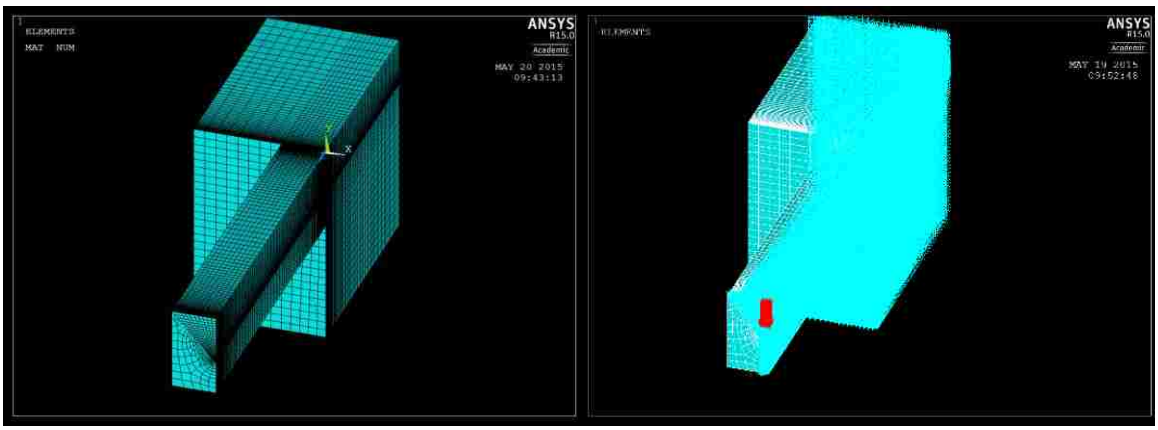

result is shown in Figure 5-10. We must note that when the crack length is in the range of 0-0.6, the curve fitting is acceptable.

Crack length a	Compliance (m/N)
0	0.000195
0.2	0.000201
0.4	0.000209
0.6	0.000225
0.8	0.000228
1	0.000268

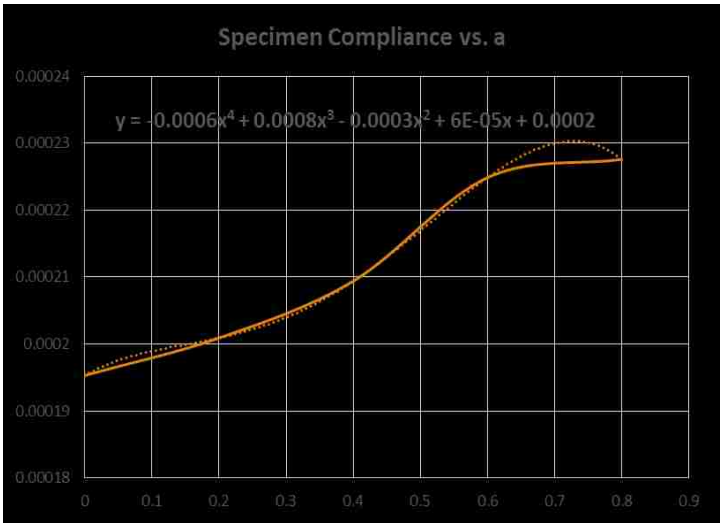

5.3.4 Crack stability analysis of fixed-fixed rectangular chevron specimen

As discussed in section 5.3.2, to achieve the stability of the chevron notched beam it is critical to get a valid maximum load that results in the true fracture toughness value of the tested material. The stability evaluation involves a numerical analysis of the deflected beam compliance, the indenter tip compliance, as well as the precision in fabricating the chevron notched beam in experiments.

In 1977, Bluhm [60] established a numerical method to calculate the stability of a generalized V shaped notch beam bending test, as shown in Figure 5-11. The energy release rate G for a loaded specimen containing a crack is given by

$$G = \frac{1}{2} P^2 \frac{dCt}{dA} \tag{21}$$

where P is the applied load, A is the crack area and Ct is the total compliance of the system, which can be written as

$$Ct = Cs + Cm \tag{22}$$

where Cs is the compliance of the specimen and Cm is the compliance if the testing machine.

The stability of the crack propagation is achieved when energy release rate G is no greater than the energy absorption rate required for crack extension Gcr, i.e.

$$\frac{dG}{dA} \leq \frac{dGcr}{dA} \tag{23}$$

where the critical energy release rate Gcr is a characteristic value of the material, and is independent of the crack propagation area A.

Therefore, the stability could be presumed if $\frac{dG}{dA} \leq 0$

Now we have

$$\frac{dG}{dA} = \frac{1}{2}\left(p^2 \frac{d^2Ct}{dA^2} + 2P \frac{dP}{dA}\frac{dCt}{dA}\right) \leq 0 \tag{24}$$

Depending on the test condition, if the test is under load control where the added load is independent of crack length A, we could eliminate the second term in equation (24) and thus if we assume a constant load Pcr is added on the specimen, equation (24) could be simplified as

$$\left(\frac{dG}{dA}\right)_p = Gcr \left(\frac{d^2Ct}{dA^2} \Big/ \frac{dCt}{dA}\right)_{A=Acr} \tag{25}$$

Where Gcr is the critical energy release rate and Acr is the corresponding critical crack area.

If the test is under displacement control, where the deflection of the beam is defined as $\delta t = P \cdot Ct$, then equation (24) reduces to

$$\left(\frac{dG}{dA}\right)_\delta = Gcr \left\{ [\frac{d^2Ct}{dA^2} - \frac{2}{Ct}\left(\frac{dCt}{dA}\right)^2] \Big/ \frac{dCt}{dA} \right\}_{A=Acr} \tag{26}$$

Therefore, the stability factor could be calculated if system compliance is known as a function of crack area in each test condition. A schematic showing stability tendency is plotted in Figure 5-12. The stability factor is defined as dimensionless, where positive value implies stability. Thus, we could see from the schematic showing that only for certain chevron notched configurations under displacement control, one

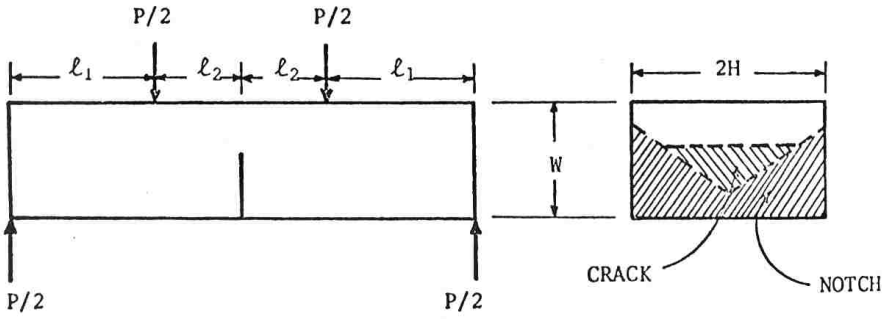

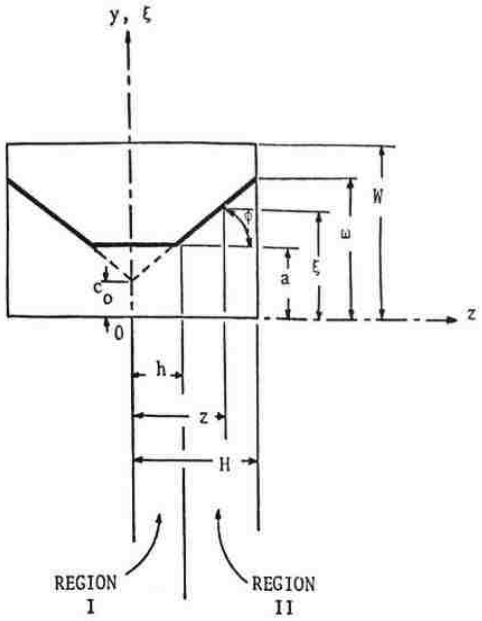

[redacted]

could achieve the stability through a wide range of crack length. This criterion is widely used to evaluate the stability of a 3pt bending test with a generalized chevron notch and also leads to the test requirements for a valid test listed in ASTM standard test.

In our configuration, no analytic formula is available for clamped-clamped specimen geometry. Crack stability analysis is made available with compliance and crack length relationship produced by finite element analysis model.

The stability factor under displacement control Sd, and the stability factor under displacement control Sp were both calculated using MAPLE. The specimen compliance is obtained from our Finite Element Analysis model built in ANSYS Mechanical APDL. In order to calculate the stability factors Sd and Sp, we normalize the specimen compliance as a function of prenotch ratio, where the prenotch ratio is defined as $\alpha = a_0/W$, where α is the in the range of 0.4-0.7. The result is shown in Figure 5-13.

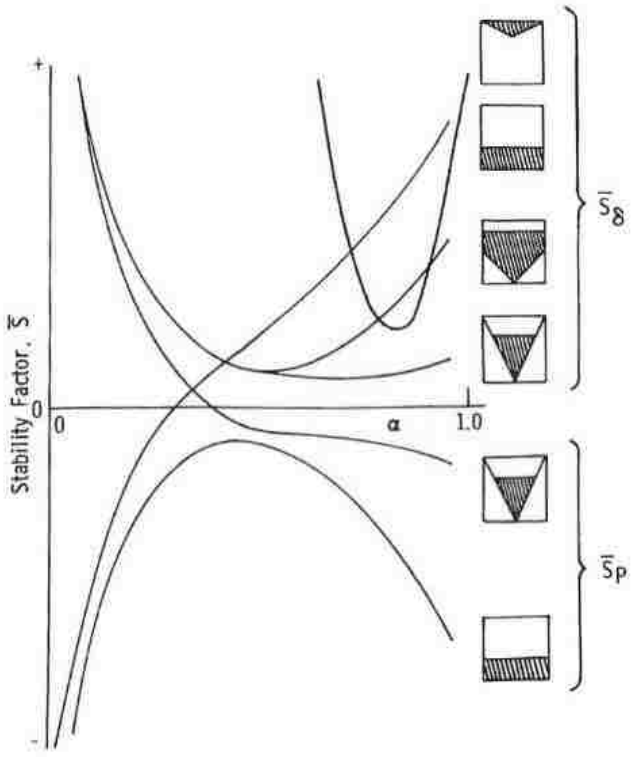

[redacted]

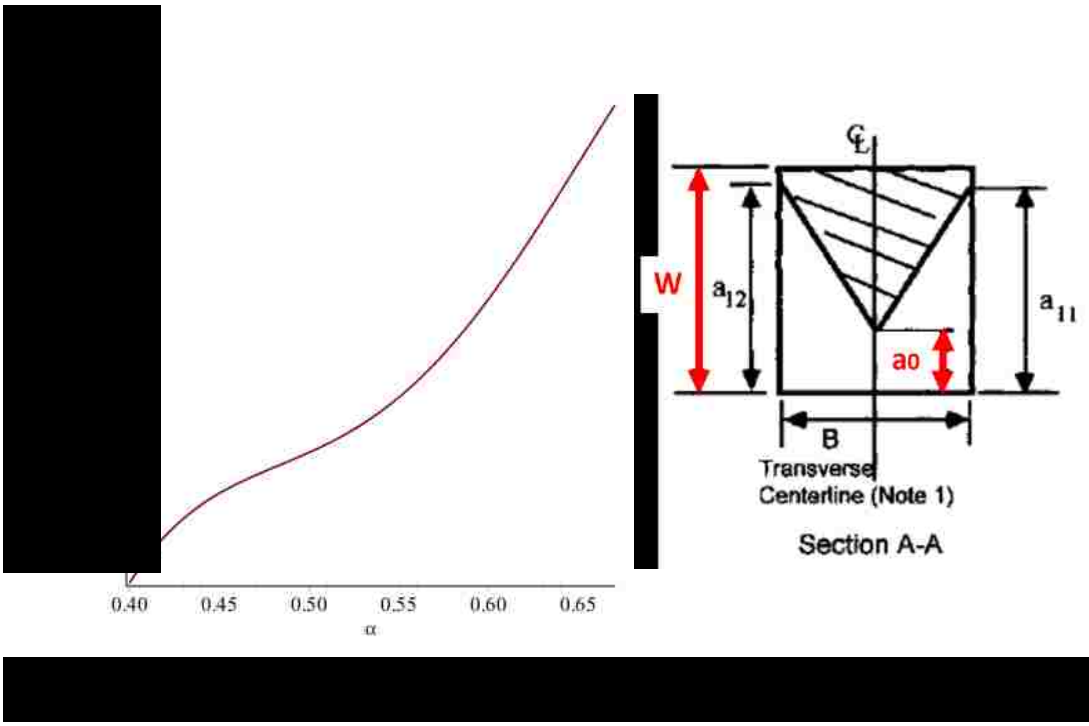

Now, we are plotting the stability factor Sp and Sd as a function of α for the

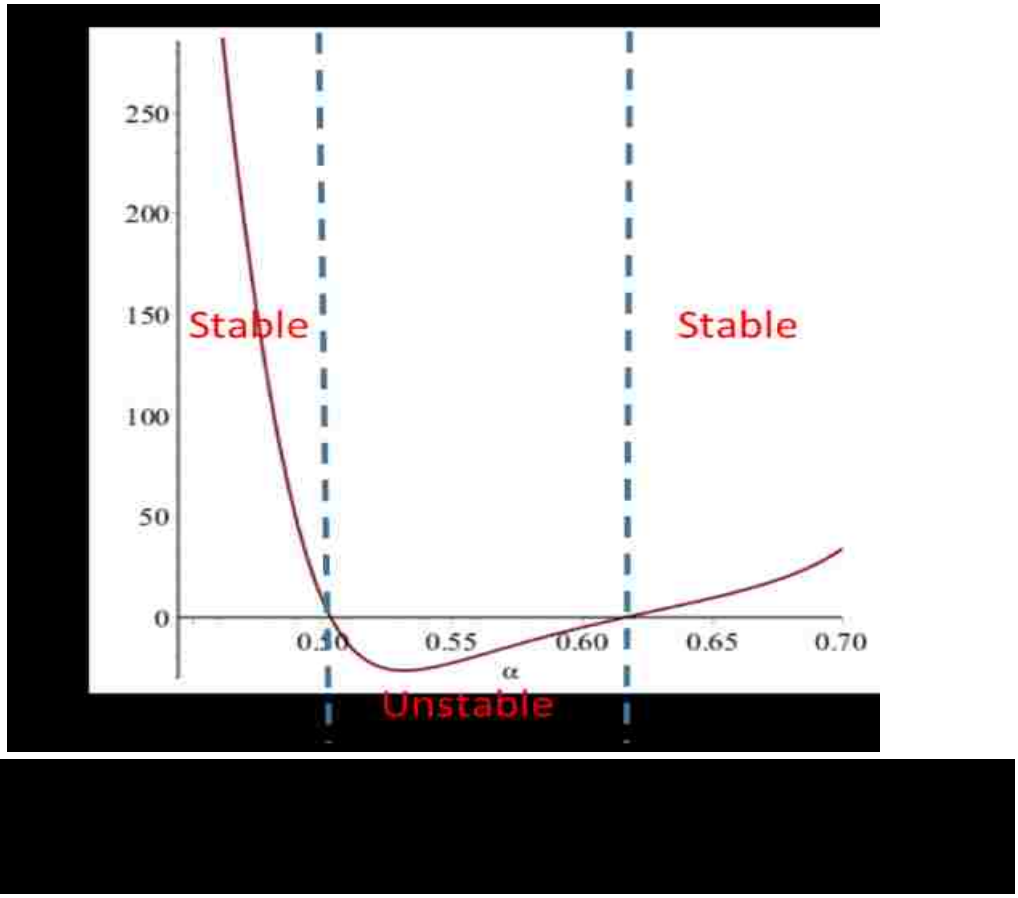

clamped-clamped end chevron notched microbeam. The result is shown in Figure 5-14, Sp and Sd is almost identical in the plot. As defined earlier, Sp and Sd would represent stability when they have positive values. As shown in the plot, the stable region for Sp is when α is in the range of (0.4, 0.5025) and (0.617, 0.7), whereas the stable region for Sd is when α is the range of (0.4, 0.5039) and (0.607,0.7). The machine compliance varies from 0.04-16.2 $\times 10^{-5}$m/N in our analysis, but does not affect the curve's positive range.

Therefore, we could draw a conclusion that the clamped-clamped beam with the current dimension (same as described in section 5.2.1) does not guarantee a stable crack extension under both displacement control and load control, unless the crack length ratio is greater than 0.6.

Another factor we analyzed here is the machine compliance effect, as we noticed, PI85 indenter compliance is 16.2 $\times 10^{-5}$m/N in our experiment, however as we decrease this value to a lower limit 0.04 in our analysis, the curve does not change. Thus, in our experiment the machine compliance could be neglected.

5.4 Discussion and limitation

Therefore, clamped-clamped specimen with a chevron notch could achieve stable crack extension with specific dimension selected in our study. However, the crack stable extension is in a relatively narrow range, which makes it hard to ensure enough amount of fracture toughness measurements. If the notch ratio is kept to be 0.4, the crack will initiate and propagate in a stable manner and then becomes unstable until it reaches

0.5. This could still give us valid toughness value with first stable region with the following criteria:

(1) The chevron notch tip was fabricated sufficiently sharp, in which case, the crack will initiate in lower load, so that the test does not skip this initial stable region instantly and become unstable right after initiation crack.
(2) The test was carried out in a slow loading rate with maximum load-unload cycles, where the crack length propagation from a ratio of 0.4-0.5 (200nm length) will be captured with sufficient data points in the load-unload cycle.

The test is valid with second stable region with following criteria:

(1) The chevron notch tip was fabricated sufficiently sharp, so that the crack initiation load does not exceed the load required to cause beam-roots fracture, in which case, the entire beam is fracture simultaneously both in the middle and the ends.
(2) The crack either stably propagated through stable region I or skips it, but reaches stable region II and propagates in a stable manner. In this case, the load-unload cycle needs to be enough to capture sufficient data before ends-cracking initiates.

Therefore, we can see that this configuration will yield a valid fracture toughness measurement only in a limited range and conditions. The danger of early ends-cracking is also present in the study of clamped-clamped rectangular beam with straight-through cut discussed in section 2.5.

Chapter 6. Design of the micro bowtie chevron test technique

6.1 Bowtie chevron design

To address the shortcomings of previously described testing methods, we have developed a bowtie-shaped beam configuration that is fixed at both ends, and that has a chevron notch milled into the underside at the beam center, as shown in Figure 6-1. The rigid, symmetric test specimen configuration with a centralized chevron notch allows the controlled propagation of a crack advancing along a straight path. This makes it possible to collect multiple measurements of toughness with a single specimen by cyclically loading to a series of increasing peak load values, each of which causes a small, stable, and measurable increase in crack length. The specimen configuration also eliminates mixed mode fracture toughness.

The loading point is above the chevron notch in the middle of the beam. When loading, the tip of the chevron notch will be the highest stress concentration, and thus the preferred site for crack initiation. As the crack advances along the chevron notch, the crack-front length will increase, as shown in Figure 6-1(b), thus a higher load is required for further propagation in each step [61][39]. Under appropriate testing conditions, such as the right chevron geometry and a very stiff loading instrument, the crack would advance in a stable fashion and the extent of crack propagation could be controlled by the

applied maximum load. If a cyclic load-unload function is employed, the compliance change from one cycle to the next is a predictable measure of crack propagation[62]. This correlation enables the measurement of compliance as a function of crack length, the crack advance per load cycle, and the fracture energy associated with the corresponding maximum load value at each step.

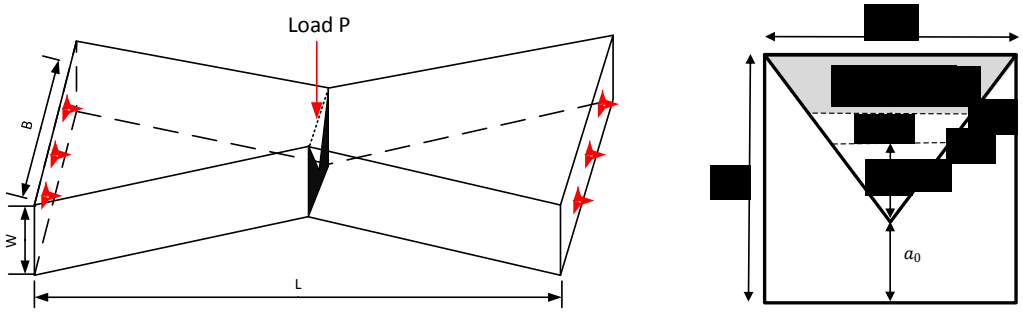

Figure 6-1. (a) Schematic cross-section of the bowtie chevron-notched beam design, showing the chevron notch during crack propagation. The triangle represents the original intact region and the grey area represents the intact region after some degree of crack growth has occurred. (b) Quarter symmetry FEA model. Axial displacement constraints (z-axis) were applied at the intact area ahead of crack front, where different color highlights represent different crack lengths.

A bowtie shaped specimen was selected to avoid the end-cracking observed in rectangular clamped-clamped specimens. Experience with chevron-notched rectangular beams demonstrated that the ends of the beam would simultaneously fracture in a catastrophic fashion so that the real crack propagation at the chevron notch was hard to distinguish. A triangle-shaped specimen has a reduced stress concentration at the beam

ends as compared to a specimen with a uniform cross-section [63]. This eliminates or delays the end-cracking, allowing the central crack to initiate and propagate at the notch area for evaluation of the fracture toughness value.

6.2 Experimental

6.2.1 Specimen fabrication

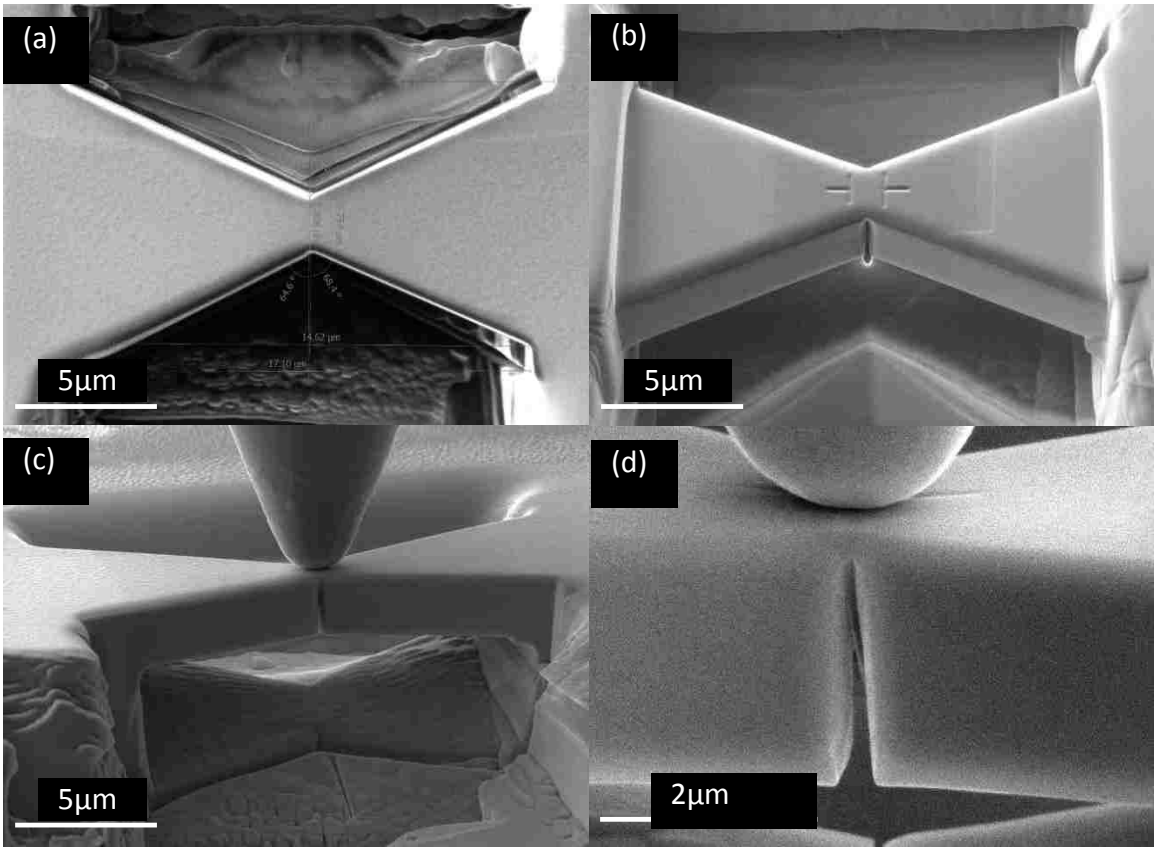

In the examples reported here, each specimen was fabricated from a bulk fused

quartz or lithium-aluminosilicate glass-ceramic (Zerodur^{TM}) sample using Focused Ion Beam (FIB) milling in an FEI Scios instrument. The bulk sample was first mechanically ground and polished on adjacent surfaces so that a 90-degree edge was exposed for FIB milling. After the basic shape was established using a high ion beam current, the test structure was ion polished using 0.1 nA at a tilt angle of $\pm$1.5 degrees to ensure smooth surfaces with minimal ion damage and parallel sides. The chevron notch was fabricated by milling at an angle to the surface in three steps, starting with an ion beam current of 10 pA with a larger width milling pattern, reducing to a smaller width, and finishing with 1.5 pA and a minimum milling width. Thus, a 'V' shaped segment was generated in the center of the test beam with the smallest radius at the tip of the resulting chevron notch, to ensure a reasonably sharp pre-notch for crack initiation. Finally, alignment markers were milled into the top surface to guide placement of the loading tip.

In order to achieve the stability of crack growth, the geometry of the specimen (height, length, width of the beam, notch area thickness, and notch ratio), misalignment tolerance, testing rate, and instrument stiffness all play important roles. [39] The specimen dimensions were selected with these criteria in mind. For the current study, the bowtie specimen in Figure 1 had a nominal length *L* of 14 um, a width *B* of 8 um at the end of the beam and 2 um at the middle of the beam, and a thickness *W* of 2 um, which produces a square cross section of the notch area of 2 um x 2 um. The radius of the sharp notch tip was measured to be 10-20 nm using a Scanning Electron Microscope (SEM), and the widest area of the notch closer to the side surface is 30-50 nm.

6.2.2 In-situ micro mechanical testing procedure

A nanomechanical testing system (Hysitron PI-85) was utilized to carry out the in-situ fracture toughness testing inside the FEI Scios FIB/SEM. The PI-85 instrument was operated under load control, and the load and deflection (tip displacement) were recorded simultaneously throughout each test. Tip alignment was facilitated by the SEM environment. As shown in Figure 6-2 (c), the indenter tip is aligned to the middle of the top surface of the specimen. Operating under load control, the specimen was deflected as the load increased, introduce crack initiation at the tip of the chevron notch. A cyclic load sequence with a loading rate of 150 uN/s was utilized, with 25uN increment in each step. In each load cycle, the specimen was loaded to a certain maximum value to propagate the crack, unloaded, reloaded to a fixed value of 200 μN, and unloaded again to evaluate the beam compliance from the unloading slope. During the next cycle the maximum load value was increased but the compliance evaluation load was kept the same. The detail of this complex loading cycle is introduced in later sections.

6.2.3 Contact stiffness correction to experimental data

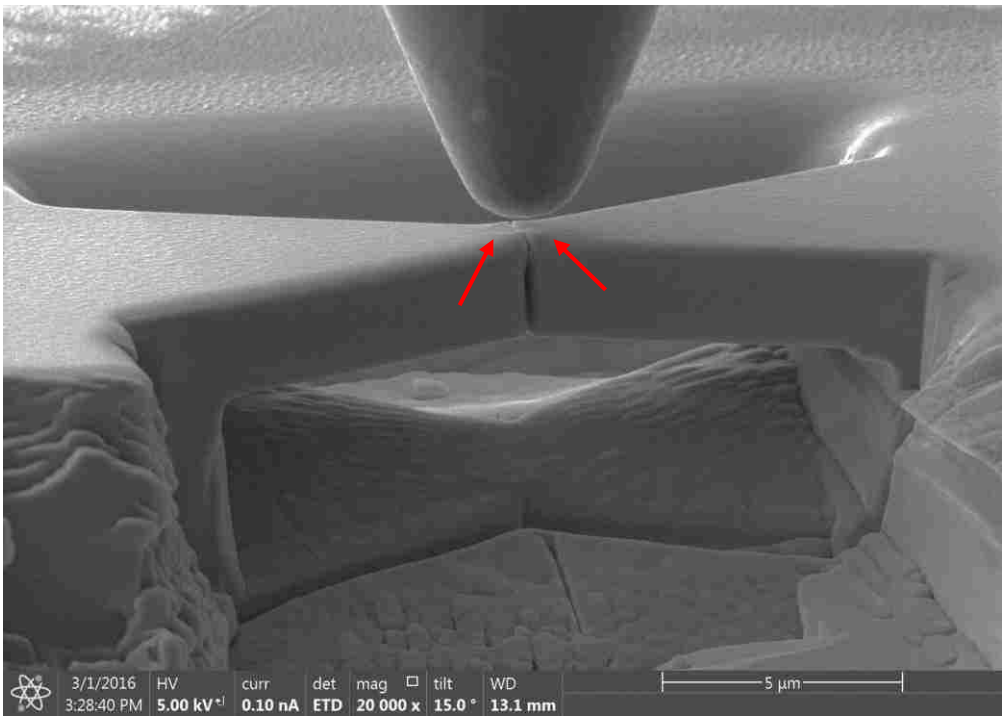

Figure 6-3. Indenter tip impression on the top surface post fracture test was shown.

Prior to analyzing the beam compliance and fracture toughness, it was necessary to correct for the contact stiffness between the indenter tip and the specimen surface, as shown in Figure 6-3. Due to the creation of an indenter impression on the top surface of the specimen, both elastic and plastic deformation needed to be taken into account when analyzing the experiment results. In every loading segment that exceeds the maximum load of any previous cycle, both elastic deformation and new plastic deformation based on the instantaneous load must be known in order to correctly determine the beam displacement[64]. During unloading and during any reloading region that is lower than the prior maximum load, only the elastic deformation and prior plastic deformation need to be subtracted. An example of a corrected data set is shown in Figure 6-3 (a). Thermal

drift of the indenter tip was also calibrated with a separate set of tests, where a drift rate of 2nm/s has been obtained. The mechanical test was conducted separately with a time span around 3-4 minutes each for minimum thermal drift effect.

Once the contact stiffness and thermal drift corrections were applied, a decrease in the slope of one compliance evaluation unload segment to the next indicated a compliance change due to stable crack growth. The compliance data was extracted from each unloading slope and plotted with respect to the maximum applied load.

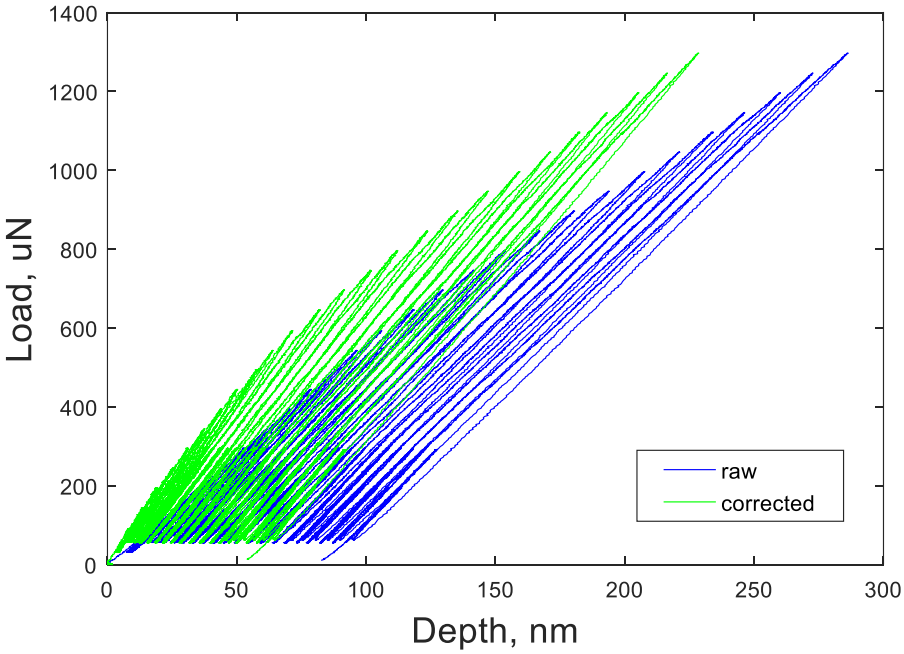

6.3 Complex load cycle for minimizing large deflection effect

6.3.1 Introduction

The geometry and constraints on the clamped-clamped bending beam could cause a nonlinear effect of the compliance change. As the loading increases during mechanical fracture test, the beam deflection increases, which cause a higher restraint from the clamped-clamped boundary condition, as shown in Figure 6-5. This complex boundary condition is mathematically difficult to address with a simple formulation. However, experimentally we could minimize this effect on the compliance change by controlling the load function to extract slope at small deflection. We achieved this goal by inserting a small deflection loading cycle in between each increasing large load cycle for advancing the crack growth. A 200 μN load and unload cycle was inserted in between each loading cycle, where we could measure the compliance change corresponded to the previous maximum load.

6.3.2 Experimental procedure

In order to analyze the nonlinearity of this testing configuration, the mechanical test was carried out using two micro-mechanical testing systems as a comparison to confirm experimental data. One is the Hysitron PI 85 pico-indenter. For this testing method, we applied cyclic loading unloading method in order to measure the unloading slope for calculating the compliance change of the specimen. The fracture toughness results were then computed after post processing the experiment data, including contact stiffness correction and drift correction. In Figure 6-6(a), we observed a difference between the measurement of the stiffness at maximum load cycle and minimum load cycle. The minimum load was chosen at 200 uN to minimize the deflection of the specimen but

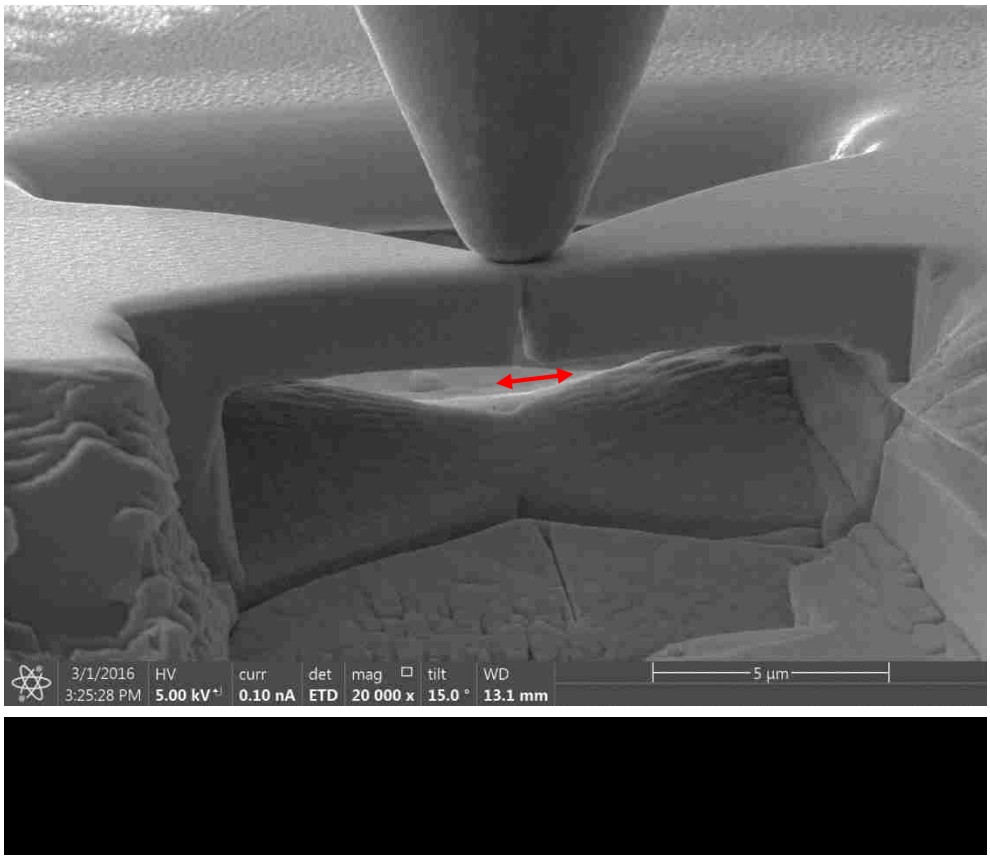

large enough to ensure the accurate measurement of the stiffness without errors. As

the indentation loading increases, the specimen deflection increases. The discrepancy between the two curves is the result of nonlinearity of the clamped-clamped beam boundary condition. The stiffness measured at the large deflection is a combination of the crack propagation contribution and the restraint of the clamping force.

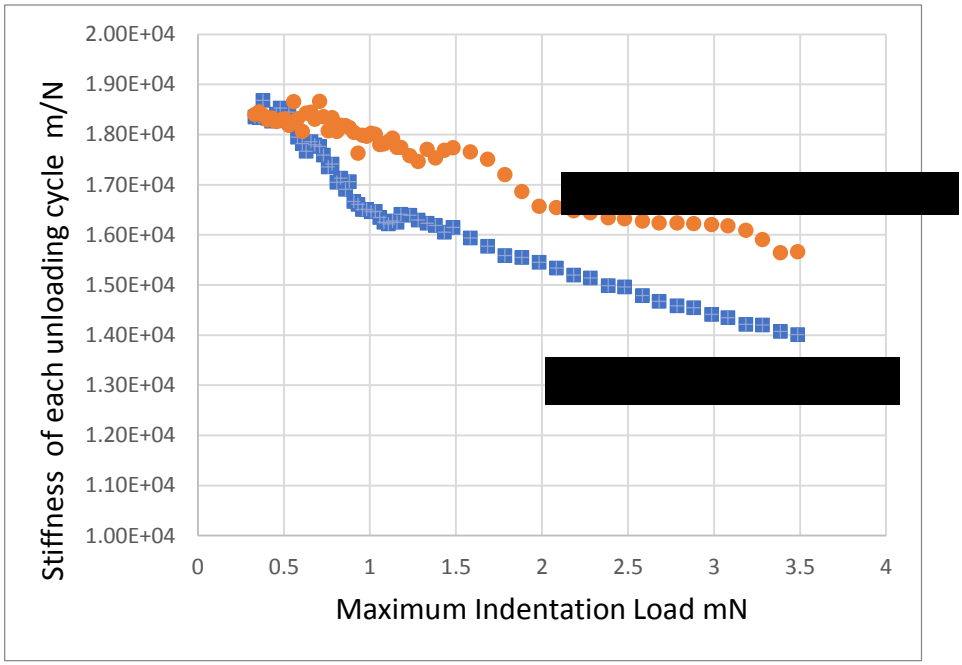
2.00E+04
1.90E+04
1.80E+04
1.70E+04
1.60E+04
1.50E+04
1.40E+04
1.30E+04
1.20E+04
1.10E+04
1.00E+04
Stiffness of each unloading cycle m/N
0
0.5
1
1.5
2
2.5
3
3.5
4
Maximum Indentation Load mN

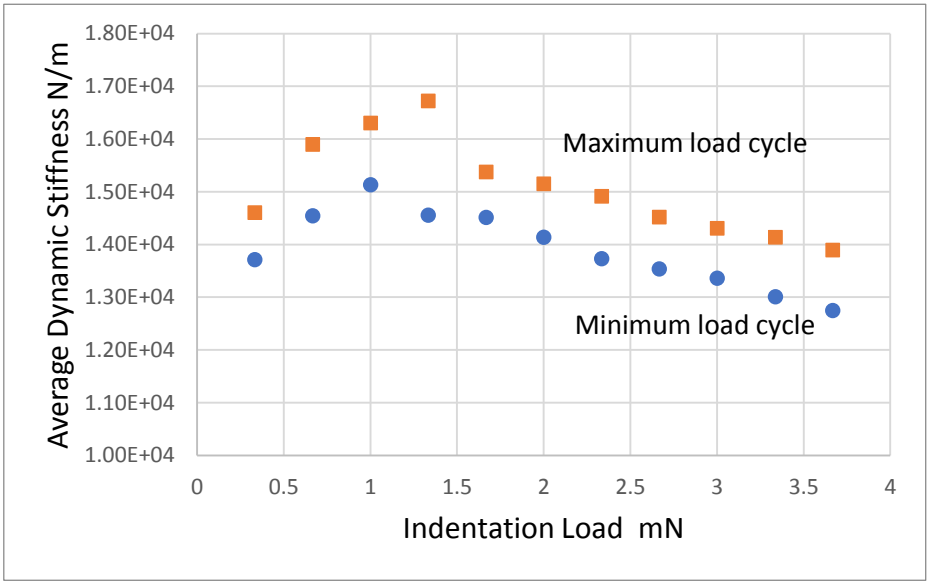
1.80E+04
1.70E+04
1.60E+04
1.50E+04
1.40E+04
1.30E+04
1.20E+04
1.10E+04
1.00E+04
Average Dynamic Stiffness N/m
Maximum load cycle
Minimum load cycle
0
0.5
1
1.5
2
2.5
3
3.5
4
Indentation Load mN

The other method we used is continuous stiffness measurement by Nanomechanics Inc, where a dynamic stiffness was measured at both maximum loading cycle and minimum loading cycle, which is again 200 uN. As a comparison, the nonlinear effect with large deflection could be observed again in Figure 6-6 (b); the same trend was observed at this testing method. The increasing stiffness at the beginning of the test was due to the impression of the indenter on the top surface, which could be corrected with the same contact stiffness correction as shown in Figure 6-6(a). Therefore, we conclude that from two different testing systems, we observed the same nonlinear effect at maximum load measurement. And this proves that the method of complex loading cycle and measurement extracted from 200uN load cycle is reasonable and effective.

6.4 Finite element analysis modeling

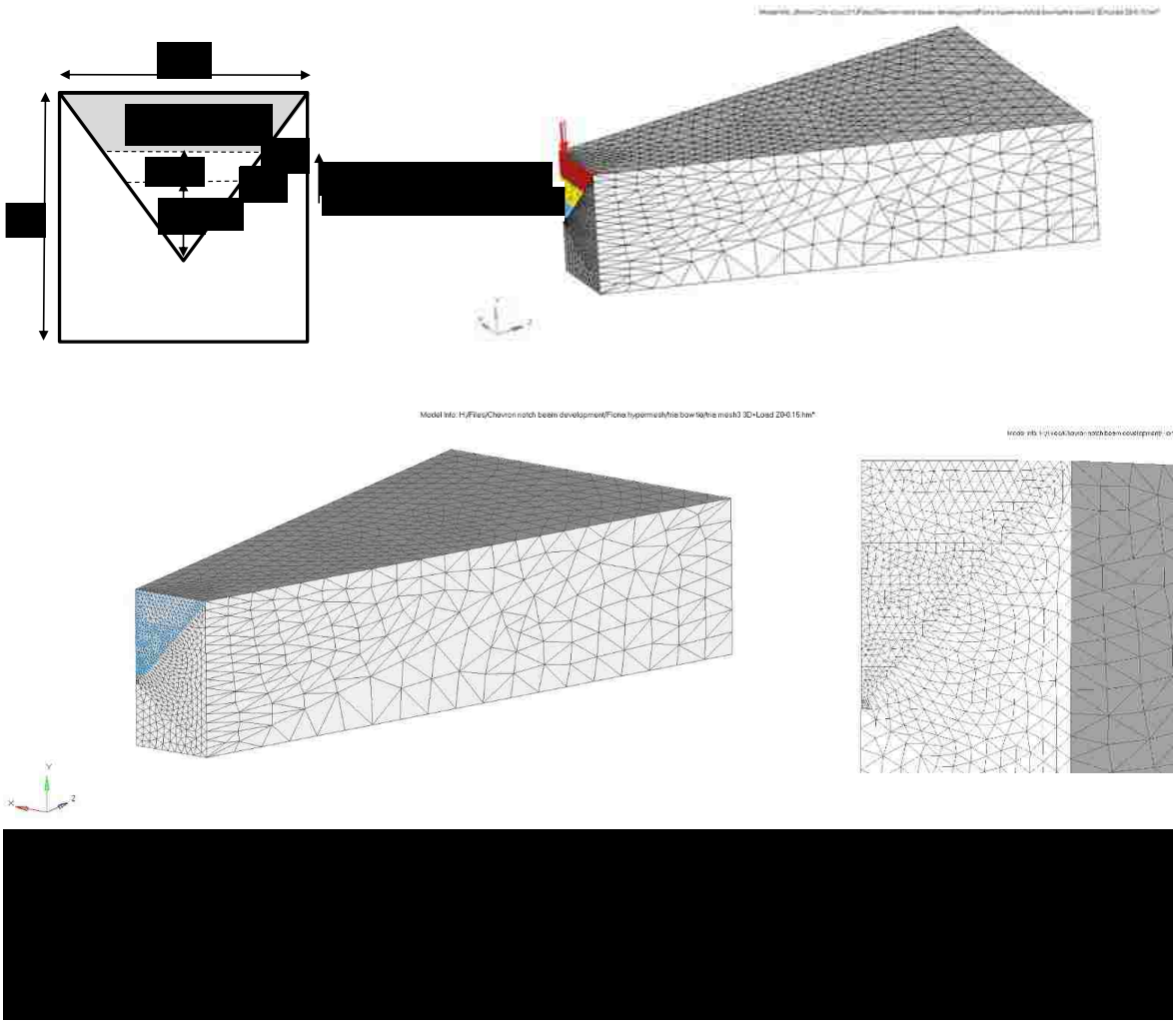

A 3D finite element analysis (FEA) quarter-model was built using Altair Hypermesh and ANSYS Mechanical APDL to evaluate the effects of geometry, and to establish the correlation between specimen compliance and crack propagation. A refined mesh at the notch area was used to ensure accuracy of the FEA model, as shown in Figure 6-7 (d). The model dimensions matched the experiment design. The wide end was constrained in all directions to simulate the attachment to the bulk material, the straight side area in the middle of the beam was constrained in the x (transverse) direction to impose model

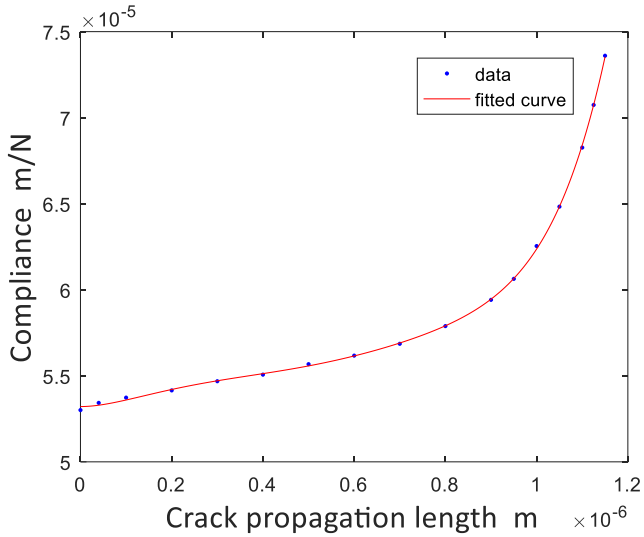

Figure 6-8. Compliance vs. Crack propagation length, generated through FEA, polynomial fit with MATLAB

symmetry, and the intact V-notch area was constrained in the z (axial) direction. A distributed load was added on the top surface of the elements above the notch area. A series of models with different crack opening length a were modeled under the same boundary conditions and load conditions to simulate the crack propagation. The intact area for one such case is depicted in Figure 6-7 (a), and a series of areas are shown by the colored regions in Figure 6-7 (b). By analyzing the deflection at the tip of the notched region for each applied load value, a function describing the beam compliance C as a function of crack length a was obtained, as shown in Figure 6-8.

6.5 Geometry sensitivity evaluation

6.5.1 Method

After a fracture test, the fracture surface could be exposed by milling half of the beam ends and removed horizontally with a manipulator in the SEM. The fracture

surface exposed in this procedure is shown in Figure 6-9. The specimen length and chevron notch shape could be measured, the dimensions of which are depicted in Figure 6-9 (c) and (d).

In order to analyze the effect of geometry dimensions of the beam on the compliance, a series of geometry sensitivity tests were conducted through finite element analysis modeling. Models with different crack length, width, and thickness were created to analyze the beam dimension effect on the overall compliance of the specimen. Moreover, models with different notch angle, overcut/undercut, and different pre-notch length were also created to analyze how the chevron notch geometry would affect the compliance change of the test. The effect of each dimension change on the overall specimen compliance was evaluated with a normalized change factor. A linear change of ±10% was applied at each dimension variable, and then the corresponding change in the compliance could be evaluated using FEA model. By comparing the relative compliance change of the overall beam with same change ratio of each dimension, we could then compare the dimension sensitivity of the bowtie chevron specimen.

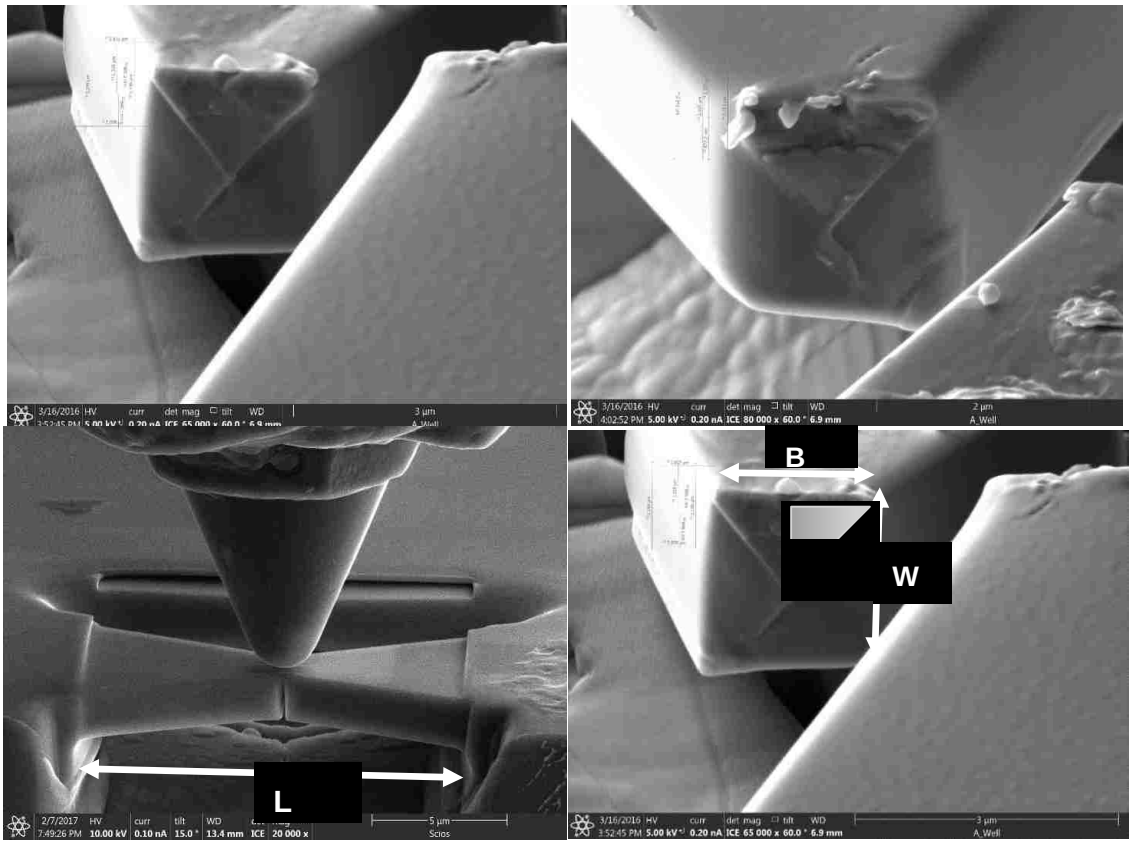

6.5.2 Geometry sensitivity results

Geometry dimension sensitivity can be studied by comparing compliance change ratio at different dimensions. Compliance of the specimen was normalized so that the sensitivity of each dimension change could be represented as comparison. The finite element analysis model with change in different dimensions is shown in Figure 6-10.

The impact factor of each dimension changes is shown in Figure 6-11 and listed in Table 6-1. The length and the height of the specimen play relatively more significant roles compared to other geometry dimensions, and the notch angle effect is minimal on

the relative compliance change as well as overcut and undercut situation. And therefore, we are very confident in machining the chevron notched specimen without concern for the notch angle effect on the overall compliance change of the specimen.

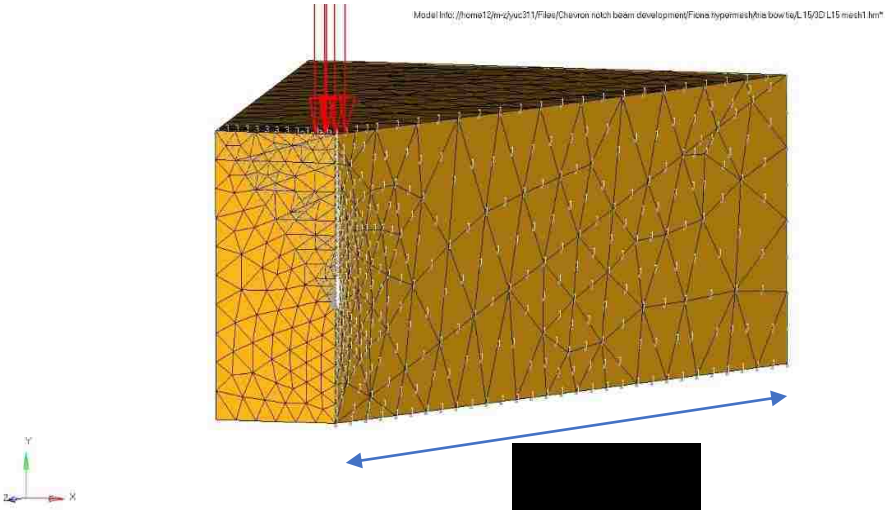
Model Info: //home12/m-z/yuc311/Files/Chevron notch beam development/Fiona hypermesh/tria bow tie/L15/3D L15 mesh1.hm*
[redacted]

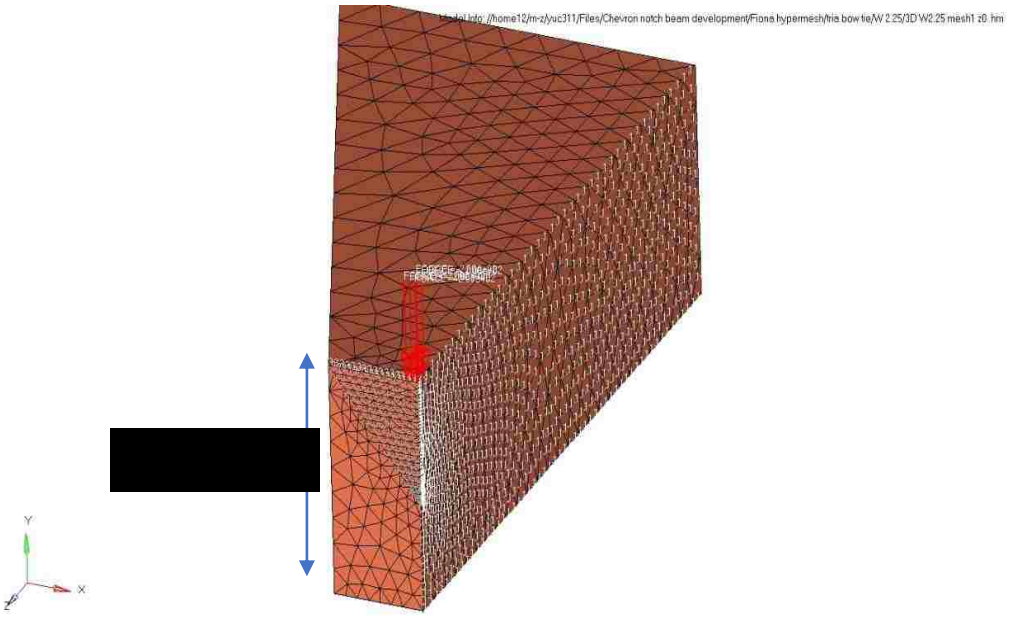
Model Info: //home12/m-z/yuc311/Files/Chevron notch beam development/Fiona hypermesh/tria bow tie/W 2.25/3D W2.25 mesh1 z0.hm
[redacted]

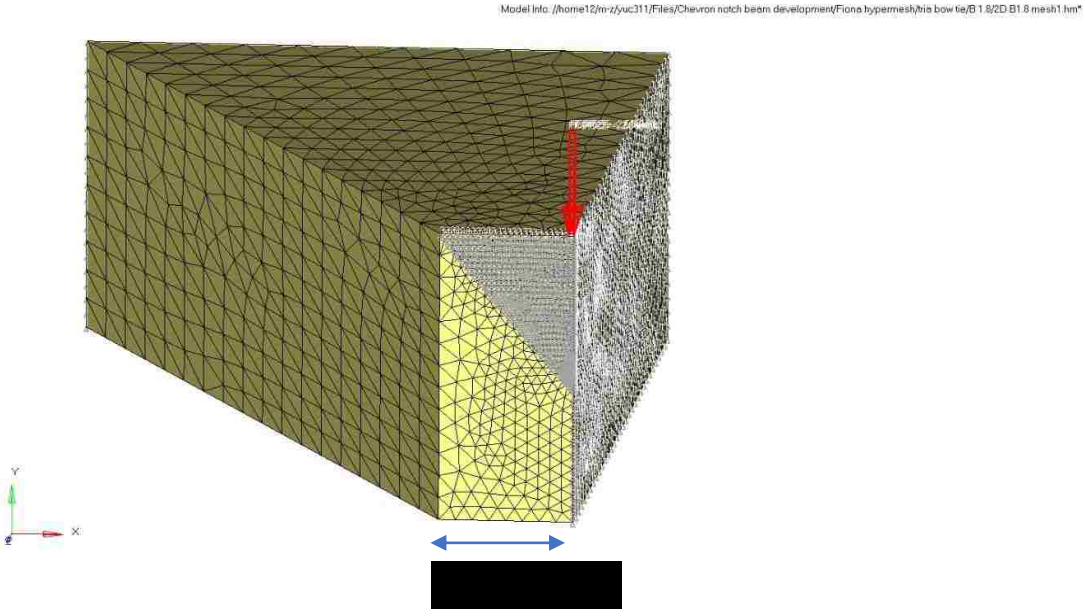
Model Info: //home12/m-z/yuc311/Files/Chevron notch beam development/Fiona hypermesh/tria bow tie/B1.8/2D B1.8 mesh1.hm*
[redacted]

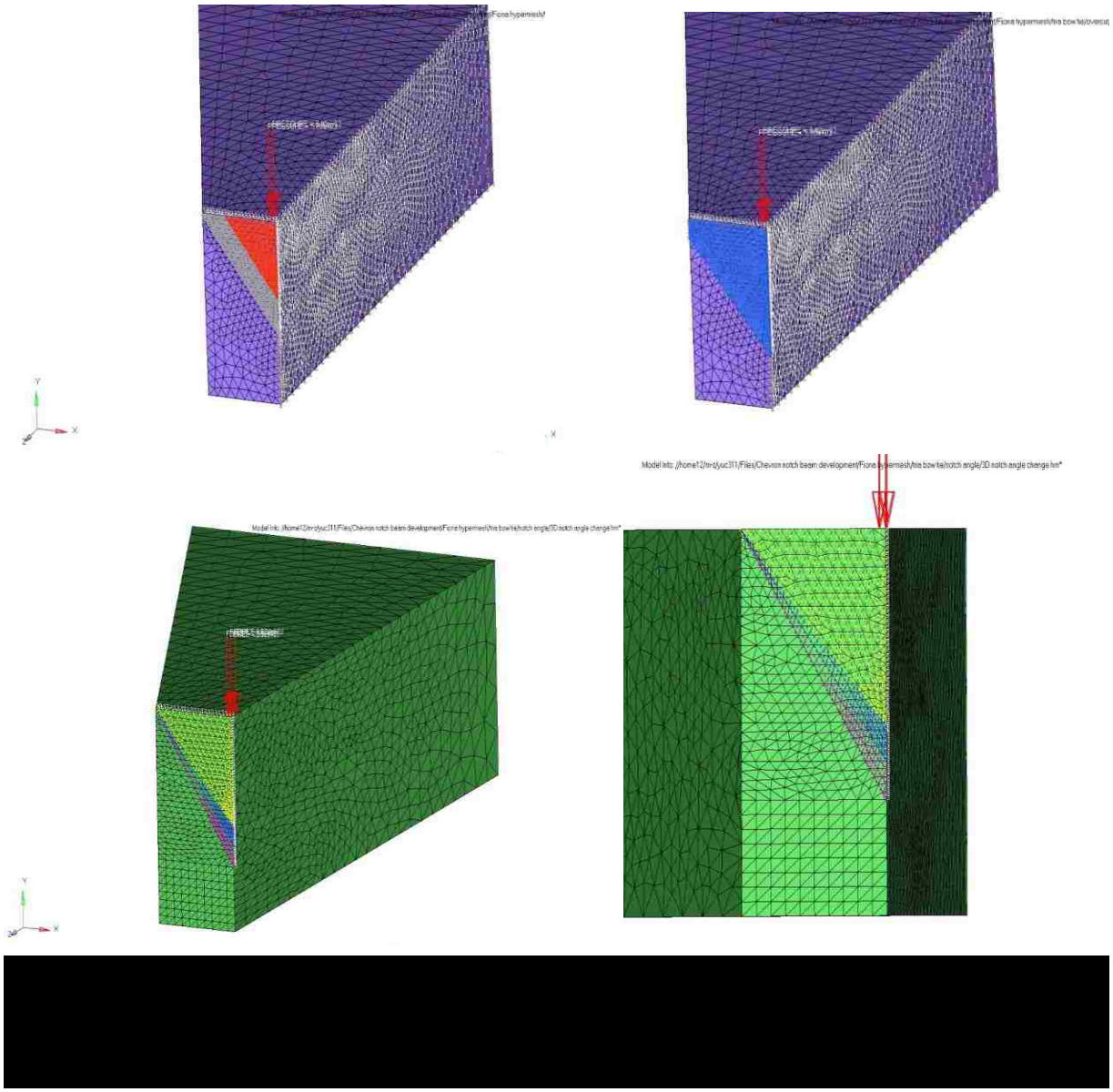

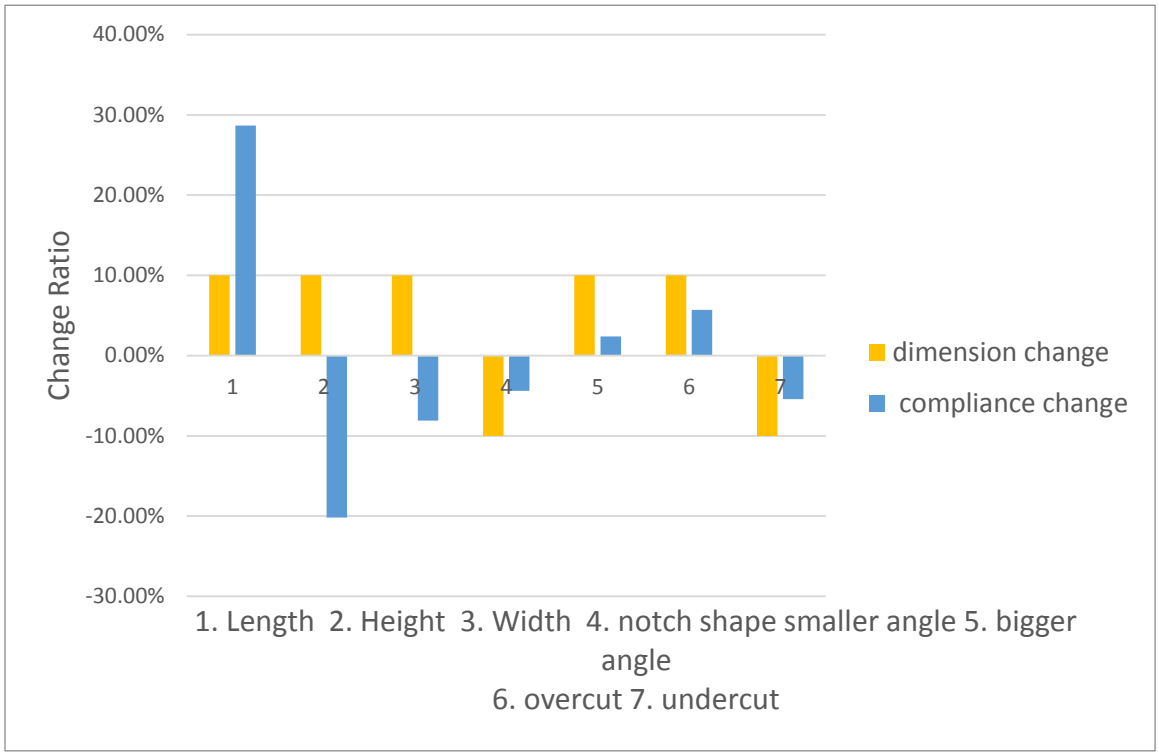
40.00%
30.00%
20.00%
10.00%
0.00%
-10.00%
-20.00%
-30.00%
Change Ratio
1
2
3
4
5
6
7
dimension change
compliance change
1. Length 2. Height 3. Width 4. notch shape smaller angle 5. bigger angle
6. overcut 7. undercut

Table 6-1. Geometry sensitivity results. Normalized impact factor of each dimension change.

Dimension	Standard design	FEA change in model	ΔL/L	ANSYS compliance change	Equation
L	14	15	7.14%	20.476%	22.996%
W	2	2.25	12.50%	-25.238%	-29.767%
B	2	1.8	-10.00%	8.095%	11.111%
alpha	39.8	35.54	-10.70%	-4.695%	n/a
	39.8	45	13.07%	3.099%	n/a
overcut	2	0.333	16.65%	9.480%	n/a
undercut	2	-0.2	-10.00%	-5.423%	n/a

6.6 Crack stability analysis

6.6.1 Methodology

In order to evaluate the crack growth stability, we need to derive the corresponding strain energy release rate with respect to normalized crack propagation length.

Strain energy release rate G for chevron notched specimen could be expressed as,

$$G = \frac{1}{2b} P^2 \frac{dC_t}{da} \tag{27}$$

where P is the applied load, a is the crack propagation length, b is the notch width at the crack front, defined as b= 2 x a x tanφ, where φ is the semi angle of the chevron notch. Note that Eqn. (27) is derived from Eqn. (21) mentioned in section 5.3.4.

$$G = \frac{1}{2a\, tan\varphi} P^2 \frac{dC_t}{da} \tag{28}$$

And C represents the compliance of the bending beam, where $C_t = C_m + C_s$, C_t is the total compliance of the machine compliance C_m and the specimen compliance C_s.

The crack propagation is stable when the propagation rate is smaller than the critical crack propagation rate as the crack length increases, and for brittle materials, there is no R-curve behavior, so that the critical energy release rate is independent of the crack propagation length a and therefore could be expressed as,

$$\frac{dG}{da} \leq \frac{dG_{cr}}{da} = 0 \tag{29}$$

From Eqn. (28) , we get

$$\frac{dG}{da} = \frac{1}{2a\ tan\varphi}\left(P^2\ \frac{d^2C_t}{da^2} + 2\ P\ \frac{dP}{da}\ \frac{dC_t}{da}\right) - \frac{1}{2a^2\ tan\varphi}\ P^2\ \frac{dC_t}{da} \tag{30}$$

Under constant load condition, where $\frac{dP}{da} = 0$

$$\left(\frac{dG}{da}\right)p = \frac{P^2}{2a\ tan\varphi}\left(\frac{d^2C_t}{da^2} - \frac{1}{a}\ \frac{dC_t}{da}\right) = \ G_{cr}(\frac{\frac{d^2C_t}{da^2}}{\frac{dC_t}{da}} - \frac{1}{a}) \leq 0 \tag{31}$$

Under constant displacement condition, where $\frac{dd_t}{da} = 0, where\ d_t = PC_t,$

Thus,

$$P = \frac{d_t}{C_t} \tag{32}$$

$$\frac{dP}{da} = \frac{dd_t}{da}\frac{1}{C_t}\ - \frac{1}{{C_t}^2}\ d_t\ \frac{dC_t}{da} = \ -\frac{1}{{C_t}^2}\ d_t\ \frac{dC_t}{da} \tag{33}$$

Therefore, plugging (33) into (30), we get

$$\left(\frac{dG}{da}\right)d = \frac{1}{2a\ tan\varphi}\ \{P^2\ \frac{d^2C_t}{da^2} - 2P\ \frac{1}{{C_t}^2}\ d_t\ (\frac{dC_t}{da})^2\} - \frac{1}{2a^2\ tan\varphi}\ P^2\ \frac{dC_t}{da} \tag{34}$$

Then plugging (32) into (34) and rearranging, we get

$$\left(\frac{dG}{da}\right)d = \frac{P^2}{2a\ tan\varphi}\ \{\frac{d^2C_t}{da^2} - 2\ \frac{1}{C_t}(\frac{dC_t}{da})^2 - \frac{1}{a}\ \frac{dC_t}{da}\} \tag{35}$$

$$\left(\frac{dG}{da}\right) d = G_{cr}\{\frac{\frac{d^2C_t}{da^2}}{\frac{dC_t}{da}} - \frac{2}{C_t}\frac{dC_t}{da} - \frac{1}{a}\} \leq 0 \quad (36)$$

Now, the compliance of a bending beam is not only affected by the geometry of the specimen but also the material's properties. Thus, compliance can be normalized as $\lambda_t = EB\ C_t$, [65] where E is the elastic modulus of the material and B is the width of the beam. Crack propagation length a can be normalized as $\alpha = a/W$, where W is the beam thickness. Then equation (31) and (36) can be derived dimensionless and simplified as,

$$-f_p = \frac{\frac{d^2\lambda_t}{d\alpha^2}}{\frac{d\lambda_t}{d\alpha}} - \frac{1}{\alpha - a_0/W} \leq 0 \quad (37)$$

$$-f_d = \frac{\frac{d^2\lambda_t}{d\alpha^2}}{\frac{d\lambda_t}{d\alpha}} - \frac{2}{\lambda_t}\frac{d\lambda_t}{d\alpha}\frac{1}{\alpha - a_0/W} - \frac{1}{\alpha - a_0/W} \leq 0 \quad (38)$$

where a_0 is initial crack length/ pre notch length, f_p and f_d are defined as the crack stability factor under constant load and constant displacement conditions respectively. Positive values indicate stable crack growth, and negative values indicate instability.

Thus, it is now critical to obtain the value for the compliance function λ_t with respect to crack length ratio α, so that the first derivative and second derivative of compliance change will lead to the determination of stability of the crack growth. The machine compliance is a parameter regarding the equipment, which in our case, is the machine compliance of Hysitron PI85 Pico-indenter. The unit includes the transducer,

the spring and all the loading cells behind the indenter tip. We may notice that under load control, the total compliance λ_t in the expression can be replaced as λ_s of the specimen, because only the derivative terms are included. However, for the displacement control, machine compliance may play a more significant role. This machine compliance is usually large compared to specimen compliance during bending tests to ensure the stability of the test. For Hysitron PI85, a non-normalized value of 1.5 nm/mN was initially provided by the company, then recalibrated to be 6.26 nm/mN after several years of usage. The machine compliance was calibrated using a cube corner tip on the surface of fused quartz. In our analysis, the machine compliance was set to be between 0.1 to 50 nm/mN as to sufficiently analyze the problem, with any calibration error of the machine compliance taken into account.

6.6.2 Crack stability results

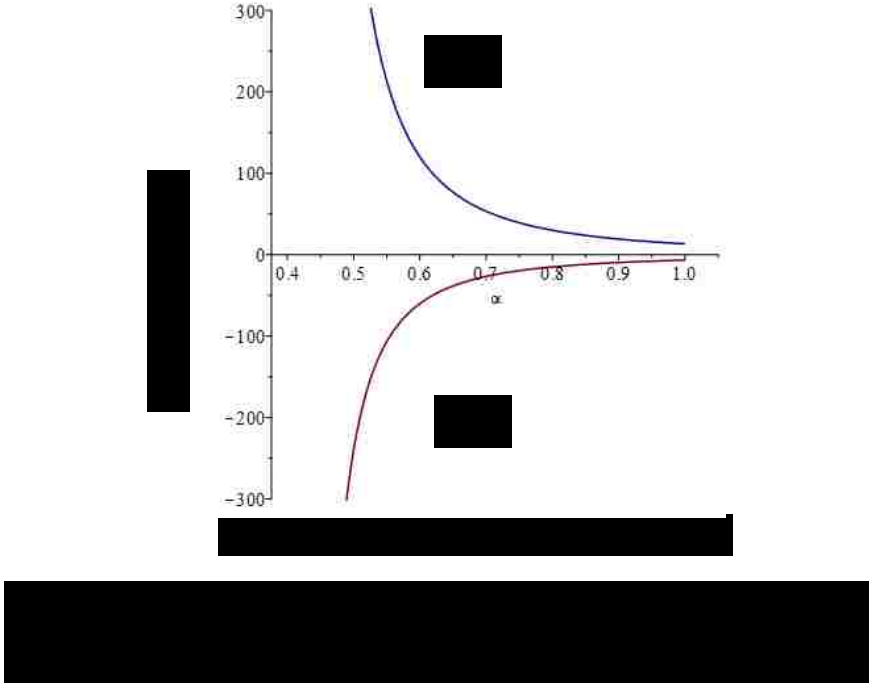

Mathematical software MAPLE was used to do the analysis crack stability factor evaluation for the derived normalized compliance function (37) and (38). Machine compliance was selected within the range of 0.1-50 × 10^{-3}m/N, which yields to a normalized machine compliance λ_m of 34.2 to 17100, with a beam width of 2 μm. Within this range of machine compliance change, which includes the current calibrated machine compliance of PI85 system to be 2140.92, there is no significant impact on the defined stability factor. The stability factor has been plotted with respect to crack propagation length ratio α, which is shown in Figure 6-12. As we can see that under constant load condition, in no range of pre notch ratio would result in a stable crack propagate. Under constant displacement control, in all the pre-notch ratio this configuration will result in a stable crack growth as the crack propagates.

6.6.3 Stability verification by TEM

In order to verify the compliance prediction of FEA model and the stability analysis, we intentionally conducted an incomplete fracture test, where the load function was stopped after a few loading cycles, so that the crack has initiated but did not completely fracture the beam. The initiation of the crack can be observed in the slope change of unloading segments in the load- displacement curve, which represents the stiffness of the specimen. Then a TEM specimen of size 2 x 2 um was lifted out at the notch area with a thickness of 200nm, so that the crack front is embedded in the TEM specimen, as shown in Figure 6-13.

The bright field image of one TEM specimen extracted from an interrupted test is shown in Figure 6-13. The image is oriented such that the original top of the specimen is located on the left side. The impression left by the indenter tip is visible on that edge of the specimen. A clear vertical line is visible spanning the triangular region. In the original chevron orientation, this line runs from side to side. Convergent beam electron diffraction (CBED) patterns taken on both sides of this line are well ordered, as expected for a single crystal. However, a subtle shift in the patterns indicates a small change in crystal orientation on the order of 2-3 degrees, consistent with an intact crystal on one side and a slightly misaligned crystal on the other side where the crack has opened and imperfectly closed. The CBED pattern acquired right on the line is much less ordered, consistent with high local elastic strain gradients present at a crack tip. The likelihood that the line indicates a stable crack front is therefore very high, and its presence verifies that crack stability is indeed possible with the chevron notch bowtie specimen.

This image also makes it possible to measure the crack propagation length. The total distance from the tip of the triangle to the top of the beam is 1.26 μm. The beam was nominally 2 μm thick, so the initial crack length a_0 was approximately 0.74 μm and the crack length ratio was $a_0/W=0.37$. This is very close to the target FIB length of $a_0/W=0.40$, demonstrating the ability of the blind milling procedure to accurately achieve the desired notch geometry. The cracked region is 0.76 μm in length, corresponding to total crack propagation of approximately 60% of the triangular region. These results can be directly compared to the FEA model that predicted a cracked region 0.80 um long, based on the corresponding measured compliance of this particular beam at the end of the test. The FEA results and TEM measurement of experiment crack propagation were consistent and therefore the validity of the FEA model was confirmed.

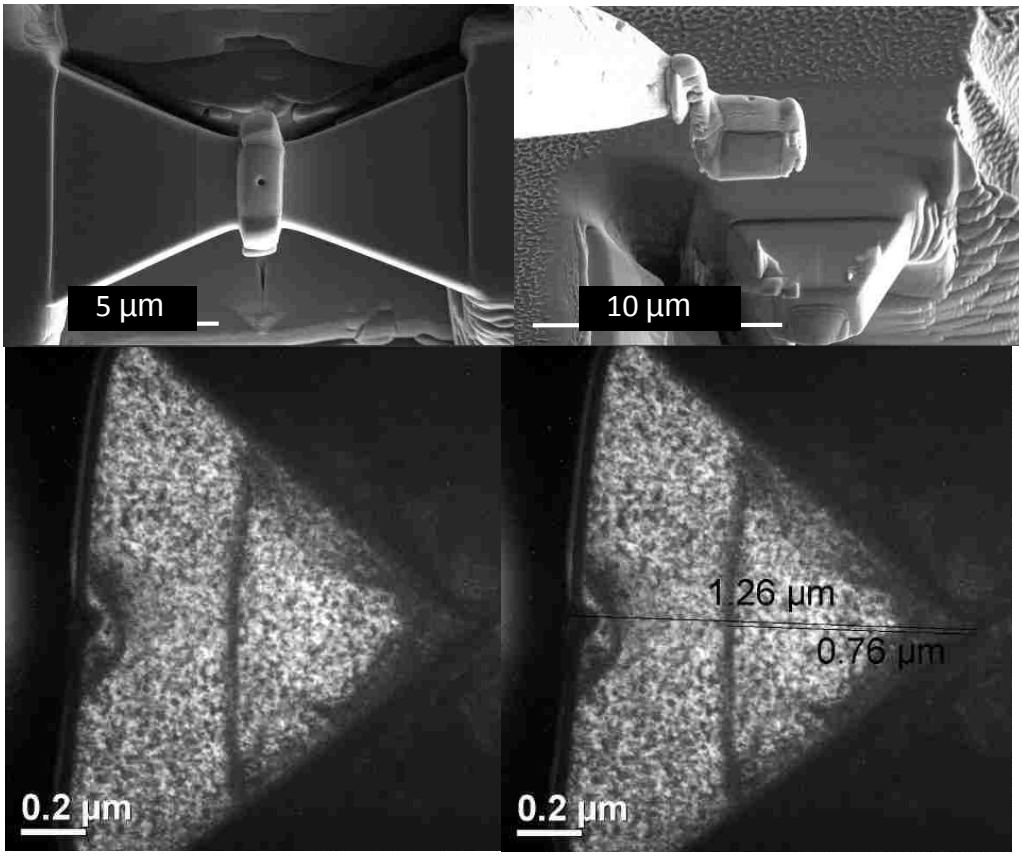

6.7 Fracture energy calculation

Fracture toughness then was evaluated using an energy balance approach based on the measured compliance change and corresponding load data, combining the results from the experiment and FEA model. The strain energy release rate *G* was obtained as a function of compliance change as the crack propagates, which is derived for the chevron notch in our configuration as shown in Equation (27), rewritten here for convenience,

$$G = \frac{1}{2b} P^2 \frac{dC}{da} \tag{27}$$

The quantity $\frac{dC}{da}$ is the compliance change as the crack propagates during each loading cycle. The crack propagation length a and rate $\frac{dC}{da}$ are obtained by combining experiment output, FEA modeling, and numerical methods using MATLAB. If the material is brittle and isotropic, the stress intensity factor at fracture, K_I , can also be obtained by the relation,

$$K_I = \sqrt{\frac{EG}{1 - \nu^2}} \tag{39}$$

where E is the elastic modulus and ν is the Poisson's ratio. A fracture toughness value could then be calculated based on Equation 27 for each unloading segment, and multiple results from a single specimen could be averaged to create a final value and a statistical distribution, as shown in Figure 6-14. The compliance change as a function of crack length is plotted for two transparent ceramic materials fused quartz and Zerodur™, as shown in Figure 6-15.

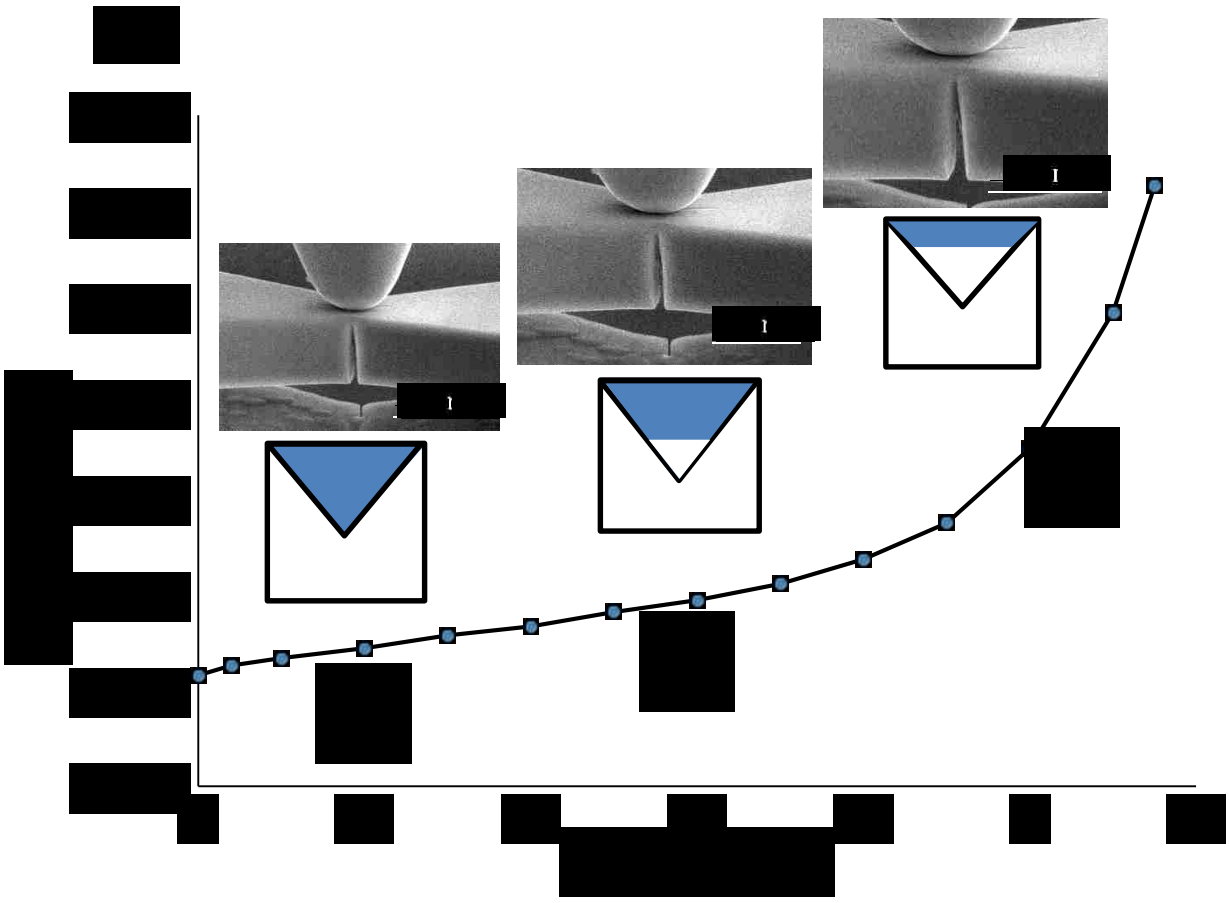

Figure 6-14. Finite element analysis result of compliance change with respect to crack length

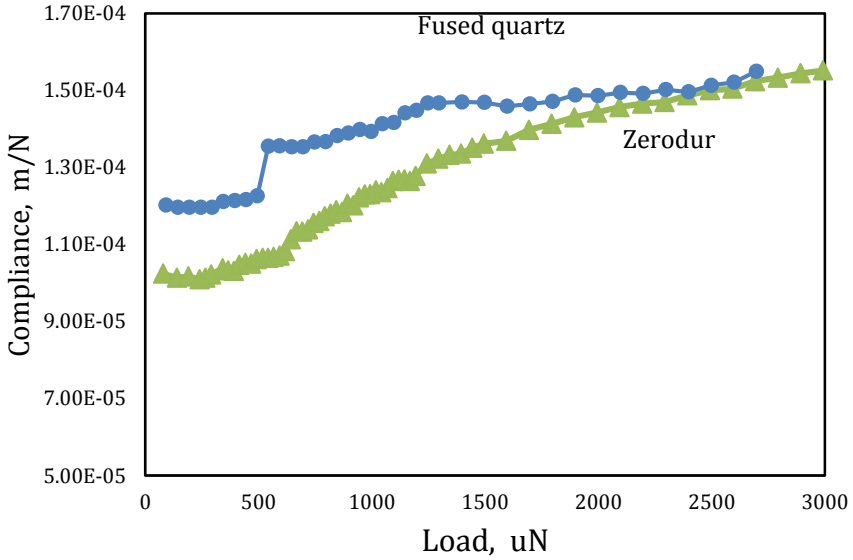

Figure 6-15. Compliance change in each unloading segment with respect to load for fused quartz and Zerodur™.

A comparison between the fracture toughness values measured in this study and literature results is shown in Table 6-2 and Table 6-3. Actual specimen dimensions measured in the SEM were used for all calculations rather than the nominal dimensions described above. The fused quartz results represent 27 data points extracted from 3 bowtie specimens. An average fracture toughness value of 0.62 ± 0.07 MPa/$\sqrt{m}$ was obtained for the fused quartz, which matches very well with those results that have been reported in literature. [24][66–68]. There are many measurements of fused quartz fracture toughness so the reported values are likely to be reliable. Unfortunately, there are very few fracture toughness measurements reported for Zerodur™. The glass-ceramic results from the bowtie structure represent 28 data points extracted from 4 specimens. The average value of 1.26 ± 0.1 MPa/$\sqrt{m}$ for the glass-ceramic matches well with a 2004 report that used microindentation [69]. An older report that also used microindentation claimed a value between that of fused quartz and the newer Zerodur™ result. [70] While

the match to the current measurement is not very close, both values agree insofar as the glass-ceramic has a higher fracture toughness than fused quartz.

Table 6-2. Fused quartz fracture toughness value comparison with literature

Testing Method	**Fracture toughness value MPa/$\sqrt{m}$**	**References**
Macroscopic three-point bending	0.58	Harding et al. [66]
Macroscopic chevron-notched short rod	0.735	Barker [67]
Nano indentation toughness, cube corner tip	0.6±0.1	Scholz et al. [68]
Micro cantilever beam chevron	0.65±0.04	Mueller et al. [48]
Microscopic bowtie chevron	0.62±0.07	this study

Table 6-3. Zerodur™ fracture toughness value comparison with literature

Testing Method	Fracture toughness value $MPa/\sqrt{m}$	References
Micro indentation toughness, Vickers	0.9	Viens [70]
Micro indentation toughness, Vickers	1.33±0.08	Bouvier et al. [69]
Microscopic bowtie chevron	1.26 ± 0.1	this study

6.8 Conclusion

In aggregate, the current results strongly support the chevron-notch bowtie as a promising test structure for micro-scale fracture toughness testing of brittle materials.

Full analysis of this testing method has been carried out to ensure the validity of the testing theoretically and experimentally. Analytical analysis includes finite element analysis, geometry sensitivity analysis and crack stability analysis. It has shown that this testing method will ensure crack stability and therefore provide accurate fracture measurement as well as a time and cost-efficient testing method by generating multiple results out of one single test.

Chapter 7. Conclusion and Future Work

The first part of this work has focused on micro scale fracture toughness analysis on transparent ceramic magnesium aluminate spinel. Fracture behavior of low index plane single crystals were investigated. Correlation between fracture energy and low index plane energy was established through micro cantilever deflection testing method. Fracture toughness measurements of single crystal magnesium aluminate spinel specimens indicate that among low index planes, the {111} single crystal plane is the highest surface energy orientation, and the {100} plane is the lowest, with the {110} orientation in the middle. These results are in agreement with most recent experimental and theoretical studies. Fracture test results for undoped bicrystal boundaries have shown that the {111}/{100} boundary orientation has a 43% lower fracture toughness than the {110}/{100} boundary orientation, implying that the {111}/{100} boundary has the greater energy of the two. Somewhat surprisingly, Eu-doped grain boundaries exhibit the same level fracture energy as their undoped counterparts regardless of whether or not Eu is present.

High resolution STEM micrographs suggest a mechanism underlying the fracture toughness results. For {111}/{100} doped grain boundaries, Eu was found to strongly segregate to the {111} plane and faceted Eu-rich precipitates were observed. However for the {110}/{100} grain boundary, only a 'clean' interface was found between small, sparsely distributed Eu-rich precipitates. Neither case showed the same highly-ordered grain boundary complexion previously observed in a {111}/{100} Yb-doped spinel boundary. Although a strong bond may exist between Eu and the {111} side of a boundary, relatively poor strength of Eu-Eu bonds or bonds between Eu and the {100} boundary plane may result in the unimproved fracture toughness associated with Eu doping.

These results support the theoretical prediction that the surface energy of a {111} plane is more strongly affected by doping than the other low index planes. However, the larger Eu 2+ ion has a reduced tendency to segregate and alter surface energy than the smaller Yb 3+ ion. Valence may play a more significant role than size, so the present result does not necessarily contradict the general size trend observed in other material systems.

Eu doping did not have a positive effect on boundary strength in either of the two orientations examined, which can be attributed in part to the formation of a more "disordered" high temperature grain boundary complexion. However, when extrinsic mechanisms are considered in fracture behavior of bulk materials, weaker grain boundaries can enhance energy dispersing mechanisms like bridging, crack deflection, and pull-outs of grains. This was observed in Satet et al.'s work in the polycrystalline

Si_3N_4 system, in which an increase in rare earth dopant size introduced weaker boundaries and thus an increasing fracture toughness.[29] It may be, therefore, that Eu is an attractive dopant to choose because Eu-doped grain boundaries may have unchanged bond strength between the grain boundaries while offering options for controlling grain growth by selection of processing temperature.

The second part of this work was focused on micro scale fracture toughness testing method development. This experimental testing method was further investigated with detailed experimental procedures targeting various goals. This include large deflection of beam bending induced nonlinearity, contact stiffness evaluation induced compliance correction methods and also factors that contribute to stable crack growth analysis.

Testing method was first utilized to measure fracture toughness on two brittle transparent ceramics, fused quartz and Zerodur™. An average fracture toughness value of 0.62 ± 0.07 MPa$\sqrt{m}$ was obtained for the fused quartz, which matches very well with those results that have been reported in the literature. [66, 67,68] There are many published measurements of fused quartz fracture toughness so the reported values are likely to be reliable. Unfortunately, there are very few fracture toughness measurements reported for Zerodur™. The glass-ceramic results from the bowtie structure represent 28 data points extracted from 4 specimens. The average value of 1.26 ± 0.1 MPa$\sqrt{m}$ for the glass-ceramic matches well with a 2004 report that used microindentation . An older report that also used microindentation claimed a value

between that of fused quartz and the newer Zerodur^{TM} result. [69] While the match between the older value and the current measurement is not very close, both values agree insofar as the glass-ceramic has a higher fracture toughness than fused quartz. In aggregate, the current results strongly support the chevron-notch bowtie as a promising test structure for micro-scale fracture toughness testing of brittle materials.

The bowtie chevron-notched micro beam has been further analyzed and then demonstrated using two different experimental instruments and a brittle crystalline ceramic material. Although the instruments are both inherently load-controlled, their finite response time enabled stable crack growth as shown by cross-section TEM from an interrupted test. None of the tests failed prematurely at the ends, showing that the bowtie design is successful at delaying the early end-cracking sometimes observed in rectangular specimens due to high stress intensity at the beam roots. Stable crack growth at the chevron will guarantee that the toughness measured is a result of crack propagation instead of unstable fracture at a blunt notch that may be affected by ion implantation. Moreover, with a work of fracture approach, we resolve the fracture measurement with a well-established strain energy release rate calculation. This energy approach significantly simplifies the analytical analysis by simply extracting compliance data from a straightforward linear elastic finite element analysis model. In addition, multiple evaluations of toughness can be extracted from a single test. This is a significant advantage in fracture testing, since catastrophic failure usually results in one single measurement of the fracture toughness of one test specimen. Despite the added complexity

associated with milling a bowtie chevron specimen, it can be time and cost efficient by obtaining multiple fracture measurement. The time of fabrication and mechanical testing of a traditional spinel cantilever with a cross section of 2x2 or 3x3 μm is 4-5 hours to get one measurement, while it takes 5-6 hours for a bowtie chevron specimen like the ones described here. A 25% increase in fabrication time can bring a 5-8 times as many quantitative results.

Further work includes implementing bowtie chevron testing technique in other materials and also along a single grain boundary. The stable crack growth of bowtie chevron method and eliminating the mixed mode fracture behavior will benefit in guiding the fracture propagation path along the grain boundary and thus provide multiple measurement of grain boundary fracture toughness of a single experiment. Further analysis could also be focused on magnesium aluminate spinel in how to correlate the micro scale fracture toughens results with bulk material property. This will involve statistical analysis methods and large quantity of experimental measurement of grain boundary fracture tests to reveal and characterize the structure-property correlation. Rare earth elements other than Ytterbium and Europium could also be utilized in further study of dopants effects on grain boundary behavior. More experimental analysis will aid the investigation in grain boundary structure, energy and strength affected by dopant segregation behavior. The same systematic study method could also be utilized in testing and assessing other material system, when grain boundary fracture strength and structure was a focus. Micro-scale fracture testing methods could also be implemented on thin film

mechanical behavior evaluation or minimized medical device when the area of interest is in small scale. Furthermore, fracture toughness testing method of micro scale samples could also be utilized in metal and polymer where ductility is involved. In such case, J-integral methods could be employed to evaluation the fracture toughness results.

Bibliography

[1] R. Hertzberg, R. Vinci, J. Hertzberg, Deformation and fracture mechanics of engineering materials, 5th ed., 2013. http://cds.cern.ch/record/258912.

[2] Corning® Gorilla® Glass 3: Tougher Through Science, (n.d.). https://www.corning.com/gorillaglass/worldwide/en/videos/gorilla-glass-3-tougher-through-science.html.

[3] A.A. Griffith, The Phenomena of Rupture and Flow in Solids, Philos. Trans. R. Soc. A Math. Phys. Eng. Sci. 221 (1921) 163–198. doi:10.1098/rsta.1921.0006.

[4] C. Inglis, Stresses in a plate due to the presence of cracks and sharp corners, Trans. Inst. Nav. Archit. (1913).

[5] G. Irwin, Fracturing of metals, ASM, Clevel. (1948).

[6] H. Westergaard, J. of Applied Mechanics, Trans. ASME. (1939).

[7] G. Irwin, Fracture, Elast. Plast. Und Plast. (1958). https://link.springer.com/chapter/10.1007/978-3-642-45887-3_5

[8] W. Brown, J. Srawley, ASTM STP 410 (American Society for Testing and Materials, Philadelphia, 1966)

[9] R.O. Ritchie, Mechanisms of fatigue crack propagation in metals, ceramics and composites: Role of crack tip shielding, Mater. Sci. Eng. 103 (1988) 15–28. doi:10.1016/0025-5416(88)90547-2.

[10] I. Ganesh, A review on magnesium aluminate (MgAl 2 O 4) spinel: synthesis, processing and applications, Int. Mater. Rev. 58 (2013) 63–112. doi:10.1179/1743280412Y.0000000001.

[11] G. Gilde, P. Patel, P. Patterson, D. Blodgett, D. Duncan, D. Hahn, Evaluation of hot pressing and hot isostastic pressing parameters on the optical properties of spinel, J. Am. Ceram. Soc. 88 (2005) 2747–2751. doi:10.1111/j.1551-2916.2005.00527.x.

[12] R. Mishra, G. Thomas, Surface energy of spinel, J. Appl. Phys. (1977). http://aip.scitation.org/doi/abs/10.1063/1.323486 (accessed August 15, 2017).

[13] C. Fang, S. Parker, G. With, Atomistic simulation of the surface energy of spinel MgAl2O4, J. Am. Ceram. (2000). http://onlinelibrary.wiley.com/doi/10.1111/j.1151-2916.2000.tb01516.x/full

[14] J. Steeds, Introduction to anisotropic elasticity theory of dislocations, (1973). http://www.citeulike.org/group/1496/article/811516

[15] R. Stewart, M. Iwasa, R. Bradt, Room-Temperature KIc Values for Single-Crystal and Polycrystalline MgAl2O4, J. Am. (1981). http://onlinelibrary.wiley.com/doi/10.1111/j.1151-2916.1981.tb09560.x/full

[16] R. Stewart, R. Bradt, Fracture of single crystal MgAl2O4, J. Mater. Sci. (1980). http://link.springer.com/article/10.1007/BF00552428

[17] R. Stewart, R. Bradt, The brittle to ductile transition in MgAl2O4 spinel, Plast. Deform. Ceram. (1995). http://link.springer.com/chapter/10.1007/978-1-4899-1441-5_2

[18] G. Quinn, G. Quinn, Fractography of ceramics and glasses, 2007. http://nvlpubs.nist.gov/nistpubs/specialpublications/NIST.SP.960-16e2.pdf

[19] W. Cao, R. Vinci, Dissertation:Micro-scale Fracture Toughness Testing and Finite Element Analysis in Brittle Materials, Lehigh Univeristy, 2013.

[20] H.J. Reimanis, I.; Kleebe, A review on the sintering and microstructure development of transparent spinel (MgAl(2)O(4)) tle, J. Am. Ceram. Soc. 92 (2009).

[21] G. Villalobos, J. Sanghera, I. Aggarwal, Transparent Ceramics: Magnesium Aluminate Spinel, (2005). http://www.dtic.mil/docs/citations/ADA523625

[22] M. Ramisetty, S. Sastri, U. Kashalikar, L. Goldman, cubic spinels protect and defend, Ceramics.org. (n.d.). http://ceramics.org/wp-content/uploads/2013/02/march13_cover-story1.pdf

[23] W. Cao, A. Kundu, Z. Yu, M.P. Harmer, R.P. Vinci, Direct correlations between fracture toughness and grain boundary segregation behavior in ytterbium-doped magnesium aluminate spinel, Scr. Mater. 69 (2013) 81–84. doi:10.1016/j.scriptamat.2013.03.002.

[24] R. Jupp, D. Stein, D. Smith, Observations on the effect of calcium segregation on the fracture behaviour of polycrystalline alumina, J. Mater. Sci. (1980). http://link.springer.com/article/10.1007/BF00552432

[25] R. Cook, A. Schrott, Calcium segregation to grain boundaries in alumina, J. Am. Ceram. (1988). http://onlinelibrary.wiley.com/doi/10.1111/j.1151-2916.1988.tb05759.x/full

[26] G. West, J. Perkins, M. Lewis, The effect of rare earth dopants on grain boundary cohesion in alumina, J. Eur. Ceram. Soc. (2007). http://www.sciencedirect.com/science/article/pii/S095522190600478X

[27] J. Buban, K. Matsunaga, J. Chen, N. Shibata, Grain boundary strengthening in alumina by rare earth impurities, (2006). http://science.sciencemag.org/content/311/5758/212.short

[28] C. Conner, K. Faber, Segregant-enhanced fracture in magnesium oxide, J. Mater. Sci. (1990). http://link.springer.com/article/10.1007/BF00584873

[29] R.L. Satet, M.J. Hoffmann, Influence of the rare-earth element on the mechanical properties of RE-Mg-bearing silicon nitride, J. Am. Ceram. Soc. 88 (2005) 2485–2490. doi:10.1111/j.1551-2916.2005.00421.x.

[30] A. Ziegler, J. Idrobo, M. Cinibulk, C. Kisielowski, Interface structure and atomic bonding characteristics in silicon nitride ceramics, (2004). http://science.sciencemag.org/content/306/5702/1768.short

[31] W. Sanders, D. MIEWSKOWSKI, Strength and microstructure of sintered Si3N4 with rare-earth-oxide additions, Am. Ceram. Soc. Bull. (1985). http://cat.inist.fr/?aModele=afficheN&cpsidt=9206985

[32] P. Becher, E. Sun, K. Plucknett, Microstructural design of silicon nitride with improved fracture toughness: I, effects of grain shape and size, J. (1998). http://onlinelibrary.wiley.com/doi/10.1111/j.1151-2916.1998.tb02702.x/full

[33] R.L. Satet, M.J. Hoffmann, R.M. Cannon, Experimental evidence of the impact of rare-earth elements on particle growth and mechanical behaviour of silicon

nitride, Mater. Sci. Eng. A. 422 (2006) 66–76. doi:10.1016/j.msea.2006.01.015.

[34] S. Lojanová, P. Tatarko, Z. Chlup, M. Hnatko, J. Dusza, Z. Lenčéš, P. Šajgalík, Rare-earth element doped Si3N4/SiC micro/nano-composites—RT and HT mechanical properties, J. Eur. Ceram. Soc. 30 (2010) 1931–1944. doi:10.1016/j.jeurceramsoc.2010.03.007.

[35] A. Noviyanto, S. Han, H. Yu, D. Yoon, Rare-earth nitrate additives for the sintering of silicon carbide, J. Eur. Ceram. (2013). http://www.sciencedirect.com/science/article/pii/S0955221913002604

[36] P.. Tatarko, P.; Lojanova, S.; Dusza, J.; Sajgalik, Influence of various rare-earth oxide additives on microstructure and mechanical properties of silicon nitride based nanocomposites, Mater. Sci. Eng. a-Structural Mater. Prop. Microstruct. Process. (2010) 4771–4778.

[37] ASTM, E399 - 12e3 Standard Test Method for Linear-Elastic Plane-Strain Fracture Toughness K1C of Metallic Material, ASTM Int. (2013) 1–33. doi:10.1520/E0399-12E03.2.

[38] M. Sakai, R.C. Bradt, Fracture toughness testing of brittle materials, Int. Mater. Rev. 38 (1993) 53–78. doi:10.1179/imr.1993.38.2.53.

[39] Standard Test Methods for Determination of Fracture Toughness of Advanced Ceramics, ASTM C1421-15. (2014) 1–33. doi:10.1520/C1421-10.Annex.

[40] K. Takashima, S. Koyama, K. Nakai, Y. Higo, Development of fatigue pre-cracking method into micro-sized specimens for measuring Fracture Toughness, Mat. Res. Soc. Symp. 741 (2003) J3.3.1. https://www.cambridge.org/core/journals/mrs-

online-proceedings-library-archive/article/development-of-fatigue-pre-cracking-method-into-micro-sized-specimens-for-measuring-fracture-toughness/85B6A02F6BD4CFEE935BC4A945BA465B

[41] K. Matoy, H. Schönherr, T. Detzel, G. Dehm, Micron-sized fracture experiments on amorphous SiOx films and SiOx/SiNx multi-layers, Thin Solid Films. 518 (2010) 5796–5801. doi:10.1016/j.tsf.2010.05.114.

[42] D.E.J. Armstrong, A.J. Wilkinson, S.G. Roberts, Micro-mechanical measurements of fracture toughness of bismuth embrittled copper grain boundaries, Philos. Mag. Lett. 91 (2011) 394–400. doi:10.1080/09500839.2011.573813.

[43] W.D. Weihs, T. P.; Hong, S.; Bravman, J. C.; Nix, Mechanical deflection of cantilever microbeams - a new technique for testing the mechanical-properties of thinfilms., J. Mater. Res. 3 (1988) 931–942.

[44] D. Armstrong, A. Haseeb, A. Wilkinson, Micro-fracture testing of Ni-W microbeams produced by electrodeposition and FIB machining, MRS Online. (2006) 29. https://www.cambridge.org/core/journals/mrs-online-proceedings-library-archive/article/micro-fracture-testing-of-ni-w-microbeams-produced-by-electrodeposition-and-fib-machining/43657CC3100D29736A9301DDA68B774D

[45] D.E.J. Armstrong, A.S.M.A. Haseeb, S.G. Roberts, A.J. Wilkinson, K. Bade, Nanoindentation and micro-mechanical fracture toughness of electrodeposited nanocrystalline Ni-W alloy films, Thin Solid Films. 520 (2012) 4369–4372. doi:10.1016/j.tsf.2012.02.059.

[46] K. Matoy, H. Schönherr, T. Detzel, T. Schöberl, R. Pippan, C. Motz, G. Dehm, A

comparative micro-cantilever study of the mechanical behavior of silicon based passivation films, Thin Solid Films. 518 (2009) 247–256. doi:10.1016/j.tsf.2009.07.143.

[47] M. V. Ichikawa, Y.; Makekawa, S.; Takashima, K.; Shimojo, M.; Higo, Y.; Swain, Fracture behavior of micro-sized Ni-P amorphous alloy specimens, Mat. Res. Soc. Symp. (2000) 273.

[48] M.G. Mueller, V. Pejchal, G. Žagar, A. Singh, M. Cantoni, A. Mortensen, Fracture toughness testing of nanocrystalline alumina and fused quartz using chevron-notched microbeams, Acta Mater. 86 (2015) 385–395. doi:10.1016/j.actamat.2014.12.016.

[49] G. Žagar, V. Pejchal, M.G. Mueller, L. Michelet, A. Mortensen, Fracture toughness measurement in fused quartz using triangular chevron-notched micro-cantilevers, Scr. Mater. 112 (2016) 132–135. doi:10.1016/j.scriptamat.2015.09.032.

[50] B.N. Jaya, V. Jayaram, S.K. Biswas, A new method for fracture toughness determination of graded (Pt,Ni)Al bond coats by microbeam bend tests, Philos. Mag. 92 (2012) 3326–3345. doi:10.1080/14786435.2012.669068.

[51] B.N. Jaya, V. Jayaram, Crack stability in edge-notched clamped beam specimens: Modeling and experiments, Int. J. Fract. 188 (2014) 213–228. doi:10.1007/s10704-014-9956-2.

[52] B.N. Jaya, Can microscale fracture tests provide reliable fracture toughness values ? A case study in silicon, (2015) 1–13. doi:10.1557/jmr.2015.2.

[53] B.N. Jaya, S. Bhowmick, S.A.S. Asif, O.L. Warren, V. Jayaram, Optimization of

clamped beam geometry for fracture toughness testing of micron-scale samples, Philos. Mag. 95 (2015) 1945–1966. doi:10.1080/14786435.2015.1010623.

[54] O. Schumacher, Thermodynamics and kinetics of complexion transitions in europium-doped MgAl2O4, (2016) 139.

[55] A. Ayhan, H. Nied, FRAC3D—finite element based software for 3-D and generalized plane strain fracture analysis (second revision), (1999).

[56] R. Bradt, Cleavage of ceramic and mineral single crystals, (1997). https://www.osti.gov/scitech/biblio/293153 (accessed August 15, 2017).

[57] M.M. Hasan, P.P. Dholabhai, R.H.R. Castro, B.P. Uberuaga, Stabilization of MgAl2O4 spinel surfaces via doping, Surf. Sci. 649 (2016) 138–145. doi:10.1016/j.susc.2016.01.028.

[58] O. Schumacher, C.J. Marvel, M.N. Kelly, P.R. Cantwell, R.P. Vinci, J.M. Rickman, G.S. Rohrer, M.P. Harmer, Complexion time-temperature-transformation (TTT) diagrams: Opportunities and challenges, Curr. Opin. Solid State Mater. Sci. 20 (2016) 316–323. doi:10.1016/j.cossms.2016.05.004.

[59] G. Rohrer, Grain boundary energy anisotropy: a review, J. Mater. Sci. (2011). http://link.springer.com/article/10.1007/s10853-011-5677-3

[60] J.I. Bluhm, Stability considerations in the generalized three dimensional “Work of Fracture” Specimen, Adv. Res. Strength Fract. Mater. Fourth Int. Conf. Fracure. 3 (1977). http://www.gruppofrattura.it/ocs/index.php/ICF/ICF4/paper/download/2625/7433

[61] H.G. Tattersall, G. Tappin, G.T. H.G. Tattersall, The work of fracture and its measurement in metals, ceramics and other materials, J. Mater. Sci. 1 (1966) 296–301. doi:10.1007/BF00550177.

[62] R. Sanford, Principles of Fracture Mechanics, Peason Education, Inc, New Jersey. (2003).

[63] J.N.Ã. Florando, W.D. Nix, A microbeam bending method for studying stress – strain relations for metal thin films on silicon substrates, J. Mech. Phys. Solids. 53 (2005) 619–638. doi:10.1016/j.jmps.2004.08.007.

[64] D. Kupka, E.T. Lilleodden, Mechanical Testing of Solid-Solid Interfaces at the Microscale, Exp. Mech. 52 (2012) 649–658. doi:10.1007/s11340-011-9530-z.

[65] F.I. Baratta, Crack Stability and Its Effect on Fracture Toughness of Hot-Pressed Silicon Nitride Beam Specimens, J. Am. Ceram. Soc. (1996).

[66] D.S. Harding, W.C. Oliver, G.M. Pharr, Cracking During Nanoindentation and its Use in the Measurement of Fracture Toughness, MRS Proc. 356 (1994) 663–668. doi:10.1557/PROC-356-663.

[67] L. Barker, Short Bar Specimens for K Ic Measurements, Fract. Mech. Appl. to Brittle Mater. (1979). http://www.astm.org/DIGITAL_LIBRARY/STP/PAGES/STP36626S.htm

[68] T. Scholz, G.A. Schneider, J. Muñoz-Saldaña, M. V. Swain, Fracture toughness from submicron derived indentation cracks, Appl. Phys. Lett. 84 (2004) 3055–3057. doi:10.1063/1.1711164.

[69] C. Bouvier, J.C. Lambropoulos, S.D. Jacobs, Fracture toughness of ULE , Zerodur ,

Astrosital and Corning 9600, Opt. Soc. Am. 2 (2004) 4–6.

[70] M.J. Viens, Fracture Toughness and Crack Growth of Zerodur, NASA Tech. Memo. 4185. (1990) 1–30. http://www.dtic.mil/docs/citations/ADA309969

Vita

Fiona Yuwe Cui, the daughter of Fang Cui and Yanxia Wang, was born in Harbin, Heilongjiang Province, China on June 4th, 1988. She went to Harbin No. 3 high school and graduated in 2007. Then she went to Harbin Institute of Technology and graduated as a Bachelor in Science in the major of Controls Engineering in 2011. After completion of Bachelor degree, she came to United States to pursue graduate degree. She received her Master Degree in the department of Mechanical Engineering in 2013. Her Ph.D. study is in the department of Materials Science and Engineering under direction of Professor Richard P. Vinci.